

NUMERICAL INVESTIGATION OF CONTROLS ON MEGATHRUST
EARTHQUAKES ALONG THE JAPAN TRENCH SUBDUCTION ZONE

A Dissertation

by

BIN LUO

Submitted to the Office of Graduate and Professional Studies of
Texas A&M University
in partial fulfillment of the requirements for the degree of

DOCTOR OF PHILOSOPHY

Chair of Committee,	Benchun Duan
Committee Members,	Frederick Chester
	Andreas Kronenberg
	David Sparks
	Marcelo Sanchez
Head of Department,	Michael Pope

December 2018

Major Subject: Geophysics

Copyright 2018 Bin Luo

ABSTRACT

The goal of this dissertation is to investigate physical conditions that control the generation of megathrust earthquakes, such as the 2011 Mw 9.0 Tohoku earthquake, along the Japan Trench subduction zone. Understanding the physical conditions that lead to megathrust earthquakes is of great importance to earthquake prediction and seismic hazard mitigation. In order to fulfill this goal, I establish an advanced elastodynamic modeling algorithm based on dynamic finite element method for numerical investigation of dynamic earthquake rupture and earthquake cycle behavior.

I first implement nonplanar fault geometry and various forms of the laboratory-derived rate- and state-dependent friction laws in the framework of the dynamic finite element method. Using the updated method, I explore how dynamic ruptures would behave under the influence of different friction laws on a fault surface with a bump representing a subducted oceanic relief. The results show that the bump could act as a rupture barrier, and such a geometrical effect varies with the dimension of the bump and with the specific forms of friction law.

I then extend the dynamic modeling method to an integrated earthquake simulator by using the adaptive dynamic relaxation technique. The new earthquake simulator is capable of capturing both long-term and short-term faulting behaviors in multiple earthquake cycles. Earthquake cycle simulations of thrust faults with various dip angles show that thrust faults tend to produce earthquake cycles with a longer recurrence interval and larger released seismic energy compared with strike-slip faults. Moreover, I find that

the asymmetry in particle displacements across a thrust fault caused by earthquakes can be recovered during the interseismic phase.

Finally, I conduct numerical investigation on earthquake cycle behavior in subduction fault models of the Japan Trench subduction zone. I find that a planar fault model with realistic structural heterogeneity reproduces complex faulting behavior including numerous aseismic transients in interseismic period and a megathrust earthquake that resembles the 2011 event, while a homogeneous model with complex fault geometry of a low-height, broad-base seafloor relief accumulates stress changes slowly on the geometrical irregularity over time but generates simple pattern for earthquake cycles within the limited simulation time.

DEDICATION

To my family.

ACKNOWLEDGEMENTS

I would like to give my special thanks to my advisor, Dr. Benchun Duan, for his hard work and dedication to my research, and for his patient and supportive guidance through my Ph.D. study. Many thanks also go to my committee members, Dr. Chester, Dr. Kronenberg, Dr. Sparks and Dr. Sanchez, for their guidance and support throughout the course of this research.

I also want to thank the Department of Geology and Geophysics at Texas A&M University for offering this Ph.D. program and the departmental faculty for offering excellent courses for my Ph.D. study.

Thanks also go to my friends and colleagues for making my time at Texas A&M University a great experience.

Finally, thanks to my parents and my family for their consistent support and encouragement during my study.

CONTRIBUTORS AND FUNDING SOURCES

This work was supervised by a dissertation committee consisting of Professors Benchun Duan, Frederick Chester, Andreas Kronenberg and David Sparks of the Department of Geology and Geophysics and Professor Marcelo Sanchez of the Zachry Department of Civil Engineering.

All work for the dissertation was completed by the student, under the advisement of Professor Benchun Duan of the Department of Department of Geology and Geophysics.

Graduate study was mainly supported by research grant from National Science Foundation under Grant Number EAR-1254573. It was also supported in part by a departmental fellowship and teaching assistantship from the Department of Geology and Geophysics. The contents in this work are solely the responsibility of the authors and do not necessarily represent the official views of National Science Foundation and the Department of Geology and Geophysics.

Portions of this research were conducted with the advanced computing resources provided by Texas A&M High Performance Research Computing (<http://hprc.tamu.edu/>).

TABLE OF CONTENTS

	Page
ABSTRACT	ii
DEDICATION	iv
ACKNOWLEDGEMENTS	v
CONTRIBUTORS AND FUNDING SOURCES	vi
TABLE OF CONTENTS	vii
LIST OF FIGURES	ix
LIST OF TABLES	xvi
CHAPTER I INTRODUCTION	1
CHAPTER II DYNAMICS OF NONPLANAR THRUST FAULTS GOVERNED BY VARIOUS FRICTION LAWS	5
2.1 Introduction	5
2.2 Fault Geometry and Stresses	7
2.3 Functional Forms of Various Friction laws	12
2.4 Implementation of rate- and state-dependent friction laws in finite element methods	17
2.5 Comparing Frictional Behaviors of Various Friction Laws	21
2.6 Modeling Results	33
2.7 Discussion	47
2.8 Conclusions	54
CHAPTER III DYNAMIC FINITE ELEMENT MODELING OF EARTHQUAKE CYCLES ON FAULTS WITH RATE- AND STATE-DEPENDENT FRICTION	56
3.1 Introduction	56
3.2 A New Dynamic Earthquake Simulator Based on Finite Element Method ...	60
3.2.1 Dynamic Modeling with Rate- and State-Dependent Friction	61
3.2.2 Static Modeling Using Adaptive Dynamic Relaxation Method	64
3.2.3 Quasi-Static Modeling with Rate- and State-Dependent Friction	67
3.2.4 Integrated Modeling of Full Earthquake Cycles	72
3.2.5 Fault Geometry and Model Configuration	74
3.3 Verification of the Dynamic Earthquake Simulator	82
3.3.1 Quasi-Static Simulation Benchmark	82
3.3.2 Earthquake Cycle Simulation on a Vertical Strike-Slip Fault	84
3.4 Application of the Dynamic Earthquake Simulator: Earthquake Cycle Behaviors of Thrust Faults	89

3.5 Discussion	101
3.6 Conclusions	108
CHAPTER IV THREE-DIMENSIONAL MODELING OF MEGATHRUST EARTHQUAKES ALONG THE JAPAN TRENCH SUBDUCTION ZONE.....	110
4.1 Introduction	110
4.2 Model Setup	114
4.2.1 Structural Heterogeneity	115
4.2.2 Nonplanar Fault Geometry.....	118
4.2.3 Frictional Parameters	119
4.2.4 Boundary and Initial Conditions	122
4.3 A Subduction Fault Model with Structural Heterogeneity.....	124
4.3.1 Earthquake Sequence and Fault Slip.....	124
4.3.2 Earthquake Rupture.....	127
4.3.3 Aseismic Transients and Earthquake Nucleation.....	131
4.4 A Subduction Fault Model with Nonplanar Fault Geometry	136
4.5 Discussion	137
4.5.1 Slip Pattern of the 2011 Tohoku Megathrust Earthquake	138
4.5.2 Giant Earthquake Sequence	139
4.5.3 Aseismic Transients and M7~8 Large Earthquakes.....	140
4.6 Conclusions	143
CHAPTER V SUMMARY	145
REFERENCES	148

LIST OF FIGURES

	Page
Figure 2. 1 (a) A hexahedral element degenerated into two wedge elements. Split nodes of the ideal dipping fault plane are separated for illustration purpose. A local coordinate system is shown on the fault surface, and a global coordinate system used for entire mesh generation is shown on the right. (b) The nonplanar part of the thrust fault model. The locally curved shape of the mesh represents a circular bump on the fault surface centered at 9 km along dip from the fault trace (not shown here). Note that the fault is embedded in a three-dimensional finite element domain.....	9
Figure 2. 2 The profile of background initial normal stress along dip direction (a), initial normal stress (b) and initial shear stress (c) in the vicinity of the seamount, respectively. Black circles and red stars in (b) and (c) denote the circular boundary of the bump on the fault and the hypocenter where rupture begins, respectively.....	12
Figure 2. 3 Comparison of shear stresses as a function of slip at the hypocenter for all four types of friction laws with frictional parameters listed in Table 1. In all friction laws the stress first rises from initial level (30 MPa) to the static friction (~38 MPa), and then drops to the dynamic friction (~27.3 MPa) over certain amount of slip after yielding.	23
Figure 2. 4 (a) and (b) show the initial normal and shear stress profiles along dip direction through the center of the bump for various bump heights. (c) shows the profiles of estimated yield stress in RSF law. (d) shows the variation of stress quantities at the most compressive location (at 10.5 km along dip) on the bump as a function of the height of the bump, including initial normal stress σ_n , the initial shear stress τ_0 , the yield stress τ_u estimated by the SW law and the yield stress τ_u estimated by the RSF laws.....	26
Figure 2. 5 Spatial distributions of the dynamic friction coefficient in various friction laws at 4 s. The solid and dashed lines denote the leading and trailing edges of the propagating rupture front, respectively. The area within the dashed line has been ruptured at this moment and is sliding with spatially varying dynamic friction coefficient below 0.56. The area outside the dashed line has friction coefficient above 0.56 and is not color-coded, including the intact area outside the solid line and the cohesive zone between the solid line and the dashed line.	29

Figure 2. 6	Moment rate functions of dynamic ruptures on planar faults governed by various friction laws. The curves in each group of friction laws are nearly identical using the frictional parameters selected based on the assumption of equal fracture energy and equal average dynamic friction between friction laws. However, during rupture nucleation (0 to 2 s), the moment rate of the exponentially decaying group (RS-S and RS-FH) accelerates earlier than the linearly weakening group (SW and RS-A). After the rupture leaves the nucleation patch (2 to 4 s), the former group has reached a higher moment rate than the latter group.....	32
Figure 2. 7	The moment magnitude variation of simulated dynamic ruptures as the height of the bump varies. The results of four types of friction laws are shown for comparison.	33
Figure 2. 8	Comparison of rupture time contours of dynamic rupture simulations governed by the RS-A law on a planar fault (a) and a nonplanar fault with a 300 m high bump (b), a 600 m high bump (c) and a 900 m high bump (d). The contour interval is 1 s. The black dashed circle in each contour denotes the position of the bump. The rupture in (d) is terminated by the bump and the blank area outside the 20 s rupture time contour line is not ruptured.	35
Figure 2. 9	Snapshots of the slip rate spatial distribution for the dynamic rupture simulation governed by the RS-A law on a nonplanar fault with a 300 m high bump. The white dashed circle in each snapshot denotes the position of the bump. Same for the following figures.	37
Figure 2. 10	Snapshots of the spatial slip rate distribution for the dynamic rupture simulation with governed by the SW law on a nonplanar fault with a 600 m high bump.....	39
Figure 2. 11	Snapshots of the slip rate spatial distribution for the dynamic rupture simulation governed by the RS-A law on a nonplanar fault with a 600 m high bump.....	40
Figure 2. 12	Snapshots of the slip rate spatial distribution for the dynamic rupture simulation governed by the RS-S law (upper panel) and RS-FH law (lower panel) on a nonplanar fault with a 600 m high bump.....	42
Figure 2. 13	Comparison of slip rate and shear stress evolution at the location of the bump center between a planar fault (a and b) and a nonplanar fault with 600 m high bump (c and d).	45
Figure 2. 14	Comparison of particle velocity at a free surface location above the bump center between a planar fault (a and b) and a nonplanar fault with 600 m high bump (c and d). Both y-component and z-component velocities	

are shown. The x-component velocity is trivial due to symmetry of the model and not shown. A signal related to bump failure in each nonplanar fault model that has a bump failure is pointed out by an arrow with a corresponding line style.	46
Figure 2. 15 Space-time plots of slip rate along the line in dip direction through the center of the bump. (a) and (b) are SW cases with no bump and a bump of 600 m high, respectively. (c) and (d) are RS-A cases with no bump and a bump of 600 m high, respectively. Slip rate is in m/s. Dashed lines in (b) and (d) denote the updip and downdip boundary of the bump. The along-dip profile is extended to 23 km to include the strengthening fault edge (20 to 23 km) to show the termination of the rupture.	51
Figure 3. 1 Schematic diagrams that show (a) a right-lateral strike-slip planar fault model and (b) a thrust planar fault model with dip angle ϕ . The fault boundary completely separates the model domain into two blocks to avoid singular solution. The red arrows represent the major movement direction of the blocks.	76
Figure 3. 2 Comparison of (a) along-strike and (b) along-dip dynamic slip profiles in grid resolution tests with grid size of 100 m, 200 m, and 400 m. These dynamic rupture tests use the large fault geometry $\Omega 1$ and model parameters presented in Table 3. 1. Slip profiles at 2 s, 4 s, and 6 s are shown.	79
Figure 3. 3 Spatial distribution of frictional parameters on the large fault surface. (a) shows spatial areas of $a - b < 0$ (dark blue) and $a - b > 0$ (light blue). (b) shows the vertical profile of a (blue curve) and $a - b$ (red curve) at $x_s = 0$. (c) shows the horizontal profile of same parameters at $x_d = 10$ km. The central area where $a - b < 0$ is the seismogenic zone with steady state velocity weakening property (VW). The surrounding area outside the seismogenic zone where $a - b > 0$ is the stable creep area with steady state velocity strengthening property (VS). High initial shear stress is assigned in the rectangular patch marked by the dashed white line to artificially initiate the first event in the earthquake cycle simulation.	81
Figure 3. 4 (a) A schematic diagram showing the two-dimensional anti-plane vertical fault geometry for an ideal earthquake cycle benchmark problem. (b) Comparison of the analytic (solid) and numerical (dashed) solutions of the displacement distributions at the free surface every 10 years in an earthquake cycle of 50 years. The horizontal coordinate x is normalized by the width D of the locked zone and presented in a logarithmic scale. The results are anti-symmetrical about the fault and thus only the $x < 0$ part is shown.	84

- Figure 3. 5 Logarithmic maximum slip rate history of the fifth cycle in various time scales. (a) shows part of the simulated earthquake sequence (black curve) from 200 to 400 years, in which the fifth event (red curve) occurs in year 293. Red dot marks the onset of the dynamic process, and black dot marks the onset of the quasi-static process. Evolution details of V_{max} in the red dashed box are shown in (b) time scale of seconds and (c) simulation time steps. The start and the end of data in (b) correspond to the first and the last time step shown in (c). The time origin in (b) is reset to the beginning of the dynamic event.85
- Figure 3. 6 Snapshots of slip rate spatial distribution on the vertical strike-slip fault surface of $\Omega 1$ from the interseismic phase before the fifth event to the nucleation phase before the sixth event. Slip rate in log scale ranges from 10 – 12 m/s (interseismic locking) to 1 m/s (seismic slip). The elapsed time of the snapshot from the beginning of the run is shown at the top left corner. For the coseismic snapshots, the elapsed time from the switch moment is also shown at the top right corner. Snapshots are selected to illustrate key features observed in the earthquake cycles: (a-d) interseismic, (e-f) nucleation, (g-j) coseismic, (k) postseismic, (l-m) interseismic, (n-o) nucleation.88
- Figure 3. 7 Scaling of (a) the average recurrence interval and (b) the average seismic moment with respect to $\sin\phi$ of various thrust fault models. Red dashed lines denote the least squares fitted lines of the data. (c) shows the $Tr - M0$ relation of all the events in simulated earthquake sequences of the four dip-slip fault models. Note that both quantities are in log scale and Tr is in seconds. The black dashed line passing through the simulated data represents the fitted line of the simulated events and suggests a relation $Tr \propto M0^{0.77}$. The black solid line, which suggests $Tr \propto M0^{0.17}$, represents the fitted line of the observed repeating small earthquakes (more than 90% right-lateral strike-slip) in the Parkfield segment of SAF where repeating M6 events are expected (Nadeau and Johnson, 1998).91
- Figure 3. 8 Snapshots of slip rate spatial distribution on the 30° dip thrust fault surface of $\Omega 2$ from the interseismic phase before the fifth event to the nucleation phase before the sixth event. Similar to Figure 3. 6, snapshots are selected to illustrate key features observed in the earthquake cycles: (a-d) interseismic, (e-f) nucleation, (g-j) coseismic, (k) postseismic, (l-m) interseismic, (n-o) nucleation.92
- Figure 3. 9 Cumulative slip history of the along-strike profile at $xd = 7 \text{ km}$ on the thrust faults with (a) 90°, (b) 45°, (c) 30° and (d) 15° dip angles. Solid curves denote slow aseismic slip at an interval of five years. Dashed curves denote fast seismic slip at an interval of one second. The origin of the slip

- history is set to the moment in the middle of the interseismic period between the second and the third event. Five successive events are shown in (a) and (b), four are shown in (c) and (d).95
- Figure 3. 10 Cumulative slip history of the along-dip profile at $x_s = -8 \text{ km}$ on the thrust faults with (a) 90° , (b) 45° , (c) 30° and (d) 15° dip angles. Solid curves denote slow aseismic slip at an interval of five years. Dashed curves denote fast seismic slip at an interval of one second. Five successive events are shown in (a) and (b) and four are shown in (c) and (d).96
- Figure 3. 11 Spatiotemporal evolution of interseismic slip rate along the horizontal line at $x_d = 7 \text{ km}$ on the thrust faults with (a) 45° and (b) 15° dip angles in 120 years after the fifth event. The color scale for slip rate ranges from $10 - 12$ to $10 - 8 \text{ m/s}$ to emphasize interseismic features. The time origin is reset to the end of the coseismic phase of the fifth event where the following postseismic phase begins. The sixth event occurs in year 76 in (a) and in year 94 in (b).98
- Figure 3. 12 Particle motion histories of the sliding pairs at $x_d = 7 \text{ km}$ and different strike location $x_s = 0 \text{ km}$ (black solid), -12 km (blue dotted) and -19 km (red dashed) on the 15° dipping thrust fault, including (a) cumulative slip, (b) cumulative mean particle displacement, (c) cumulative particle displacement on the hanging wall, and (d) cumulative particle displacement on the foot wall. Quantities are measured along updip direction and particle motions are in opposite directions between the hanging wall and the footwall. The time ranges from the beginning of the third event to the beginning of the seventh event, in which four cycles are included. Cumulative motion starts with zero at the beginning of the time range.99
- Figure 3. 13 Cumulative slip history of the along-strike profile at $x_d = 10 \text{ km}$ on the vertical (a) strike-slip and (b) dip-slip faults. Solid curves denote slow aseismic slip at an interval of five years. Dashed curves denote fast seismic slip at an interval of one second. The origin of the slip history is set to the moment in the middle of the interseismic period between the second and the third event. Both plots show the cumulative slip history of four subsequent cycles.103
- Figure 3. 14 Interseismic evolution of the along-strike shear stress profiles at $x_d = 10 \text{ km}$ in the VW zone of the vertical (a and c) strike-slip and (b and d) dip-slip faults. (a and b) show the interseismic period before the fifth event, and (c and d) show the period before the sixth event. Black arrows denote the propagation direction of the inward propagating edge of the locked zone where shear stress reaches a local peak value. Note that the

curves associated with the stress peaks at the outermost of the VW zone are at early stage of the interseismic period and show residual stress level of the preceding dynamic event, while the curves associated with the peaks at the innermost of the VW zone are at late stage and about to trigger nucleation.	105
Figure 4. 1 Depth cross-section of the major portion of the finite element mesh for the subduction fault model, including geometry of the fault plane between hanging wall and footwall and layers in the overriding plate. See text for more details of the color-coded structural heterogeneity. Solid black line denotes the fault area of interest in this study, while dashed black line denotes the deep portion of the fault plane that always slides freely at plate convergence rate. Black arrows denote relative plate motions across the fault plane. Element size is 15 km for illustration purpose.	117
Figure 4. 2 (a) Along-trench P-wave velocity profiles in the upper and lower portions of the continental crust within 150 km from the trench line. (b) Along-trench rock density profile in the continental crust.	117
Figure 4. 3 (a) A fault plane with 15° dip from the free surface embedded in a hexahedral model domain. The fault plane divides the model domain into two blocks. The red arrows represent the major movement direction of the blocks. (b) FEM mesh of the nonplanar fault surface discretized by square elements. Only the part with the bump geometry is shown. Element size is 3 km for illustration purpose.	119
Figure 4. 4 Profiles of frictional parameter $a - b$ along (a) dip and (b) strike directions.	122
Figure 4. 5 Maximum slip velocity histories in log scale (a) between year 0 and 2000, (b) between year 850 and 1150, and (c) between year 1550 and 1850. A total of six events (large spikes) are shown in (a). The fourth and the sixth events are shown in (b) and (c), respectively.	125
Figure 4. 6 Cumulative slip history of the along-strike profile at (a) 70 km and (b) 140 km along dip from the trench line. Blue solid curves denote slow aseismic slip at an interval of ten years. Red dashed curves denote fast seismic slip at an interval of five seconds. The origin of the slip history is set to the moment in the middle of the interseismic period between the first and the second event in the sequence. Five successive events are shown.	127
Figure 4. 7 Snapshots of slip velocity on the fault plane for the sixth dynamic event in the earthquake sequence. Corresponding time is shown on each snapshot. For illustration purpose, the onset time is set to the moment when	

maximum slip velocity in the nucleation zone becomes greater than 0.3 m/s.	129
Figure 4. 8 Distributions of (a) final slip and (b) stress drop on the fault plane for the sixth dynamic event in the earthquake sequence. Black dash dotted circles indicate the rough size and location of the nucleation zone.	130
Figure 4. 9 Snapshots of logarithmic sliprate over the fault for the interseismic period before the sixth event.	132
Figure 4. 10 Space-time diagram of sliprate in log scale at 100 km dip from the trench line. The sliprate evolution indicates the north-to-south propagation of the aseismic transient within 30 days before rupture initiation of the sixth event in the modeled earthquake sequence. The black dashed line denotes the front (peak sliprate along strike) that migrates at a constant speed of 0.8 km/day.	134
Figure 4. 11 Simulation results of the nonplanar subduction fault model with a low-height, broad-base bump. (a) shows maximum slip velocity history in log scale. Red dots in the interseismic and nucleation phases before the seventh event sequentially denote the time of the logarithmic sliprate snapshots in (b), (c), (d), and (e). Shear and normal stress distributions for a coseismic moment of the seventh event are shown in (f) and (g), respectively. White ellipses in the sliprate snapshots and black ellipses in the stress distributions denote the size and location of the bump geometry on the fault.	135

LIST OF TABLES

	Page
Table 2. 1 Model and frictional parameters	16
Table 2. 2 Rupture Type Classification.....	43
Table 3. 1 Summary of Model Parameters in This Study	78
Table 3. 2 Measured Quantities of Earthquake Cycles on Various Thrust Fault Models	91
Table 4. 1 Model Parameter Summary.....	123

CHAPTER I

INTRODUCTION

On 11 March 2011, an Mw 9.0 undersea earthquake occurred 70 km offshore Honshu in northeastern Japan. This event was the result of the relative sliding motion between the overriding and underlying plates in the Japan Trench subduction zone. In addition to generating strong ground motion in its vicinity, the rupture managed to reach the undersea trench and caused a significant amount of seafloor deformation, which excited a catastrophic tsunami that struck the Pacific coast of Japan. Although there used to be large megathrust earthquakes of M7~8 occurring along the Japan Trench subduction zone, this 2011 event is still a great surprise, because its magnitude is unprecedentedly large in this area and it ruptures the unexpected part of the Japan Trench subduction zone where no large megathrust earthquakes have been recorded in the past century. Extensive observations in this region have revealed many aspects of this 2011 event. For example, kinematic inversions of seismic, geodetic and tsunami data provide slip distribution of the 2011 rupture on the megathrust fault (e.g., *Fujii et al.*, 2011; *Ide et al.*, 2011; *Lay et al.*, 2011; *Simons et al.*, 2011). The Japan Trench Fast Drilling Project (JFAST) deployed in the shallow large slip area on the megathrust fault after the 2011 event allows direct core sampling for experimental analysis (e.g., *Chester et al.*, 2013; *Ujiie et al.*, 2013) and in situ temperature measurement for dissipated frictional heat energy evaluation (*Fulton et al.*, 2013). However, two categories of scientific questions regarding the underlying physics of the generation of this megathrust earthquake remain to be addressed. The first

category of questions ask why the 2011 earthquake occurred in the way it did and what conditions on the Japan Trench subduction zone caused its occurrence. The second category of questions ask what is the relation between this megathrust earthquake (M9) and previous large earthquakes (M7~8) along the Japan Trench subduction zone in the history and what conditions control the generation of earthquakes of various sizes.

The overall goal of this project is to understand better the physical conditions that led to this Mw 9.0 event along the Japan Trench subduction zone. In regard to the rupture characteristics of the 2011 event itself and the role of this event in a broader context of earthquake cycle behavior along the Japan Trench subduction zone, we conduct a series of three coherent research studies based on dynamic finite element method to systematically investigate the controlling factors in generating megathrust earthquakes.

In Chapter II, we first investigate how large-scale geometrical irregularities can affect dynamic rupture under the influence of different friction laws. In subduction zone, large-scale irregular geometry of a fault surface, such as seamounts and subducted oceanic plateaus, is a prevailing factor that introduces stress heterogeneity and affects rupture dynamics. *Duan* (2012) employs dynamic finite element method (FEM) code EQdyna to conduct 3D simulation of spontaneous rupture governed by the classic slip-weakening friction law with a high stress patch on the megathrust fault, mimicking a seamount updip of the hypocenter of the 2011 event. The patch with lower pore fluid pressure and high strength stalls initial rupture expansion until its failure occurs, leading to massive rupture over the entire fault surface. Here we implement the modern laboratory-derived rate- and state-dependent friction laws of various forms in the FEM code EQdyna and investigate

rupture dynamics in three-dimensional thrust fault models with explicitly characterized seamount geometry and various friction laws.

In Chapter III, we extend our research scope from individual dynamic event to a broader context of earthquake cycle behavior involving a sequence of repeated earthquakes and the quasi-static periods between these earthquakes. Dynamic rupture studies often focus on the narrow time window of individual events and oversimplify the complicated prestress conditions that evolves from residual stress conditions of the past events and interseismic tectonic deformation processes. Numerical simulation of multiple cycles captures full details of stress evolution on the fault over long-term period and provides spontaneously developed prestress conditions. To conduct earthquake cycle simulations that incorporate as many physics as possible, we develop a new dynamic earthquake simulator based on the dynamic FEM code EQdyna and a dynamic relaxation technique. Governed by rate- and state-dependent friction law, this advanced earthquake simulator is capable of reproducing sequential dynamic events on realistically complex fault system embedded in heterogeneous medium. Tests on a vertical strike-slip fault verify the correctness of the methodology. As an application example, we employ the developed methodology to numerically investigate how the asymmetric thrust fault geometry affects long-term and short-term fault slip behaviors in earthquake cycles.

In Chapter IV, we utilize the newly developed earthquake simulator to perform earthquake cycle simulations along the Japan Trench subduction zone to explore the physical controls that generate repeated earthquakes of various sizes. According to paleoseismic studies, the 2011 M9 Tohoku earthquake may be part of a giant earthquake

sequence with a recurrence interval of hundreds of years. This is beyond our seismic observations of the past century, which records only M7~8 earthquakes with an interval of 30~40 years. Here we investigate two volumetric models based on realistic observations, one with heterogeneous geologic structure and the other with nonplanar fault geometry, as both models are suggested as plausible candidates that controls the generation of giant and large earthquakes.

Understanding the physical conditions that controls generation of the unusual M9 Tohoku earthquake and its relation with historical M7~8 events on Japan Trench subduction zone is of great importance to seismic hazard analysis in subduction zone areas. What we learn from these studies can be broadly applied to subduction zone areas, such as Cascadia, Chile, Nankai and Sumatra.

CHAPTER II

DYNAMICS OF NONPLANAR THRUST FAULTS GOVERNED BY VARIOUS FRICTION LAWS*

2.1 Introduction

Fault interface topography is a prevailing factor in earthquake rupture dynamics. In subduction zones, large-scale oceanic reliefs such as seamounts and plateaus on the incoming oceanic plate can be driven into the subduction fault zone and form geometrical irregularities on the fault interface. The nature of how subducted oceanic reliefs could affect megathrust earthquakes remains unclear, and contradictory mechanisms attempting to explain their seismic effect demonstrate how complex this problem is. Subducted oceanic reliefs have been suggested to weaken the interplate coupling by severely damaging the overriding plate, such as eroding the base of the accretionary wedge, which entrains fluid-rich sediments into the seismogenic zone, lowers the effective normal stress and hence reduces elastic strain accumulation for potential earthquake rupture (*Bangs et al.*, 2006; *Mochizuki et al.*, 2008), or fracturing the overriding plate, which creates a complex fracture network and forms an environment favorable for aseismic creep instead of megathrust earthquakes (*Dominguez et al.*, 1998; *Wang and Bilek*, 2011; 2014; *Kyriakopoulos and Newman*, 2016). On the contrary, they have also been suggested to induce strong interplate coupling by colliding against the base of the overriding plate as

* Modified version of a paper by Bin Luo and Benchun Duan titled “Dynamics of Nonplanar Thrust Faults Governed by Various Friction Laws” published in *Journal of Geophysical Research: Solid Earth*. Reprinted with permission by Wiley. Copyright 2018 American Geophysical Union.

high strength patches with increased normal stress and acting as barriers to inhibit seismic slip (Cloos, 1992; Scholz and Small, 1997; Kodaira *et al.*, 2000). Yang *et al.* [2013] demonstrated that the barrier effect of a seamount on megathrust rupture become stronger for increased seamount normal stress, larger height-to-width ratio, and shorter seamount-to-nucleation distance. Recently, Collot *et al.* (2017) suggested that the real scenario for oceanic relief subduction may depend on the relation between the height-to-width ratio of the oceanic reliefs and the subduction channel thickness, and in particular, for a low height-to-width ratio subducted relief with little detectable subduction channel, the irregularity may jag against the overriding plate and favor interplate coupling.

Another key factor in controlling rupture dynamics is the friction law on the fault interface. Many numerical studies of fault geometry effect on dynamic rupture (Oglesby and Archuleta, 2003; Duan and Oglesby, 2005b; Yang *et al.*, 2013; Fukuyama and Hok, 2015) utilize a linear slip-weakening (SW) friction law (Ida, 1972; Palmer and Rice, 1973; Andrews, 1976) to account for the shear stress breakdown process within the cohesion zone during rupture propagation (Yang *et al.*, 2013; Fukuyama and Hok, 2015). This classic friction law provides an effective means to reproduce unstable slip based on the fact that frictional strength falls as slip increases. As more frictional phenomena are observed in laboratory experiments, such as velocity dependence of steady-state friction and healing process of frictional strength, a modern form of friction law called rate- and state-dependent friction law (RSF) (Dieterich, 1978; Dieterich, 1979; Ruina, 1983) was proposed to capture these physical details in experimental observations. Recent development of experimental equipment allows us to perform high-speed friction

experiments (*Beeler et al.*, 2008; *Di Toro et al.*, 2011) at coseismic slip rates, and strong rate weakening behavior is observed. An improved model based on RSF to better fit such observations is proposed (*Rice*, 1999; *Rice*, 2006; *Beeler et al.*, 2008) and applied in rupture modeling (e.g. *Rojas et al.*, 2009; *Ryan and Oglesby*, 2014).

The RSF laws have been discussed to behave similarly to the standard SW law on a flat fault model (*Bizzarri et al.*, 2001; *Bizzarri and Cocco*, 2003) and produce an equivalent slip-weakening curve in dynamic rupture simulation. The RSF law with strong rate weakening can differ from the SW law by producing self-healing pulse-like rupture other than crack-like rupture (*Perrin et al.*, 1995; *Gabriel et al.*, 2012). However, it remains a question that whether the RSF laws and the SW law still behave similarly when dynamic rupture occurs on a nonplanar fault. A recent study by *Ryan and Oglesby* (2014) shows that different friction laws could lead to different jump distance for a step-over fault geometry, and specific frictional parameterizations could even generate previously unseen supershear rupture phenomenon. In this study, we conduct numerical experiments to investigate the roles of a large-scale seamount-like geometrical irregularity in earthquake rupture on subduction faults governed by various friction laws.

2.2 Fault Geometry and Stresses

In order to investigate the rupture behavior on nonplanar fault surfaces governed by different friction laws, we use the three-dimensional finite element code EQdyna (*Duan and Oglesby*, 2006; 2007; *Duan*, 2012) to carry out a series of dynamic rupture

simulations. We implement different forms of RSF laws into EQdyna in this study. EQdyna has been verified in the SCEC/USGS Spontaneous Rupture Code Verification Project (*Harris et al.*, 2009; *Harris et al.*, 2011), including the implementation of RSF laws. Specifically, for the purpose of this study, we use EQdyna to solve the SCEC TPV28 benchmark problem which tests various codes on bump geometry on strike-slip faults. The quantitative comparison from the SCEC/USGS Code Verification Web Server (<http://scecddata.usc.edu/cvws/>) based on metrics defined by *Barall and Harris* [2014] shows that the fine resolution results obtained by EQdyna (25 or 50 m) is in good agreement with those by other codes (http://scecddata.usc.edu/cvws/metric_cvv1_u1/tpv28/metric_cvv1_tpv28_ac_0.html). For coarse grid size (100 m), EQdyna shows much smaller RMS error in rupture time than other methods do as compared to the fine resolution results.

We construct a subduction fault plane embedded in a three-dimensional half-space linear elastic homogeneous isotropic continuum. The fault plane dips at an angle $\phi = 30^\circ$ and extends to the free surface. The finite element mesh is hexahedral, and we use a degeneration technique (*Duan*, 2012) to divide a hexahedron element into two wedge elements along the fault plane (Figure 2. 1a). The hexahedron elements have unequal edge lengths in order to fit the dipping angle of the fault, with $\Delta y = \Delta x \cos \phi$ and $\Delta z = \Delta x \sin \phi$. Here, x -axis is defined along the strike direction, y -axis is perpendicular to the strike direction, and z -axis is vertical and points upward.

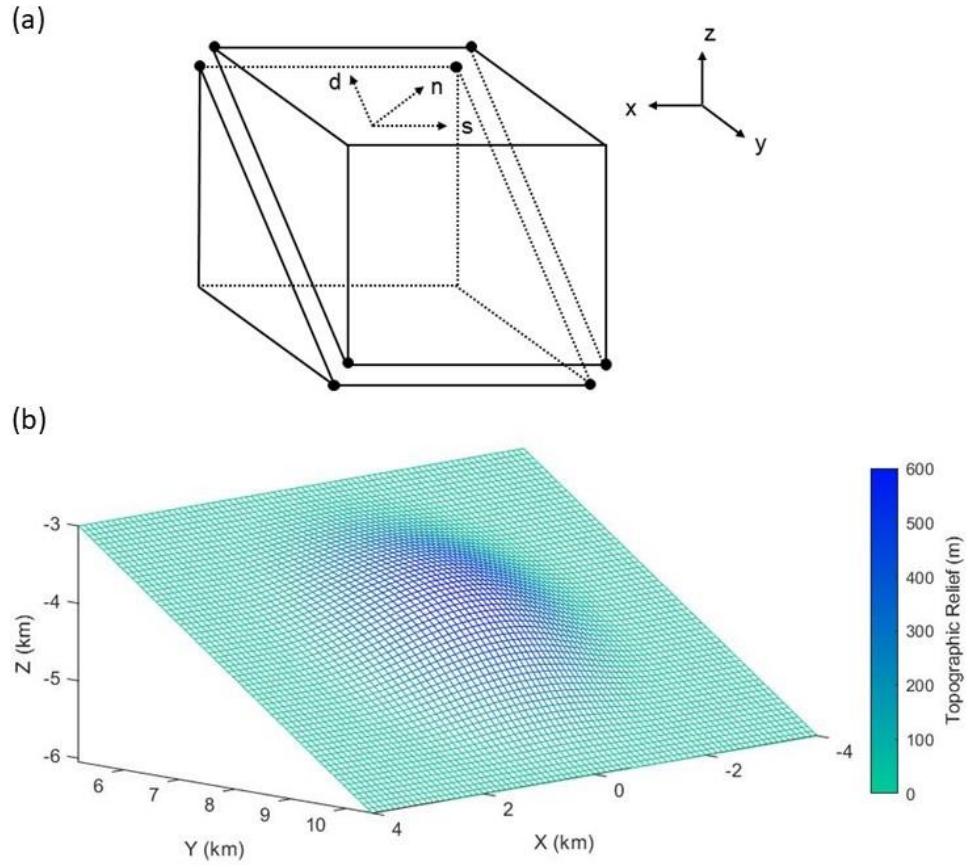


Figure 2. 1 (a) A hexahedral element degenerated into two wedge elements. Split nodes of the ideal dipping fault plane are separated for illustration purpose. A local coordinate system is shown on the fault surface, and a global coordinate system used for entire mesh generation is shown on the right. (b) The nonplanar part of the thrust fault model. The locally curved shape of the mesh represents a circular bump on the fault surface centered at 9 km along dip from the fault trace (not shown here). Note that the fault is embedded in a three-dimensional finite element domain.

In the mesh, a bump is constructed explicitly on the fault plane to represent the subducted seamount geometry. To do that, we use a mesh morphing technique (*Barall, 2009*), which moves the on-fault nodes in a direction perpendicular to the ideal flat fault plane to create the bump geometry. The deviation of the morphed fault surface from the original fault plane is accommodated by the surrounding finite element mesh with no more than 10% distortion in each element. The function we use to describe the spatially distributed deviation of the bump is

$$h(r) = \frac{A}{2} \left[1 + \cos\left(\frac{\pi r}{R}\right) \right], \quad \text{if } r < R, \quad (2.1)$$

where A is the height of the bump and r is the distance between any location on the reference planar fault and the bump center. In our model, the center of the bump is positioned at 9 km from the free surface along dip direction and 0 km along the strike direction (Figure 2. 1b).

We assume a pure-thrust faulting stress environment with the minimum principal effective stress σ_3 in the vertical direction, the intermediate principal effective stress σ_2 in the strike direction, and the maximum principal effective stress σ_1 perpendicular to the strike direction in the horizontal plane. All three principal stresses are assumed to be linearly increasing from the free surface to 2 km at depth. In particular, σ_3 is the lithostatic pressure minus hydrostatic pore pressure. Below 2 km at depth, effective principal stresses are assumed constant due to overpressurization. The initial normal stress σ_n and initial shear stress τ_0 on the fault are assigned by resolving the effective stress tensor onto the

fault surface. On the planar part of the fault, σ_1 and σ_3 are constructed as follows to provide certain effective compressive normal traction and shear traction,

$$\sigma_1 = \sigma_n + \frac{\tau_0}{\tan \phi}, \quad (2.2)$$

$$\sigma_3 = \sigma_n - \tau_0 \tan \phi. \quad (2.3)$$

Specifically, we assume constant effective normal traction as 50 MPa and constant shear traction as 30 MPa at depth below 2 km, which correspond to $\sigma_1 = 102$ MPa and $\sigma_3 = 32.6$ MPa. On the nonplanar part, the fault surface orientation varies spatially and gives heterogeneous local effective normal and shear tractions. Since the lateral slopes of the bump are tilted toward the strike direction, the intermediate principal stress σ_2 is also involved in determining the initial tractions on the bump. For this reason, we assume

$$\sigma_2 = \frac{\sigma_1 + \sigma_3}{2}. \quad (2.4)$$

Figure 2. 2 shows the initial stress distribution on the thrust fault with a 600 m high seamount with a 6 km basal diameter. The bump sits on top of the footwall and intrudes into the hanging wall. When the thrust fault slides, the hanging wall moves updip relative to the footwall. Therefore, compared to the background level, the effective normal stress on the bump is more compressive on the downdip slope and less compressive on the updip slope.

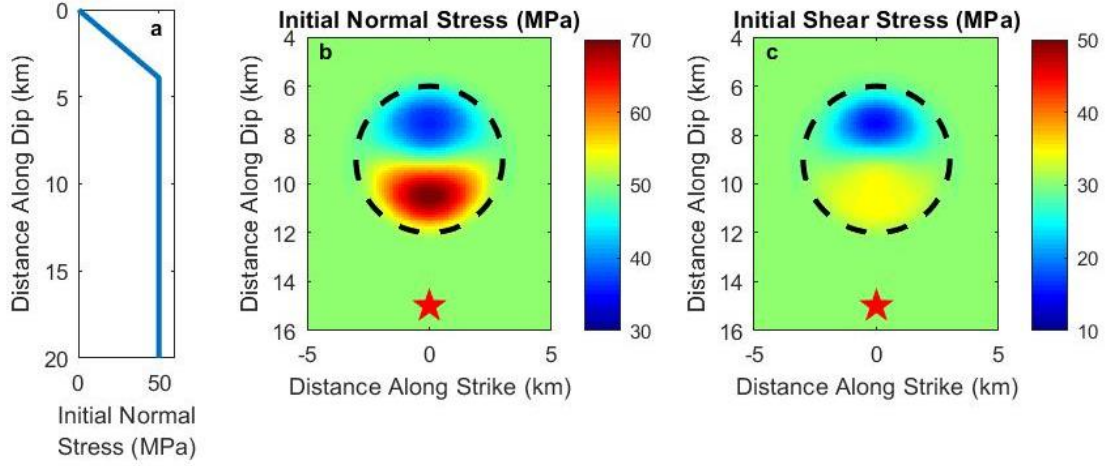


Figure 2. 2 The profile of background initial normal stress along dip direction (a), initial normal stress (b) and initial shear stress (c) in the vicinity of the seamount, respectively. Black circles and red stars in (b) and (c) denote the circular boundary of the bump on the fault and the hypocenter where rupture begins, respectively.

2.3 Functional Forms of Various Friction laws

The explicit finite element code EQdyna uses the standard FEM formulation to discretize the space domain as well as the central difference time integration method to explicitly evolve physical quantities with the diagonalized mass matrix. The code utilizes the traction-at-split-node (TSN) method (*Andrews, 1999; Day et al., 2005*) to allow displacement discontinuity on the fault surface and to couple frictional boundary conditions to the FEM model. The widely used linear slip-weakening law (SW) defines μ as a function of slip distance δ :

$$\mu = \mu_s + (\mu_s - \mu_d) \min\left(\frac{\delta}{d_0}, 1\right), \quad (2.5)$$

where μ_s and μ_d are the static and dynamic friction coefficient, respectively, and d_0 is a frictional parameter called the critical slip distance over which friction drops from μ_s to μ_d . On the other hand, the laboratory-derived rate- and state- friction laws define μ as a function of slip rate V and state variable θ :

$$\mu = f_0 + a \ln \frac{V}{V_0} + b \ln \frac{V_0 \theta}{L}, \quad (2.6)$$

where a and b are constitutive frictional parameters determined in laboratory experiments; L is the characteristic slip distance for the exponential healing process after a velocity stepping; f_0 is a reference friction coefficient associated with a reference steady state slip rate V_0 . Here state variable θ is a description of sliding history and evolves according to various evolution laws.

Since μ is not defined at $V = 0$ in this classic form of RSF, a modified form is proposed (*Lapusta et al.*, 2000) as

$$\mu = a \operatorname{arcsinh} \left[\frac{V}{2V_0} \exp \left(\frac{f_0 + b \ln \frac{V_0 \theta}{L}}{a} \right) \right], \quad (2.7)$$

with aging law

$$\frac{d\theta}{dt} = 1 - \frac{V\theta}{L}, \quad (2.8)$$

describing the evolution process of θ . This modified form of RSF with aging law is denoted as RS-A here. Another variant form of RSF is the slip law (RS-S), which is defined in a slightly different form:

$$\mu = a \operatorname{arcsinh} \left[\frac{V}{2V_0} \exp \left(\frac{\Psi}{a} \right) \right], \quad (2.9)$$

where state variable Ψ evolves according to the following set of equations:

$$\frac{d\Psi}{dt} = -\frac{V}{L}(\Psi - \Psi_{ss}), \quad (2.10)$$

$$\Psi_{ss} = a \ln \left[\frac{2V_0}{V} \sinh \left(\frac{f_{ss}}{a} \right) \right], \quad (2.11)$$

$$f_{ss} = f_0 - (b - a) \ln \frac{V}{V_0}, \quad (2.12)$$

Both the RS-A and RS-S laws are proposed to describe the friction behavior observed at low slip rates in laboratory experiments. However, earthquake ruptures involve high slip rates at which microscopic asperities in the thin slip zone may experience transient heating that thermally weakens the frictional strength. A modified model based on rate- and state-friction to better fit this flash heating phenomenon is proposed (*Rice, 1999; Rice, 2006; Beeler et al., 2008*) and applied in rupture modeling (e.g. *Rojas et al., 2009; Ryan and Oglesby, 2014*). In this model, the steady state friction coefficient f_{ss} defined in the RS-S law is retained for low slip rate condition and is renamed low velocity steady state friction coefficient f_{LV} . A new steady state friction coefficient is defined as:

$$f_{ss} = f_w + \frac{f_{LV} - f_w}{\left[1 + \left(\frac{V}{V_w}\right)^8\right]^{1/8}}, \quad (2.13)$$

where f_w is the weakened state friction coefficient and V_w is the characteristic weakening velocity. This modified form of RSF introduces strong velocity weakening when velocity is at high levels. We denote this form by RS-FH. Section 2.4 gives more information about the implementation of the rate- and state-dependent friction laws.

Model and frictional parameters are listed in Table 2. 1. Here we consider a 40 km by 20 km thrust-type fault which is able to host an earthquake of $M \sim 7$. The basal diameter of the seamount is 6 km, while its height varies within 15% of its basal diameter. In reality, the height of seamounts varies from 0 to 6 km and is less than 10% of its base width (*Wang and Bilek, 2011*).

Frictional parameters are selected based on comparison criteria discussed in the next section. In all RSF cases, a small initial slip velocity $V_{ini} = 10^{-6}$ m/s in along-dip direction is assigned throughout the planar part of the fault to provide a reasonable static friction of 0.6. The magnitude of the slip velocity on the bump is still assumed uniform but its direction is parallel to the local initial shear traction. Initial state variable is determined by initial friction coefficient and initial slip velocity according to the RSF equations for consistency.

Table 2. 1 Model and frictional parameters

Parameter	Value
<i>FEM Model Parameters</i>	
Fault length along strike	40 km
Fault width along dip	20 km
Dip angle, ϕ	30°
Loading slip rate, V_{ini}	10 ⁻⁶ m/s
S-wave speed, v_s	3464 km/s
P-wave speed, v_p	6000 km/s
Density, ρ	2670 kg/m ³
Time step, Δt	0.005 s
Element edge length in x direction, Δx	100 m
<i>Frictional Parameters</i>	
<i>SW</i>	
Static frictional coefficient, μ_s	0.78
Sliding frictional coefficient, μ_d	0.55
Critical slip-weakening distance, d_0	0.18 m
<i>RSF</i>	
Rate- and state- friction parameter a	0.016
Rate- and state- friction parameter b	0.02
Reference slip velocity, V_0	10 ⁻⁶ m/s
Steady state friction coefficient, f_0	0.6
Characteristic slip L for RS-A	0.012 m
Characteristic slip L for RS-S	0.08 m
Characteristic slip L for RS-FH	0.08 m
Weakened state friction coefficient, f_w	0.547
Characteristic weakening velocity, V_w	0.1 m/s

Dynamic ruptures are initiated by artificial shear stress perturbation within a circular nucleation patch of 3 km radius centered at 15 km downdip and 0 km along strike. For the SW law, the friction begins to drop when the shear traction reaches the prescribed frictional strength. For the RSF laws, however, an explicit criterion of frictional yielding

is not given in advance. The stress, slip rate and state variable evolve simultaneously in the nucleation phase, and a significant decrease in frictional resistance occurs when the state variable drops dramatically. Dynamic ruptures governed by the RSF laws are arrested at the buried fault edges by a strip of velocity strengthening zones of 3 km wide. For the SW law, a strip of a negative stress drop region of 3 km wide is given to stop ruptures at these fault edges.

2.4 Implementation of rate- and state-dependent friction laws in finite element methods

The frictional failure condition at on-fault split nodes is incorporated into the central time differencing scheme as follows (*Day et al.*, 2005):

$$v_i^\pm \left(t + \frac{\Delta t}{2} \right) = v_i^\pm \left(t - \frac{\Delta t}{2} \right) + \Delta t \cdot (M^\pm)^{-1} \cdot [R_i^\pm(t) \mp a(T_i(t) - T_i^0)], \quad (2.14)$$

$$d_i^\pm(t + \Delta t) = d_i^\pm(t) + \Delta t \cdot v_i^\pm \left(t + \frac{\Delta t}{2} \right), \quad (2.15)$$

where Δt is time step and a is fault surface area. The nodal mass on plus-side is defined as M^+ and the minus-side as M^- . The nodal velocity vectors on the two sides are denoted by v_i^\pm , and the nodal restoration forces are R_i^\pm , with subscript i denoting the nodal components in strike (s), dip (d) or normal (n) direction. The symbol T_i is the time-dependent nodal traction vector and T_i^0 is the initial traction vector. The shear component

of on-fault traction T_i is considered as the resistant force antiparallel to the slip velocity, with its magnitude τ being equal to the fault strength τ_c which is defined as $\tau_c = \mu\sigma_n$ with friction coefficient μ and normal traction $\sigma_n = T_{normal}$. In various frictional constitutive laws, the friction coefficient μ is a function of various on-fault kinematic quantities.

For the normal component of relative motion, *Day et al.* (2005) introduced a trial traction \tilde{T}_n in normal direction as follows:

$$\begin{aligned} \tilde{T}_n = T_n^0 + & \frac{M^+M^-(\dot{\delta}_n(t - \frac{\Delta t}{2}) + \Delta t^{-1}\delta_n(t - \frac{\Delta t}{2}))}{a\Delta t(M^+ + M^-)} \\ & + \frac{M^-R_n^+(t) - M^+R_n^-(t)}{a(M^+ + M^-)}. \end{aligned} \quad (2.16)$$

This trial traction enforces both velocity and displacement continuity and is applied in both the SW and RSF laws.

Shear slip velocity components $\dot{\delta}_i$ can be obtained through subtraction between particle velocities of split nodes:

$$\begin{aligned} \dot{\delta}_i \left(t + \frac{\Delta t}{2} \right) = & \dot{\delta}_i \left(t - \frac{\Delta t}{2} \right) + \frac{\Delta t [M^-R_i^+(t) - M^+R_i^-(t)]}{M^+M^-} \\ & - \Delta t \frac{(M^+ + M^-)}{M^+M^-} a [\tilde{T}_i - T_i(t)], \quad i = s, d. \end{aligned} \quad (2.17)$$

Day et al. (2005) also introduced a shear trial traction \tilde{T}_i to enforce shear velocity continuity between the split nodes across the fault:

$$\tilde{T}_i = T_i^0 + \frac{(M^+M^-)\dot{\delta}_i\left(t - \frac{\Delta t}{2}\right)}{a\Delta t(M^+ + M^-)} + \frac{M^-R_i^+(t) - M^+R_i^-(t)}{a(M^+ + M^-)}, \quad (2.18)$$

$$i = s, d.$$

In other words, such a trial traction will force the slip velocity between split nodes to vanish. Since friction is passive force which resists any relative motion between on-fault split nodes, the magnitude of actual traction should never be greater than the trial traction \tilde{T}_i . We can use \tilde{T}_i to reduce the expression of $\dot{\delta}_i\left(t + \frac{\Delta t}{2}\right)$:

$$\dot{\delta}_i\left(t + \frac{\Delta t}{2}\right) = c[\tilde{T}_i - T_i(t)], \quad i = s, d, \quad (2.19)$$

where $c = a\Delta t \frac{(M^+ + M^-)}{M^+M^-}$. Apparently, substituting \tilde{T}_i for $T_i(t)$ gives $\dot{\delta}_i\left(t + \frac{\Delta t}{2}\right) = 0$. If actual traction $T(t)$ is defined parallel to slip velocity, then $\dot{\delta}_i(t + \Delta t/2)$, \tilde{T}_i , and $T_i(t)$ are all parallel to one another. With this assumption, the vector equation above can be reduced to a scalar equation:

$$\dot{\delta}\left(t + \frac{\Delta t}{2}\right) = c [\tilde{T} - T(t)], \quad (2.20)$$

where $\dot{\delta}(t + \frac{\Delta t}{2}) = \sqrt{\dot{\delta}_s(t + \frac{\Delta t}{2})^2 + \dot{\delta}_d(t + \frac{\Delta t}{2})^2}$, $\tilde{T} = \sqrt{\tilde{T}_s^2 + \tilde{T}_d^2}$, $T(t) = \sqrt{T_s(t)^2 + T_d(t)^2}$. For the SW law, when friction level computed from the friction law is larger than the trial traction \tilde{T} , just set actual traction equal to trial traction and obtain a zero slip velocity to represent the locking state of the fault. When friction level becomes

less than \tilde{T} , the magnitude of actual traction should be friction itself and a certain level of slip velocity is obtained.

The RSF laws, however, provide a means to relate shear stress $\tau_c = T(t)$ to slip velocity and state variable:

$$\tau_c = \tau_c(\dot{\delta}, \theta) = \mu(\dot{\delta}, \theta)\sigma_n, \quad (2.21)$$

$$\dot{\theta} = g(\dot{\delta}, \theta). \quad (2.22)$$

As pointed out by *Rojas et al.* (2009), an explicit time stepping scheme is not appropriate for RSF laws because using explicit scheme to integrate RSF laws and equations of motion results in a set of stiff partial differential equations that require extremely small time steps to ensure numerical stability at extremely small slip velocity. The trapezoidal method is one of the implicit methods they proposed to address this issue. Also, this method is nominally of second-order accuracy. It defines the traction at the time t as the average of frictional tractions computed from slip velocities at $t - \frac{\Delta t}{2}$ and $t + \frac{\Delta t}{2}$. The traction at time $t - \frac{\Delta t}{2}$ is parallel to $\dot{\delta}_i(t - \frac{\Delta t}{2})$ and the traction at time $t + \frac{\Delta t}{2}$ is parallel to $\dot{\delta}_i(t + \frac{\Delta t}{2})$, so we have:

$$T_i(t) = \frac{1}{2}\sigma_n \left\{ \mu \left[\dot{\delta} \left(t - \frac{\Delta t}{2} \right), \theta(t) \right] \frac{\dot{\delta}_i \left(t - \frac{\Delta t}{2} \right)}{\dot{\delta} \left(t - \frac{\Delta t}{2} \right)} + \mu \left[\dot{\delta} \left(t + \frac{\Delta t}{2} \right), \theta(t) \right] \frac{\dot{\delta}_i \left(t + \frac{\Delta t}{2} \right)}{\dot{\delta} \left(t + \frac{\Delta t}{2} \right)} \right\}, \quad i = s, d, \quad (2.23)$$

where $\dot{\delta}(t - \frac{\Delta t}{2}) = \sqrt{\dot{\delta}_s(t - \frac{\Delta t}{2})^2 + \dot{\delta}_d(t - \frac{\Delta t}{2})^2}$. The state variable θ is defined coincidentally with slip δ and time-staggered with slip rate $\dot{\delta}$, such that an explicit updating scheme for the state evolution law can be obtained:

$$\theta(t + \Delta t) = \theta_{ss} + [\theta(t) - \theta_{ss}] \exp \left[-\frac{\dot{\delta} \left(t + \frac{\Delta t}{2} \right) \Delta t}{L} \right], \quad (2.24)$$

where L denotes the characteristic slip distance for RSF, and θ_{ss} denotes the state variable for steady-state sliding. This exponential solution is a good approximation to the evolution equation with second order accuracy according to the analysis by *Noda and Lapusta* (2010).

Substituting (2.23) into (2.20) yields:

$$\dot{\delta} \left(t + \frac{\Delta t}{2} \right) + \frac{1}{2} c \sigma_n \mu \left[\dot{\delta} \left(t + \frac{\Delta t}{2} \right), \theta(t) \right] = c \tilde{T}', \quad (2.25)$$

where $\tilde{T}' = \sqrt{(\tilde{T}'_s)^2 + (\tilde{T}'_d)^2}$, and $\tilde{T}'_i = \tilde{T}_i - \frac{1}{2} \sigma_n \mu \left[\dot{\delta} \left(t - \frac{\Delta t}{2} \right), \theta(t) \right] \frac{\dot{\delta}_i(t - \frac{\Delta t}{2})}{\dot{\delta}(t - \frac{\Delta t}{2})}$, $i = s, d$.

We use Newton's method to solve the scalar equation (2.25) for $\dot{\delta} \left(t + \frac{\Delta t}{2} \right)$.

2.5 Comparing Frictional Behaviors of Various Friction Laws

For the spontaneous dynamic rupture problem, the slip-weakening behavior of friction is a critical factor in reproducing self-sustainable rupture propagation. All the friction laws discussed here share this common feature, although they describe this property based on their own mathematical functional forms and parameters. In the SW

law, this property is explicitly described as a linear relation between stress and slip, whereas in the RSF laws, the slip-weakening behavior is a consequence of the velocity-weakening mechanism in the RSF laws with a special condition of RSF parameters $a - b < 0$. One can produce different friction breakdown processes by varying the frictional parameters. In order to examine the effect of various friction laws on the dynamic rupture on nonplanar fault geometry, it is desirable to make the rupture behaviors governed by various friction laws similar to one another before they hit the bump.

First, all the shear stresses governed by various friction laws should yield at a similar yield stress τ_u , and then drop to a similar dynamic stress τ_d as slip increases, as shown in the stress-slip curves in Figure 2. 3. However, while this setting is applicable for a planar fault, it does not hold when the fault is nonplanar. That is because the yield stresses between the SW law and the RSF laws are defined in different ways. In the SW law, the yield stress τ_u is given as

$$\tau_u = \mu_s \sigma_n. \quad (2.26)$$

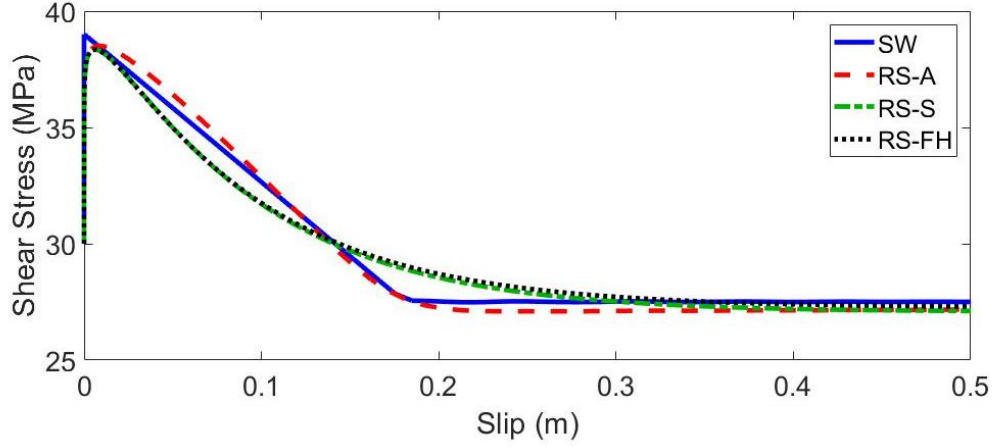


Figure 2. 3 Comparison of shear stresses as a function of slip at the hypocenter for all four types of friction laws with frictional parameters listed in Table 1. In all friction laws the stress first rises from initial level (30 MPa) to the static friction (~ 38 MPa), and then drops to the dynamic friction (~ 27.3 MPa) over certain amount of slip after yielding.

As the initial normal stress σ_n on the compressional side of a bump increases, it is reasonable that there is a proportional increase in yield stress. On the other hand, although the RSF laws with velocity-weakening parameters are shown to be capable of reproducing the slip-weakening property, the yield stress in these laws is mainly characterized by a “jump” added to the initial shear stress, the so-called direct effect in the RSF laws. Assuming negligible change in state variable, the yield stress τ_u can be estimated as (Bizzarri and Cocco, 2003)

$$\tau_u = \tau_0 + \Delta\tau \approx \tau_0 + a\sigma_n \ln \frac{V_{dyn}}{V_{ini}}, \quad (2.27)$$

where τ_0 denotes the initial shear stress, $\Delta\tau$ denotes the stress excess from initial shear stress to yield stress, and V_{dyn} denotes the coseismic slip velocity, which could be reasonably assumed as a constant of 1 m/s. This estimate holds for all three types of RSF laws, since the main difference between the RSF laws is the evolution law of the state variable, which is assumed an invariant when we estimate the yield stress. Therefore, we only consider one yield stress estimate for all three RSF laws. We equate the RSF yield stress to the SW yield stress on the planar part of the fault

$$\mu_s \sigma_n \approx \tau_0 + a \sigma_n \ln \frac{V_{dyn}}{V_{ini}}. \quad (2.28)$$

But this relation may not hold when initial stresses are heterogeneous, especially when the initial stress variation is only determined by fault geometry and is independent of the types of friction laws. Figure 2. 4a and b show the profiles of heterogeneous initial normal and shear stresses along dip direction at the center of the bump. Given the pure-thrust faulting environment, the bump surface orientation gives low normal stress on the updip slope (6 to 9 km) and high normal stress on the downdip slope (9 to 12 km). The magnitude of normal stress variation increases as the bump height increases. The initial shear stress distribution, however, is less straightforward. While the updip slope shows significant reduction in shear stress as the bump height increases, the downdip slope has limited increase in shear stress. The reason is that the maximum possible shear stress in the pure-thrust environment with $\sigma_1 = 102$ MPa and $\sigma_3 = 32.6$ MPa in this study is $(\sigma_1 - \sigma_3)/2 = 34.7$ MPa, which is close to the background shear stress of 30 MPa determined by the thrust fault surface dipping at 30° . Therefore, as the height of the bump increases,

the shear stress cannot increase by more than 4.7 MPa. Given such initial stress distribution, Figure 2. 4c estimates the corresponding yield stress in RSF laws according to equation (15). The RSF yield stress profiles appear to be analogous to the initial shear stress profiles in Figure 2. 4b, in contrast to the expectation of SW yield stress which is proportional to the initial normal stress according to equation (14). Figure 2. 4d shows the variation of stress quantities at the most compressional location on the bump (at 10.5 km along dip in Figure 2. 4a) as the height of the bump varies. At this location, the initial normal stress monotonically increases from 50 MPa to 80 MPa as the height of bump increases from 0 to 900 m, whereas the initial shear stress first increases from 30 MPa to 34 MPa but then decreases back to 32 MPa. The SW law gives a yield strength solely proportional to the initial normal stress, so the variation of the yield stress follows the trend of the variation of the initial normal stress as the bump height increases, and the yield stress reaches its maximum of 62 MPa when the bump is 900 m high. In contrast, the RSF laws give a yield strength based on the initial shear stress and the estimated stress excess, of which only the latter one is approximately proportional to the initial normal stress. In our model, since the initial shear stress is much greater than the stress excess, the RSF yield stress is dominated by the initial shear stress and its variation follows a trend similar to the variation of the initial shear stress. Therefore, as the height of the bump increases, the RSF yield stress does not increase as much as the SW yield stress does but varies based on the variation of both initial shear and normal stresses. Interestingly, as the height of the bump changes from 600 m to 900 m, the initial normal stress increases and the initial shear stress decreases. These two initial stresses change in opposite directions

and cancel out their effect on RSF yield stress, resulting in a nearly unchanged yield stress of 47 MPa, even though the height of the bump increases. This special case suggests that for RSF laws, a bump with greater height does not necessarily provide higher local strength than a bump with lower height.

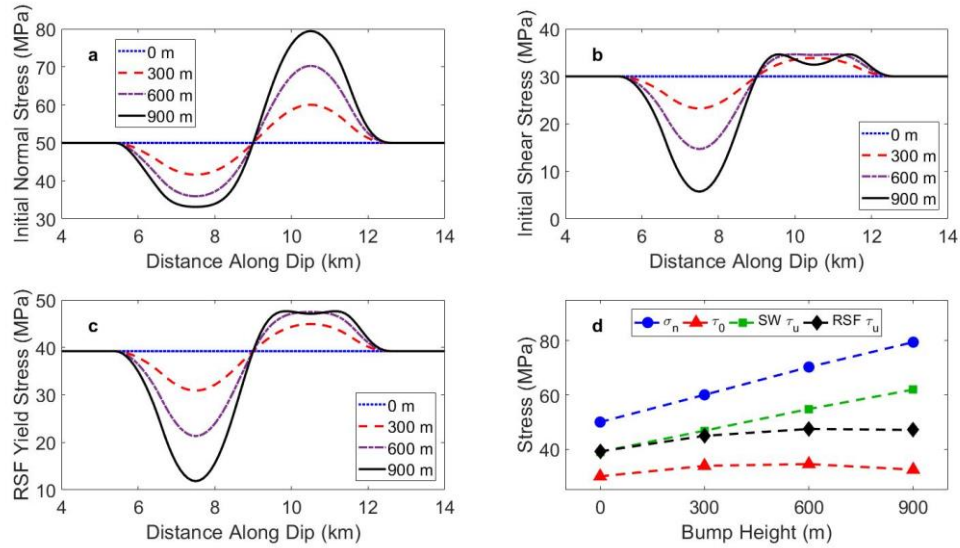


Figure 2.4 (a) and (b) show the initial normal and shear stress profiles along dip direction through the center of the bump for various bump heights. (c) shows the profiles of estimated yield stress in RSF law. (d) shows the variation of stress quantities at the most compressive location (at 10.5 km along dip) on the bump as a function of the height of the bump, including initial normal stress σ_n , the initial shear stress τ_0 , the yield stress τ_u estimated by the SW law and the yield stress τ_u estimated by the RSF laws.

Besides the yield stresses, the stress breakdown process after friction yields also show great difference between different friction laws. Based on their slip-weakening

behavior (Figure 2. 3), these four types of friction laws can be categorized into two groups, one with linearly weakening behaviors and the other with the exponentially decaying behaviors. The shape of weakening curves for the RS-A law and the SW law are similar to each other, exhibiting a linear decrease in friction with respect to the increase of sliding distance and a sharp kink turning the linearly weakening friction to a constant dynamic friction level. *Bizzarri and Cocco* (2003) has derived an estimate of the equivalent critical distance for the RS-A law as

$$d_0^{RS-A} = L \ln \left(\frac{\theta_{ini} V_d}{L} \right), \quad (2.29)$$

where V_d is the slip velocity at the end of the weakening process when the traction is at its minimum. They also point out that when simulation starts with steady state sliding, θ_{ini} equals to L/V_{ini} and thus d_0^{RS-A} is linearly related to L with a proportionality of about 15. In our models, the selection of $L = 0.012$ m for the RS-A law and $d_0 = 15L = 0.18$ m for the SW law verifies this point and yields similar stress breakdown processes between these two laws (Figure 2. 3).

The stress-slip curves for the RS-S and RS-FH laws, however, show an exponentially decaying pattern as the shear stress gradually evolves from the yield strength to the dynamic friction with respect to the slip. One way to compare this group with the linearly weakening group is to compare fracture energy among all the friction laws (*Ryan and Oglesby*, 2014), since the fracture energy is critical for self-sustaining rupture propagation and determines rupture speed (*Fukuyama and Madariaga*, 2000). As a lumped parameter representing all kinds of energy dissipated in the cohesive zone, the

fracture energy is defined as the work done against the friction excess $[\tau(\delta) - \tau_d]$ over the critical distance d_0 :

$$g_c = \int_0^{d_0} [\tau(\delta) - \tau_d] d\delta, \quad (2.30)$$

where $\tau(\delta)$ is the friction as a function of slip. For the SW law with a linear function for $\tau(\delta)$, $g_c = \frac{1}{2}(\tau_u - \tau_d)d_0$. The RS-A law can yield the same fracture energy if the stress-slip curve matches the one in the SW law. For the RS-S law, *Ampuero and Rubin (2008)* analyze theoretically the fracture energy by integrating equation (18) and show that the equivalent slip-weakening critical distance d_0^{RS-S} in the sense of fracture energy is proportional to the characteristic slip parameter L . In the light of their work, d_0^{RS-S} is approximately twice of L . Here we integrate g_c numerically for both the RS-S and RS-FH laws and find that $L = 0.08$ m, a value slightly less than half of d_0 in the SW law, makes the fracture energies for both RS-S and RS-FH laws equivalent to the ones in the SW and RS-A cases.

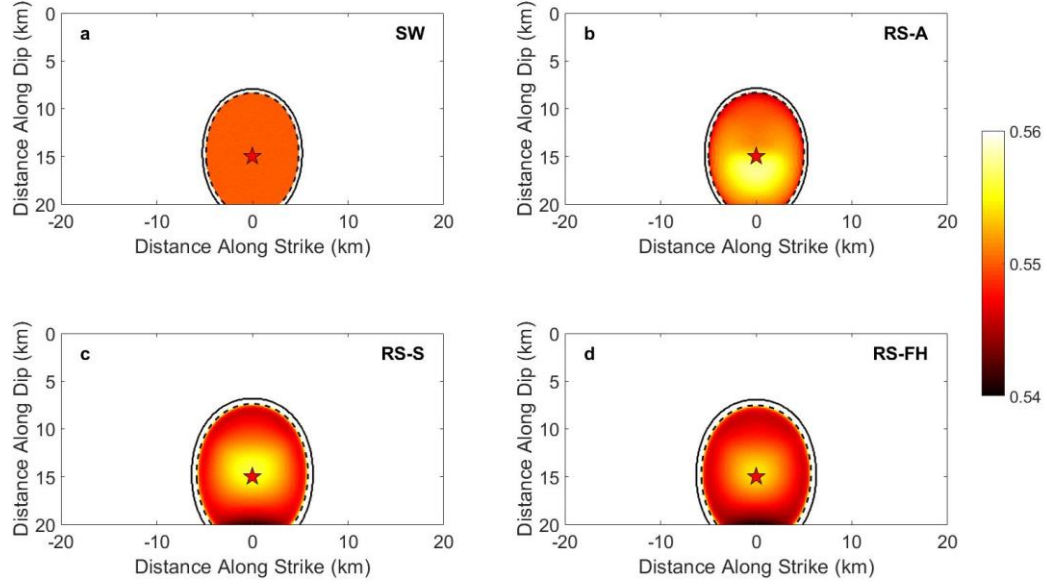


Figure 2. 5 Spatial distributions of the dynamic friction coefficient in various friction laws at 4 s. The solid and dashed lines denote the leading and trailing edges of the propagating rupture front, respectively. The area within the dashed line has been ruptured at this moment and is sliding with spatially varying dynamic friction coefficient below 0.56. The area outside the dashed line has friction coefficient above 0.56 and is not color-coded, including the intact area outside the solid line and the cohesive zone between the solid line and the dashed line.

Besides the fracture energy, we observe in practice that the rupture speed is also sensitive to the level of dynamic friction coefficient which is a constant value in the SW law but a variable quantity in the RSF laws controlled by frictional parameters ($a - b$) and local slip velocities. A theoretical dynamic friction level for the RS-A law equivalent to the SW law is given by *Bizzarri and Cocco* (2003), which is defined at the moment when slip reaches the aforementioned equivalent critical slip distance d_0^{RS-A} in the RSA law. However, unlike the SW law, the dynamic friction coefficient in all RSF laws is time

variable and thus shows spatial heterogeneity as the rupture grows. Figure 2. 5 compares the friction coefficient distribution on a reference, planar fault (i.e., the bump is removed) with the four friction laws at 4 s, and all of them show a ruptured area at a dynamic friction coefficient level around 0.55. This quantity is exactly 0.55 in the SW law and uniformly distributed over the SW ruptured area. However, in all RSF cases it varies spatially inside the ruptured area. Part of the RSF ruptured area, mainly at the center, has a dynamic friction coefficient slightly higher than 0.55, while the rest of the ruptured area, mainly close to the rim of the ruptured area, has a dynamic friction coefficient slightly lower than 0.55. Such spatial distribution comes from the fact that as slip increases, the rate- and state-dependent friction in the cohesive zone first drops to a relatively lower level and then rises back to a slightly higher level. As pointed out by *Bizzarri and Cocco* (2003), such rise in dynamic friction coefficient follows the relation between steady state friction and slip velocity described by equation (12). In a velocity weakening region where $a - b < 0$, once the slip velocity starts to decrease, the corresponding steady state friction coefficient will increase accordingly. Therefore, the center part of the RSF ruptured area where stress drop occurs earlier and local slip velocity is lower has a higher dynamic friction coefficient than the area closer to the rupture front. In addition, this phenomenon varies among the three RSF laws, which results in slight difference in their dynamic friction coefficient distributions. In the RS-A law, the dynamic friction heals and approaches the steady state friction level immediately after stress drops, resulting in a relative large area of dynamic friction coefficient higher than 0.55. In the RS-S law, such area is smaller because the dynamic friction coefficient only heals slightly and has not reached the theoretical steady

state level yet. In the RS-FH law, this area is even smaller because the dynamic friction reaches a preset value when slip velocity is higher than the characteristic weakening velocity V_w , and starts to heal only when slip velocity drops back to a level lower than V_w . In practice, we find that if the dynamic friction coefficient in the SW law is set to be equal to the theoretical equivalent in the RS-A law, i.e., the lower value immediately behind the rupture front, the SW law always generate stronger ruptures with larger rupture velocity and larger slip velocity than the RS-A law, because the dynamic friction coefficient in the SW law remains constant and does not rise after stress drop, which results in more release of strain energy and thus faster rupture propagation and slip rate in the cohesive zone.

In this study, instead of the theoretical equivalent, we select 0.55 as the dynamic friction coefficient in the SW law which has an effect on dynamic ruptures equivalent to the average effect of the heterogeneous dynamic friction coefficient distribution in the RS-A law. We also slightly adjust the preset high-speed friction coefficient in the RS-FH law case to match the dynamic rupture of the RS-S law. As shown in Figure 2. 6, the moment rate function of the dynamic rupture on the planar fault governed by the SW law matches the one governed by the RS-A law, and the moment rate function of the RS-S law also matches the one of the RS-FH law. However, there is still intrinsic difference between the linearly weakening group and the exponentially decaying group. The exponentially decaying group has a steeper initial slope in their weakening process (Figure 2. 3) and therefore releases energy earlier and faster than the linearly weakening group. This is consistent with observations in previous numerical studies comparing linear and non-linear slip-weakening friction laws (*Dunham, 2007; Latour et al., 2011*), which

demonstrate that steeper initial weakening slope leads to shorter nucleation length and earlier initiation time for rupture initiation.

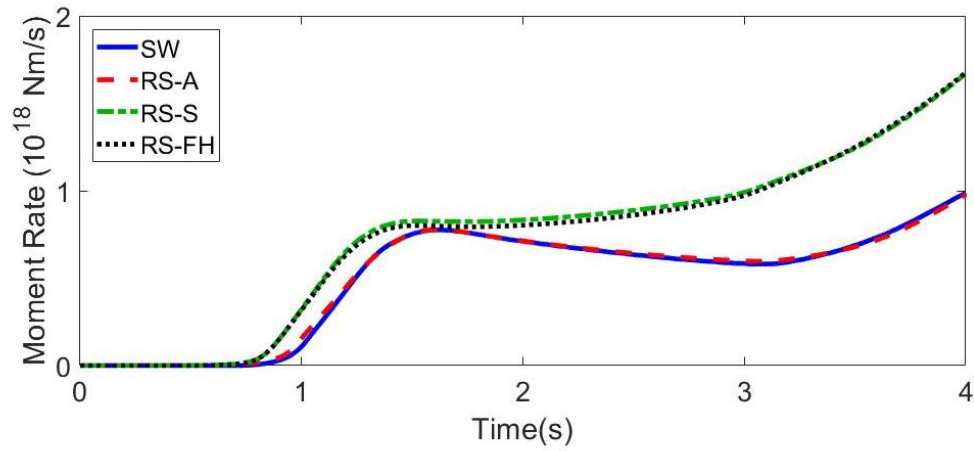


Figure 2. 6 Moment rate functions of dynamic ruptures on planar faults governed by various friction laws. The curves in each group of friction laws are nearly identical using the frictional parameters selected based on the assumption of equal fracture energy and equal average dynamic friction between friction laws. However, during rupture nucleation (0 to 2 s), the moment rate of the exponentially decaying group (RS-S and RS-FH) accelerates earlier than the linearly weakening group (SW and RS-A). After the rupture leaves the nucleation patch (2 to 4 s), the former group has reached a higher moment rate than the latter group.

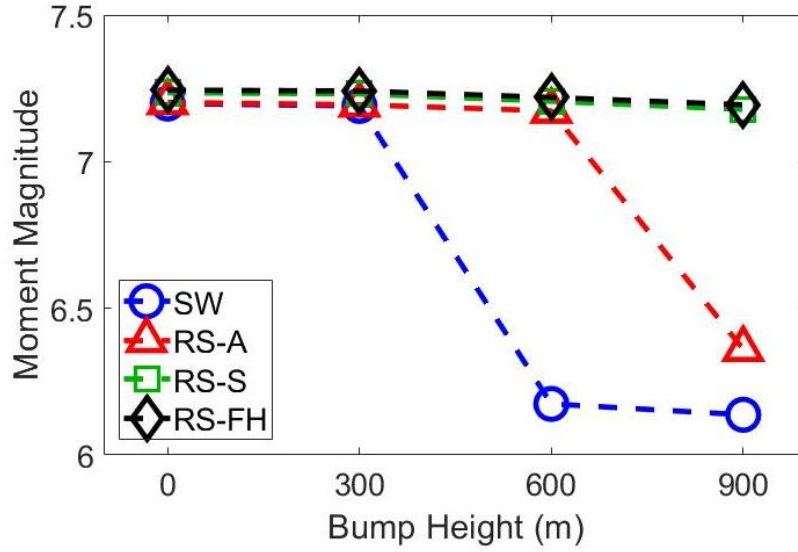


Figure 2. 7 The moment magnitude variation of simulated dynamic ruptures as the height of the bump varies. The results of four types of friction laws are shown for comparison.

2.6 Modeling Results

To study the large-scale bump geometry effect on earthquake rupture governed by the various friction laws, we carried out four sets of numerical experiments corresponding to the four friction laws. Each set of experiments comprises one case with a planar fault as reference and another three cases with a nonplanar fault with a bump of various heights (300 m, 600 m and 900 m, respectively) and the same basal diameter of 6 km. Since the hypocenter is located downdip of the bump, the rupture would first enter the downdip slope of the bump where local yield strength is relatively high. Depending on how high the yield strength is, the rupture may or may not be blocked by the downdip side of the

bump. In Figure 2. 7, we obtain the final moment magnitude of each dynamic rupture simulation for general comparison of effects of the bump geometry with the various friction laws. For a planar fault with 0m height for the bump, the four friction laws give similar magnitudes about 7.2 for the simulated earthquakes, which is a consequence of our carefully selected frictional parameters and a finite fault surface, except that the exponentially decaying group has slightly higher magnitude than the linearly weakening group mainly due to their different stress decaying styles. Compared to the planar fault, the introduction of a 300 m high bump to the fault surface causes only tiny decrease in the resulting moment magnitude for all friction laws. When the height of the bump becomes 600 m, the magnitude of the simulated earthquake governed by the SW law falls to 6.2 while the others are still barely affected. When the height of the bump becomes 900 m, both the RS-A law and the SW law show large drop in magnitude, but the RS-S law and the RS-FH law are still able to produce ruptures almost as large as the ones on a planar fault. A straightforward explanation for such a reduction in final moment magnitude is that when the bump becomes higher than a certain height value, its yield strength on the downdip slope becomes high enough to stop a rupture from further propagation to the whole fault area and therefore, limits the ruptured area and the size of the event. In our SW experiments, the dynamic rupture starts to be limited when the bump is 600 m high. But for the RSF experiments, the ruptures are still allowed to pass through by the RSF yield strength, since the RSF laws always determine a yield stress on the compressional slope lower than the one determined by the SW law.

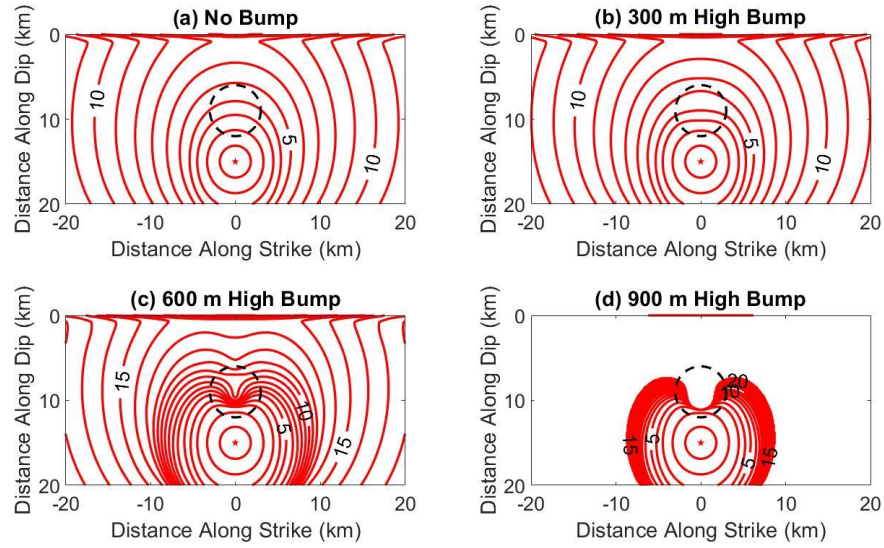


Figure 2. 8 Comparison of rupture time contours of dynamic rupture simulations governed by the RS-A law on a planar fault (a) and a nonplanar fault with a 300 m high bump (b), a 600 m high bump (c) and a 900 m high bump (d). The contour interval is 1 s. The black dashed circle in each contour denotes the position of the bump. The rupture in (d) is terminated by the bump and the blank area outside the 20 s rupture time contour line is not ruptured.

However, the yield stress of the bump is not the only factor that affects rupture dynamics. When the bump is 900 m high, the RS-A simulation gives a reduced magnitude while the other two RSF simulations do not, although all three of them have approximately the same yield stress level on the bump. Figure 2. 8 shows the rupture time contours of the RS-A cases with the various bump heights from 0 to 900 m. Rupture time is defined as the time when the slip velocity at that location exceeds 0.001 m/s, which implies the arrival of the rupture at that location. The rupture time contour for the case without a bump shows very smooth contour lines in the assumed bump area. Compared to this reference case, the contour lines in the bump area in the case with a 300 m high bump are slightly

distorted, with their intervals narrower on the downdip slope and wider on the updip slope, which suggests slower rupture speed on the downdip slope and faster rupture speed on the updip slope. Affected by this 300 m high bump, the total time to rupture the whole fault surface is approximately 1 s longer than the reference case. For a 600 m high bump, its influence on rupture time contour is much more significant. Contour lines from 3 s to 10 s are clustered at the downdip slope, mainly because the yield strength is strongly resisting rupture propagation in this area. These contour lines are also very narrow at other locations where the fault surface is planar, suggesting that the rupture responds to the barrier as a whole rather than just being affected locally. At 10 s, the downdip slope finally yields and the rupture resumes its propagation until it reaches the fault boundary. Due to the barrier effect of the bump, the whole rupture process is approximately 7 s longer than the reference case, but the final moment magnitude is still comparable to the reference case because it does rupture the whole fault surface. In the case with a 900 m high bump, the rupture time contour lines since 3 s are all clustered in front of the bump. The rupture is not able to overcome the barrier part of the bump, and therefore, the size of the ruptured area is limited and the final moment magnitude in this case is significantly reduced. In all these cases, there are rupture times recorded at the ground surface before the dynamic rupture reaches the fault traces, because seismic waves radiated from the hypocenter reach the ground surface faster than the rupture and easily trigger minor slip due to the low normal stress condition near the ground surface (Figure 2. 2a).

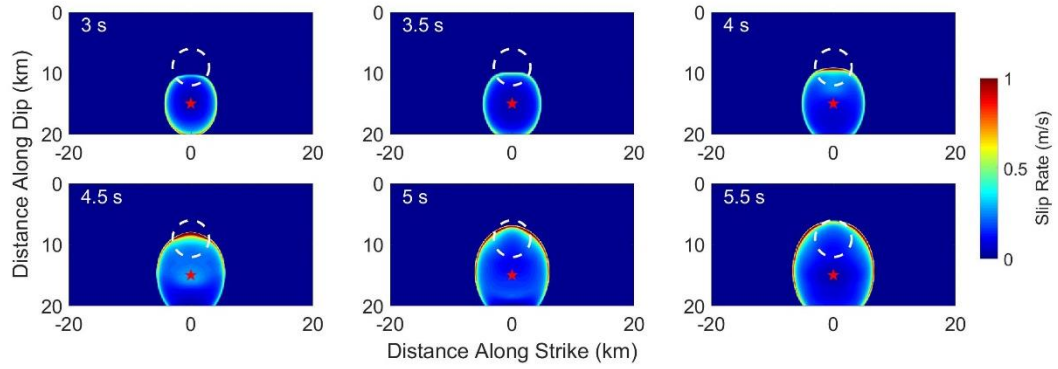


Figure 2. 9 Snapshots of the slip rate spatial distribution for the dynamic rupture simulation governed by the RS-A law on a nonplanar fault with a 300 m high bump. The white dashed circle in each snapshot denotes the position of the bump. Same for the following figures.

More details can be observed by looking at the snapshots of slip rate distributions. Starting with a nonplanar fault with a 300 m high bump, we compare the rupture behaviors across various friction laws. Figure 2. 9 shows the details of a dynamic rupture governed by the RS-A law on a nonplanar fault with a 300 m high bump. After being nucleated at the hypocenter at 15 km along dip, the dip-slip rupture propagates in all directions on the fault. The rupture fronts propagating in the dip directions are the mode II edges with relatively large rupture speeds, while the rupture fronts travelling in the strike directions are mode III edges with relatively slower rupture speeds, resulting in an elliptical shape for the entire ruptured area before the rupture hits the bump. At 3 s, the updip propagating rupture front enters the downdip slope of the bump, and is slightly decelerated due to the local high strength induced by the bump geometry. From 3 s to 4 s, this updip propagating

part of the rupture passes through the high strength area and arrives at the center of the bump. The slip rate at the updip rupture front has been accelerated after the rupture passes through the high strength area, because the static stress drop in this area is relatively higher than the background value and releases more energy for further rupture propagation. From 4 s to 5.5 s, the updip propagating rupture edge passes through the updip slope of the bump. Since this part of the bump has low normal stress levels and hence low yield strengths, the rupture that once slows down at the deeper part of the bump accelerates in this area with less impedance. Afterwards, this dynamic rupture continues to spread out on the rest of the fault surface until it reaches the preset velocity strengthening zone along the fault edges, as demonstrated by the corresponding rupture time contour. In this model, the rupture propagation is influenced by the bump only when it is traveling on the bump area, and the overall effect of this 300 m high bump on rupture propagation is minor. The other three friction laws show similar rupture behavior on a fault plane with a 300 m high bump.

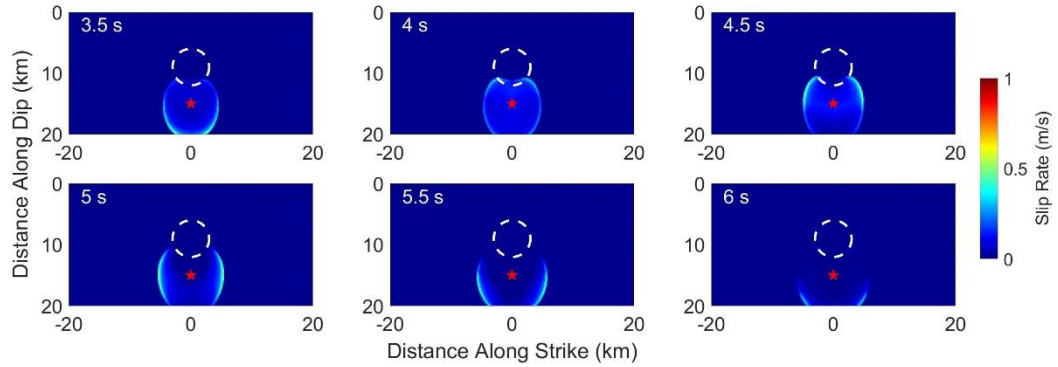


Figure 2. 10 Snapshots of the spatial slip rate distribution for the dynamic rupture simulation with governed by the SW law on a nonplanar fault with a 600 m high bump.

When the height of the bump increases to 600 m, more differences among the friction laws appear. Figure 2. 10 illustrates the evolution of the spatial slip velocity distribution over the fault for the SW case. At 2.5 s, the updip rupture front encounters the perimeter of the bump and is forced to slow down. The slip rate at the updip rupture front drops to 0.1 m/s, while the rest of the rupture front remains unaffected with a slip rate of 0.7 to 0.9 m/s at the front tip. From 2.5 s to 3.5 s, as rupture area continues to expand, the slow-down effect on the rupture front caused by the bump gradually spreads out from the updip front to the lateral fronts. At 4 s, the slip rate near the updip rupture front is temporarily increased by ~ 0.2 m/s due to the arrival of reflected seismic wave from the free surface. From 4.5 s to 5.5 s, this increase of slip rate migrates from the updip front toward the downdip front, while slip rate within the rupture area decreases. Finally, slip rate diminishes after 6 s on the entire fault. In this simulation, the dynamic rupture is

arrested before it can propagate to the fault edges because of the barrier effect of the bump located updip of the hypocenter.

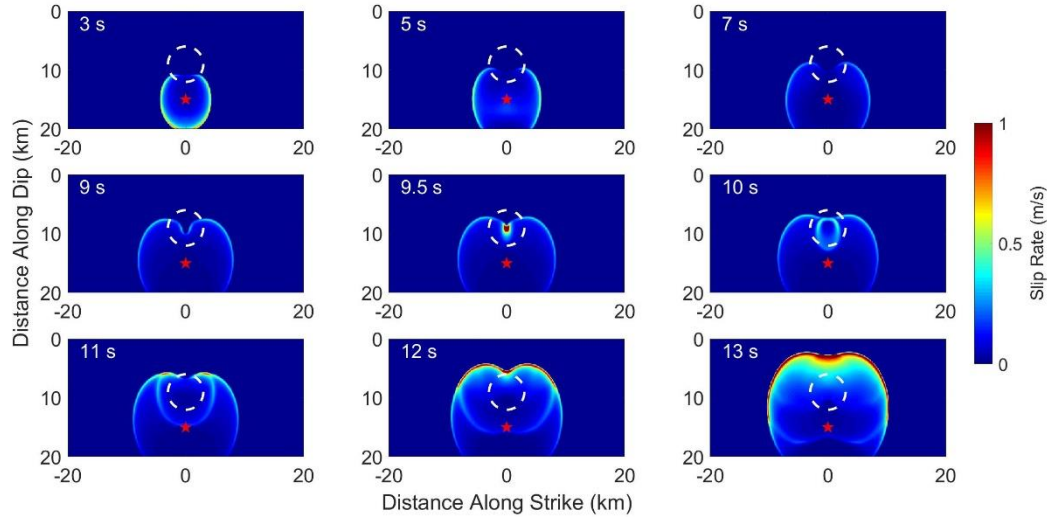


Figure 2. 11 Snapshots of the slip rate spatial distribution for the dynamic rupture simulation governed by the RS-A law on a nonplanar fault with a 600 m high bump.

As shown before, the RSF laws provide a lower yield strength on the compressional side of the bump than the SW law and thus are easier for rupture to overcome. Figure 2. 11 shows how the dynamic rupture governed by the RS-A law can pass through the 600 m high bump. After nucleation, the rupture expands and enters the compressive side of the bump at 3 s. From 5 s to 9 s, the rupture front is obviously halted by the high strength area on the compressive side, being split into two parts that encircles

the bump as the rest of the rupture continues to propagate. At 9.5 s, the split rupture fronts collide together at the top of the bump. The shear stress at the split rupture fronts concentrates at a small region and generate sufficient energy to fully break the highest strength on the bump, forming a slip velocity pulse. This is a phenomenon called rupture front focusing (*Fukuyama and Madariaga, 2000*), where two separate rupture fronts join together at one location and cause rapid stress reduction. This slip velocity pulse spreads out from the bump at 10 s and joins the primary rupture front later, forming a strong rupture that travels updip toward the free surface and laterally toward the fault edges (11 to 13 s). This event finally ruptures the whole fault area. *Dunham et al. [2003]* investigated this mechanism for a flat rupture front and proposed that it could be a possible mechanism for supershear transition. Although we observe similar mechanism in this RS-A case, the elliptical rupture is less energetic than a flat rupture front and does not grow into a supershear rupture.

In Figure 2. 12, both the results of simulations using the RS-S and RS-FH laws for a 600 m high bump are shown. Only the moments of the rupture passing the bump are illustrated. It appears that the ruptures governed by the RS-S and RS-FH laws behave similarly, and both of them are relatively stronger than those governed by the SW and RS-A laws. At 5.5 s, the updip rupture front is split by the compressive side of the bump. The split ruptures bypass the bump and merge at the top of the bump in the same way as those in the RS-A case do. Rupture front focusing excites a strong slip velocity pulse, but this pulse seems to make little difference to the overall rupture behavior when it catches up with the major rupture.

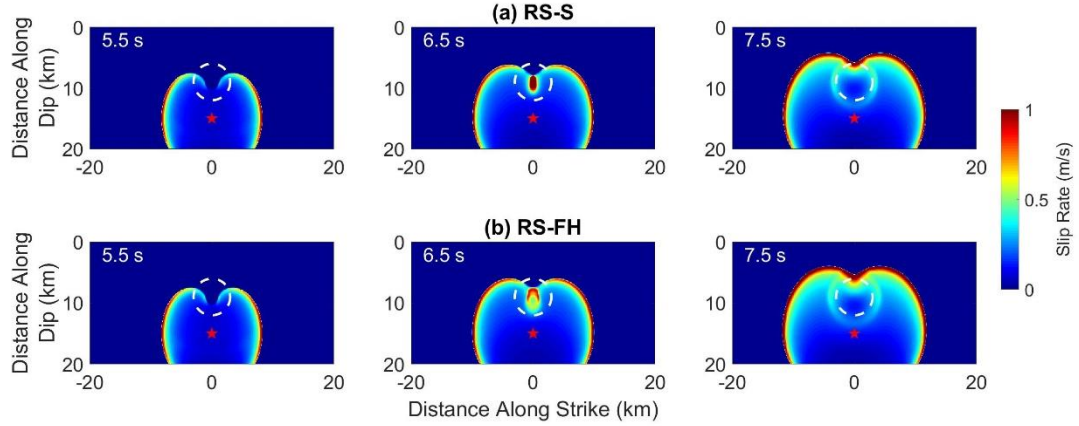


Figure 2. 12 Snapshots of the slip rate spatial distribution for the dynamic rupture simulation governed by the RS-S law (upper panel) and RS-FH law (lower panel) on a nonplanar fault with a 600 m high bump.

Examination of slip velocity snapshots of all experiments shows that there are three types of rupture patterns that would occur on a three-dimensional nonplanar fault with a bump geometry. The first one is that the rupture directly passes through the bump with minor impedance of the high strength area, causing slightly longer rupture duration than on a planar fault. The second type is that the rupture front directly striking the bump is significantly obstructed and splits into two parts, but the split rupture fronts manage to circumvent the high strength area and finally break the bump. This type of rupture has a much longer rupture duration than the first one. The third type is that the rupture is completely stopped by the bump, which limits the ruptured area and the average slip, and hence the seismic moment magnitude. The barrier effect of the bump on dynamic ruptures progressively increases from the first type to the third type. Here we label these three types

of rupture patterns as type A, B, and C, respectively, and compile the simulation results of all nonplanar fault experiments according to the three rupture types in Table 2. 2.

Table 2. 2 Rupture Type Classification

Height (m)	SW	RS-A	RS-S	RS-FH
300	A	A	A	A
600	C	B	B	B
900	C	C	B	B

Generally speaking, as the height of the bump increases, the difficulty for a dynamic rupture to overcome the bump also increases. Comparison of rupture types among the different friction laws suggests that friction laws play an important role in determining how a bump on the fault plane could affect dynamic rupture propagation. As demonstrated before, the SW law provides a higher strength on the compressional side of the bump than the RSF laws, so when the bump is 600 m high, the SW rupture can be completely stopped, while the ruptures governed by the other three RSF laws are temporally stalled but can break the bump, reaching the whole fault in the end. When the bump is 900 m high, both SW and RS-A laws are unable to sustain spontaneous ruptures

to encircle the bump, but the RS-S and RS-FH laws can still produce type B ruptures. This is because compared to the linearly weakening group, the exponentially decaying group generates dynamic ruptures with faster rupture speed and higher slip rate at rupture front, i.e., more kinetic energy to promote rupture propagation around the high strength barrier on the 900 m high bump until rupture front focusing occurs on the other side of the bump.

Figure 2. 13 shows the time evolution of slip rate and shear stress at the on-fault station located at the center of the bump (9 km downdip distance). It compares the results of all friction laws between the planar fault models and the nonplanar fault models with a 600 m high bump. In the planar fault models, the results of the linearly weakening group are close to each other, and the results of the exponentially decaying group are also close to each other. By comparing the arrival time of peak slip rates and peak shear stresses, the ruptures controlled by the RS-S and RS-FH laws arrives 0.5 s earlier at this location than those controlled by the RS-A and SW laws. The peak slip rates in the RS-S and RS-FH simulations are slightly higher than those in the other group.

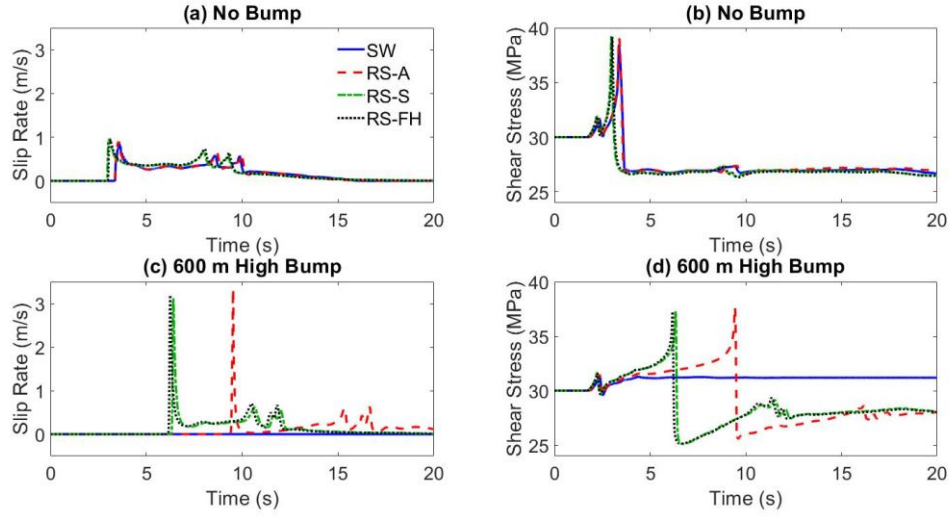


Figure 2.13 Comparison of slip rate and shear stress evolution at the location of the bump center between a planar fault (a and b) and a nonplanar fault with 600 m high bump (c and d).

In the nonplanar fault models, the arrival of the rupture at this location is delayed by the compressional side of the bump to some extent for all friction laws. In the SW simulation, the rupture is completely stopped before it reaches the center of the bump, resulting in no variation in slip rate history and minor increase in shear stress. For the RS-A simulation, the arrival of peak slip rate is delayed by 6 s compared to the result in the planar fault model. For RS-S and RS-FH simulations, the results stay close to each other and the rupture controlled by these two laws are both delayed 3 s by the bump. In addition to the delay effect, the level of the peak slip rates of all RSF laws rise to about 3 m/s in the nonplanar fault models, three times higher than those in the planar fault models. This

is the consequence of rupture front focusing, because the split rupture fronts converge at the top of the bump in all RSF cases and cause rapid stress drop and large slip velocity.

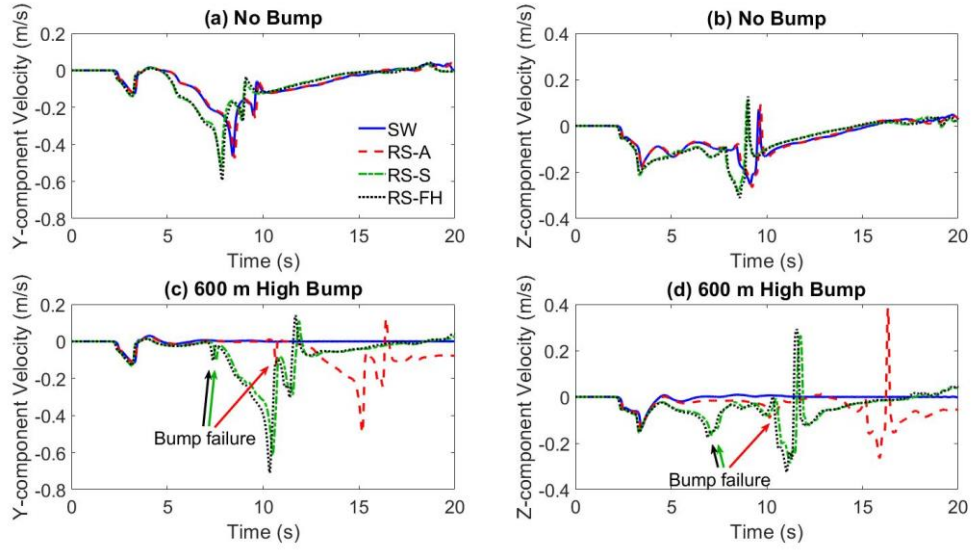


Figure 2. 14 Comparison of particle velocity at a free surface location above the bump center between a planar fault (a and b) and a nonplanar fault with 600 m high bump (c and d). Both y-component and z-component velocities are shown. The x-component velocity is trivial due to symmetry of the model and not shown. A signal related to bump failure in each nonplanar fault model that has a bump failure is pointed out by an arrow with a corresponding line style.

We also examine how different the ground motions above the center of the bump may be in the simulations with the different friction laws. Figure 2. 14 shows the particle velocity in the y- and z-directions of all the friction laws in the planar fault models and the nonplanar fault models with a 600 m high bump. The component in x-axis is trivial due to

model symmetry. In a planar fault model, there are two key signals observed in the ground motion, including a small pulse at around 3 s corresponding to the artificial nucleation at the hypocenter, and a large pulse at around 8 to 10 s related to the breakage of the free surface by the ruptures. Again, the signals of the exponential decaying group arrive earlier than the linearly weakening group because the former group generates ruptures that travel slightly faster.

In a nonplanar fault, the breakage signals in the SW case vanishes, since the rupture in this case is stopped by the bump and does not reach the free surface. In other cases, the breakage signals are delayed by as much amount of time as in rupture delay, simply because the rupture is kept from reaching the free surface until a later time. Before the arrival of the breakage signal, a new signal is observed, which is associated with the slip velocity pulse when the bump fails. This slip velocity pulse, which is generated by rupture focusing and is several times larger than the average slip velocity at the rupture front, shakes the free surface more intensely and results in a larger amplitude of the breakage signal in the nonplanar models than in the planar models.

2.7 Discussion

Oceanic relief subduction is commonly observed in worldwide subduction zones. In this study, we assume that the nonplanar fault geometry causes prestress heterogeneity, and our three-dimensional models provide possible scenarios for dynamic ruptures on thrust faults with large-scale topographic reliefs in a pure thrust fault environment. At the

bump area, the curved fault surface results in both normal and shear stress variations compared to the background pure thrust fault stress state, forming a compressional area with greater compressive normal stress on the landward leading flank (the downdip slope) and an extensional area with less compressive normal stress on the seaward trailing flank (the updip slope). This heterogeneous prestress pattern is consistent with a numerical study of overriding plate deformation caused by subducted seamounts (*Ding and Lin, 2016*). Since frictional yield strength generally increases with normal stress, the compressional area on the landward side of the bump becomes unfavorable for the rupture propagation. This condition is analogous to those observed in numerical studies of a bending geometry (*Duan and Oglesby, 2005b; Kase and Day, 2006; Bhat et al., 2007*), as pointed out by *Yang et al. (2013)*. In this sense, the height-to-basal-width ratio of a bump is equivalent to the angle of a restraining bend, determining how unfavorable the compressional side of the bump can be when a rupture strikes on it.

However, our results show that in a three-dimensional fault model, earthquake rupture may be able to overcome a bump and continue to spread out on the fault surface, even though the frictional strength on the bump may be high enough to resist rupture propagation in a two-dimensional model. Previous studies on locally strong patches on a fault surface have revealed that rupture front that is resisted by a high strength patch of finite size from one side can be split into two parts, circumvent the patch, and join back together at the opposite side of the patch (*Das and Kostrov, 1983; Fukuyama and Madariaga, 2000; Dunham et al., 2003*). The rupture front focusing, i.e., the convergence of split rupture front, concentrates the stress at the rupture front and excites a burst of slip

velocity pulse (*Fukuyama and Madariaga, 2000*) that radiates high frequency seismic waves. *Page et al. (2005)* investigated the near-source ground motion related to barriers and they found that a barrier initially resists rupture and arrests ground motion, but later when it is surrounded by rupture and the rupture front concentrates, it leads to a more violent pulse at the surface. Such rupture behavior related to a stress barrier on a planar fault model is also observed in our nonplanar fault models above, since the bump geometry induces a similar highly stressed area on its compressional side. In addition, this rupture behavior is not only observed in the RSF simulations but also seen in additional SW simulations with a bump of 450 m height that allows rupture to pass through (not shown), indicating that such behavior is common for different friction laws. However, while supershear rupture transition is observed in some stress barrier models of a planar fault in previous studies *Dunham et al. (2003)*, we do not observe any supershear phenomenon after the occurrence of rupture front focusing in our nonplanar fault models.

Therefore, for a geometrical irregularity of finite size to fully confine a dynamic rupture, it needs to be not only strong enough to resist the striking rupture front, but also large enough in size to prevent split ruptures from bypassing the irregularity to focus and concentrate sufficient energy to overcome the barrier. In fact, this latter behavior, also labeled as type B behavior in our results, is a phenomenon unique in three-dimensional models and cannot be observed in two-dimensional simulations. The dimension of the irregularity in the direction perpendicular to the rupture propagation direction may be crucial in determining whether a rupture that is resisted can bypass the area unfavorable for propagation and continue to expand. The transition between a full rupture over the

fault and a partial rupture blocked by a barrier observed in two-dimensional models corresponds to the transition between type A and type B behaviors in our results, and the actual transition between a full and a partial rupture in three-dimensional models is the transition between type B and type C behaviors in our results.

When considering dynamic rupture in the thrust fault setting, it would be desirable to examine particular features related to such thrust fault geometry, such as the reflected seismic waves from the free surface. As shown in Figure 2. 15, there are two reflected waves arriving at the fault, one at 4 s and the other at 6 s, in the planar fault cases governed by either SW or RS-A law. These waves last for about 1 s and temporarily enhanced the slip rate up to 0.3 m/s in the ruptured area where local slip rate has dropped to ~ 0.1 m/s before the arrival of the reflected waves. These features on a planar thrust fault for SW law is similar to those for a RS-A law, due to our choice of frictional parameters that keep the yield strength, dynamic stresses and fracture energy nearly identical between these two laws. In the nonplanar fault cases, the existence of the bump updip of the nucleation zone blocks further propagation of the rupture. The reflected wave arrives at the fault surface at about 5 s for both SW and RS-A cases. It appears that such perturbation does not assist the rupture to pass through the bump. As presented before, the rupture in the SW case is a type C rupture being stopped by the bump, and the rupture in the RS-A case is a type B rupture that manage to bypass the bump and continue its propagation at the far side of the bump.

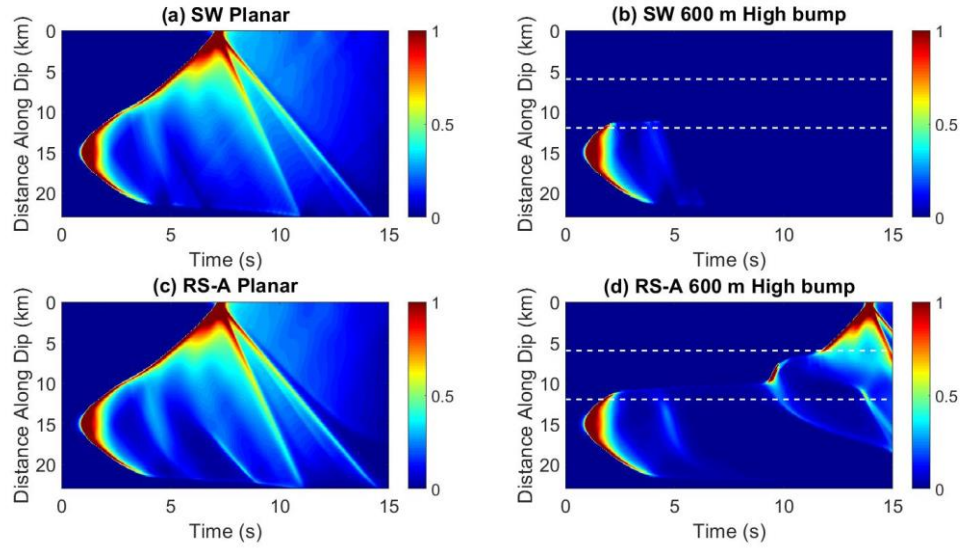


Figure 2. 15 Space-time plots of slip rate along the line in dip direction through the center of the bump. (a) and (b) are SW cases with no bump and a bump of 600 m high, respectively. (c) and (d) are RS-A cases with no bump and a bump of 600 m high, respectively. Slip rate is in m/s. Dashed lines in (b) and (d) denote the updip and downdip boundary of the bump. The along-dip profile is extended to 23 km to include the strengthening fault edge (20 to 23 km) to show the termination of the rupture.

In our numerical experiments, the downdip rupture front is terminated by the bottom edge of the fault with negative stress drop (for SW law) or velocity-strengthening (for RSF laws) setting in accord with the nature that the earthquakes only occur within the seismogenic. The rupture stops at these fault edges and emits stopping phases which reduce slip rate within the ruptured area and finally arrest fault slip (*Madariaga, 1976; Fukuyama and Madariaga, 1998*). In Figure 2. 15, the space-time plots of slip rate evolution show that the downgoing rupture front vanishes at 21 km along dip at 4.1 s. It radiates a stopping signal that propagates updip and reduce the slip rate along its path. Its

stopping effect is more obvious by looking at the location from 15 km to 18 km along dip direction at 5 s where slip rate is enhanced by the first reflected wave but then reduced by the stopping phase. However, as shown in the slip rate snapshots from 4.5 s to 6 s for the SW case in Figure 2. 10, the rupture front starts disappearing from the updip side instead of the downdip side, suggesting that compared to the stopping phase emitted from the bottom edge, the one emitted from the bump is more dominant in arresting the rupture.

Our model assumes that rupture nucleation occurs in the vicinity of the seamount, which leads to the fact that the dynamic rupture interacts with the bump earlier in time than reflected waves and bottom edge stopping phases. As shown by *Yang et al.* (2013), long seamount-to-nucleation distance allow the rupture front to grow into its full speed and thus become easy to pass the barrier. Besides, the seismogenic width which limits the depth extent of the rupture, can also modulate the rupture behavior by radiating stopping phase (*Weng and Yang, 2017*). We did not explore these factors in this study, but these factors in a thrust fault model can affect the rupture speed before the rupture hits the seamount. Since rupture propagation before reaching the seamount is on planar part of the fault, these factors should modulate the rupture speed in the same way for various friction laws with their frictional parameters finely tuned in our planar fault simulations. Therefore, one can expect that under identical geometrical configuration, the friction laws discussed here can produce rupture fronts with similar rupture speed (i.e., similar capability to overcome a barrier) before they hit the seamount.

It is noteworthy that the frictional constitutive laws adopted here attempt to represent the friction failure process in the cohesive zone from a macroscopic point of

view. Although from the SW law to the RSF laws, more and more physical details of the friction process observed in laboratory experiments are included, the most prominent feature to reproduce dynamic rupture growth is still the weakening process of frictional resistance, which is the basic property embodied in all the friction laws used here. In essence, when rupture propagates, it is the subtle balance between the released strain energy and the absorbed fracture energy in the cohesive zone that determines the rupture velocity. A high strength patch on the fault consumes more fracture energy than average and thus slows down rupture propagation. As mentioned above, the SW law provides a higher strength than the RSF laws on the high normal stress area of a bump, which means it consumes more fracture energy when rupture arrives and tends to significantly slow down or even block the rupture. Among the three RSF laws, the RS-S and RS-FH laws, which shows an exponentially decaying stress-slip relation, release strain energy faster in the cohesive zone than the RS-A law does. Therefore, even though we keep equal fracture energy for all friction laws, these two laws produce faster-moving dynamic ruptures that can continue propagating after being split by a bump, while this bump may block the rupture in the RS-A case. In our simulations, there is little difference in rupture behaviors between the RS-S law and the RS-FH law. However, given certain initial conditions, the RS-FH law with strong rate weakening property can generate pulse-like rupture which may be less energetic than those crack-like ruptures generated by other friction laws under similar initial conditions and thus less likely to overcome a bump barrier.

The difference in rupture phenomena between various friction laws for a given seamount geometry may lead to more sophisticated difference in subsequent events. A

rupture stopped by a bump (type C rupture) can lead to increased shear stress on the bump and thus make the next rupture easier to overcome the bump [*Duan and Oglesby, 2005; Yang et al., 2012; Yang et al., 2013*]. The bump barrier would finally break after stopping several ruptures and then a massive event occurs. On the contrary, a rupture able to overcome the bump (type A or type B) leaves the bump a ruptured area that is likely to be ruptured again in subsequent events. Therefore, if different friction laws result in different types of rupture behavior for a given bump geometry, their subsequent earthquake recurrence patterns may also differ significantly. Of course, realistic situations for earthquake cycle are far more complex. For example, *Lapusta and Liu (2009)* show that in long-term earthquake cycle simulations, normal stress heterogeneity could have significant impact on the first event but such effect would disappear in subsequent events due to stress redistribution. Unlike such long-term simulations for earthquake cycles, our numerical models in this study consider a single dynamic event for a subduction fault with a subducted seamount and assumes a simple pure-thrust initial stress state. Nevertheless, the comparison of various friction laws with the same initial stress state in this study provides useful insights into how different friction laws affect rupture dynamics on nonplanar thrust faults.

2.8 Conclusions

In this study, we compare the effect of large-scale seamount-like geometrical irregularity on earthquake rupture along a thrust fault interface governed by various

friction laws. Assuming a regional stress condition, the nonplanar fault geometry introduce heterogeneous initial stress distribution, which leads to significant difference between the local yield strengths determined by the SW law and the RSF laws. The seamount geometry in our thrust fault model gives a higher strength in the SW law than in the RSF laws, resulting in stronger barrier effect of the seamount on incoming ruptures governed by the SW law than the RSF laws. Due to the difference in the stress weakening process, the rupture governed by the linearly weakening group appears to be less energetic and easier to be affected by the bump than the one governed by the exponentially weakening group.

There are three types of rupture patterns identified on a three-dimensional nonplanar fault based on the relation between the strength of the incoming rupture front and the strength level of the compressional area on the bump. The first one is that the rupture directly passes through the bump with minor impedance of the high strength area. The second one is that the rupture that directly strikes the high strength area is obstructed and splits into two, which continue to propagate around the high strength area and collide at the other side, breaking the barrier and exciting slip velocity pulse. The third one is that the rupture front splits but the split parts are unable to continue propagating and merge together, resulting in a full stop in front of the bump, limiting the size of the earthquake magnitude. The observation of the second type of rupture is limited to three-dimensional models. The specific form of friction laws plays an important role in varying the intensity of the rupture as well as the strength of the geometrical barrier to determine which type of rupture behavior should appear under a given prestress condition.

CHAPTER III

DYNAMIC FINITE ELEMENT MODELING OF EARTHQUAKE CYCLES ON FAULTS WITH RATE- AND STATE-DEPENDENT FRICTION

3.1 Introduction

Destructive earthquakes occur repetitively on large-scale fault systems between tectonic plates. The nature of earthquake recurrence on fault systems involves a spectrum of faulting processes from dynamic rupture during earthquakes to stable creep between earthquakes. Although the classic elastic rebound theory offers a first-order explanation of generation and repetition of earthquakes on slowly loading faults, more details have been revealed by experiments and observations in the past decades. For example, application of the laboratory-derived rate- and state-dependent friction law (RSF) (*Dieterich, 1979; Ruina, 1983*) in exploring earthquake instability leads to the recognition and analysis of the nucleation process before seismic events (*Dieterich, 1992; Rubin and Ampuero, 2005; Ampuero and Rubin, 2008*). Geodetic observations indicate that large earthquake rupture gives rise to large postseismic deformation that differs from interseismic process (e.g. *Savage and Svarc, 1997; Jacobs et al., 2002; Ozawa et al., 2004; Ozawa et al., 2011*).

Generally speaking, a full earthquake cycle consists of four phases: interseismic, nucleation, coseismic and postseismic. The coseismic phase is commonly characterized as a dynamic process associated with transient continuum mechanics and frictional failure,

while the interseismic, nucleation and postseismic periods are usually assumed quasi-static processes under the effect of slow tectonic loading. These faulting behaviors involve complex physical processes of a wide range of scales in both space and time, and present great computational challenges for the full cycle simulation that attempts to capture as many physical details as possible. Ideal numerical models need to capture both rapid coseismic sliding which lasts for tens of seconds and slow tectonic loading during the interseismic period of hundreds of years. They also need to handle a fault surface of hundreds of kilometers for tectonic plate boundaries, but with a grid size small enough to resolve the cohesive zone on the order of kilometers when dynamic rupture propagates.

In many cases, studies of dynamic earthquake ruptures have been focusing on the rapid slip process in a narrow time window and approximate the interseismic loading for simplicity (e.g., *Harris et al.*, 2018). On the other hand, studies of earthquake cycle behaviors typically focus on quasi-static processes of earthquake cycles, significantly simplifying (or even ignoring) the coseismic dynamic process (e.g., *Rice*, 1993). However, quasi-static and dynamic processes of earthquake cycles are not independent of each other but coupled together over time and space. For example, the initial stress condition before an earthquake, which is a critical quantity in dynamic rupture modeling, can be very heterogeneous near fault geometrical complexities such as bends, stepovers, and junctions [Duan and Oglesby, 2005, 2006, 2007] due to previous earthquake cycles. Therefore, it is desirable in the earthquake-science community to simulate both dynamic and quasi-static processes of earthquake cycles on realistically complex faults.

Existing earthquake simulators that attempt to describe earthquake sequences generally simplify the complexity of physical processes to make computations tractable. Most earthquake simulators in the community make significant approximations to the elastodynamics during earthquakes to improve computational efficiency, in order to produce long earthquake histories on complex fault systems to gain basic insights of seismicity characteristics from a statistical perspective (e.g. *Dieterich and Richards-Dinger*, 2010; *Pollitz*, 2012; *Sachs et al.*, 2012; *Tullis et al.*, 2012; *Ward*, 2012). Among these simulators is RSQSim developed by *Dieterich and Richards-Dinger* (2010) based on a boundary element formulation and a simplified form of rate-and-state friction laws. The simulator can capture fault interactions and seismicity characteristics over long time history on complex fault systems, but it does not include spontaneous rupture propagation for the co-seismic phase. Instead, it approximates the co-seismic phase as quasi-dynamic rupture propagation (*Rice*, 1993). Similar simulators with quasi-dynamic approximation but based on various numerical methods are also used in the community for investigation of specific effects of fault geometry and material properties on earthquake sequences (e.g. *Yang et al.*, 2012; *Erickson and Dunham*, 2014). Nevertheless, none of these models consider fully dynamic effects in single seismic events, which could have complex interactions with interseismic deformation as shown in previous studies (e.g. *Duan and Oglesby*, 2005a; *Duan and Oglesby*, 2005b; *Chen and Lapusta*, 2009; *Kaneko et al.*, 2011). One notable exception in the community to the quasi-dynamic earthquake simulators discussed above is the simulator developed by Lapusta and co-workers (*Lapusta et al.*, 2000; *Lapusta and Liu*, 2009) using a boundary integral method. This

simulator employs a unified framework that resolves both seismic and aseismic processes of an earthquake cycle, as well as the gradual transitions between these processes. Fully dynamic earthquake simulators including more complex physical features of earthquake sources are built upon this method, such as a unified friction-to-flow law (*Shimamoto and Noda, 2014*), thermal pressurization (*Noda and Lapusta, 2010*), and dynamic weakening (*Noda and Lapusta, 2013*). However, studies using this method are restricted to planar, vertical fault geometry in a linear elastic space, while natural faults generally involve complex crustal structures such as nonplanar fault geometry and heterogeneous material properties. Other fully dynamic simulators, such as *Kaneko et al. (2011)* and *Aagaard et al. (2013)*, resolve earthquake cycle by coupling individual dynamic and quasi-static methods that are capable of explicitly characterizing the rock mass in which the complex fault system is embedded.

With the objective to studying earthquake behaviors on geometrically complex faults in realistically complex geologic media, we develop a new dynamic earthquake simulator based on a dynamic finite element method EQdyna (*Duan and Oglesby, 2006; Duan and Day, 2008; Duan, 2010; Duan, 2012*) and a dynamic relaxation technique in this study. This newly developed earthquake simulator reproduces long-term histories of seismic and aseismic fault slip with a set of desirable features, including stable sliding during the interseismic phase, smooth but rapid growth of slip velocity during the nucleation phase, spontaneous rupture propagation during the coseismic phase, and gradual decay of slip velocity during the post-seismic phase. We test this earthquake simulator on a vertical strike-slip fault by comparing with results in a previous study

(*Lapusta and Liu, 2009*). Then we apply it to thrust faults, which is the first step to explore earthquake cycle behaviors on geometrically complex faults.

3.2 A New Dynamic Earthquake Simulator Based on Finite Element Method

In this section, we present the new dynamic earthquake simulator. This simulator is based on the three-dimensional explicit finite element method (FEM) algorithm EQdyna (*Duan and Oglesby, 2006; Duan and Day, 2008*). The dynamic finite element code EQdyna has been verified in the community-wide effort for dynamic rupture simulations (*Harris et al., 2009; Harris et al., 2011; Harris et al., 2018*), and has been used for studies of spontaneous rupture on various types of complex fault geometry (*Duan and Oglesby, 2005a; Duan and Oglesby, 2005b; Duan and Oglesby, 2006; Duan and Oglesby, 2007; Duan, 2010; Duan, 2012*). We use an adaptive dynamic relaxation technique to allow EQdyna to simulate the quasi-static processes of an earthquake cycle with a variable time stepping scheme, which is suitable for long-term fault slip histories governed by a rate- and state-dependent friction law. The integrated algorithm based on EQdyna and the dynamic relaxation technique enables us to capture faulting behaviors in both the dynamic rupture process and the quasi-static processes of earthquake cycles on realistically complex faults.

3.2.1 Dynamic Modeling with Rate- and State-Dependent Friction

The finite element method discretizes the space domain with hexahedral elements and transforms the governing elastodynamic equations into the semidiscrete matrix equation

$$\mathbf{M}\mathbf{a} + \mathbf{K}\mathbf{u} = \mathbf{F}, \quad (3.1)$$

where \mathbf{a} and \mathbf{u} are the particle acceleration and displacement vectors, respectively. \mathbf{M} is the mass matrix, \mathbf{K} is the stiffness matrix, and \mathbf{F} is the vector of applied forces. We employ an one-point quadrature integration rule for hexahedral elements, which shows great efficiency in computation but also introduces a negative effect called hourglass modes that lead to hourglass instability in dynamic codes. In EQdyna, these modes are resisted by adding an anti-hourglass forces \mathbf{H} to the right hand side of equation (3.1) (*Kosloff and Frazier, 1978; Duan and Oglesby, 2006*). EQdyna integrates equation (3.1) using the central difference time integration method, which leads to the following explicit updating scheme when the mass matrix is diagonal (*Duan and Oglesby, 2006*),

$$\mathbf{a}_t = \mathbf{M}^{-1}(\mathbf{F}_t - \mathbf{K}\mathbf{u}_t), \quad (3.2)$$

$$\mathbf{v}_{t+\Delta t/2} = \mathbf{v}_{t-\Delta t/2} + \mathbf{a}_t\Delta t, \quad (3.3)$$

$$\mathbf{u}_{t+\Delta t} = \mathbf{u}_t + \mathbf{v}_{t+\Delta t/2}\Delta t, \quad (3.4)$$

where \mathbf{v} is the particle velocity vector defined at half time step and subscript t denotes time. In order to keep the numerical simulation stable, such an explicit scheme requires

the length of time step Δt to be restricted by the Courant-Friedrich-Lewy (CFL) condition (e.g., *Duan and Day*, 2008)

$$\Delta t = \alpha_{CFL} \frac{\Delta x_{min}}{v_P}, \quad (3.5)$$

where Δx_{min} is the minimum element edge length in the model, α_{CFL} is the Courant number smaller than 1 and v_P is the P-wave velocity.

Various constitutive friction laws have been successfully implemented in the code EQdyna for dynamic rupture modeling (*Luo and Duan*, 2018), including the slip-weakening law, the RSF law with aging law, the RSF law with slip law, and the RSF law with slip law and strong rate-weakening. Among these friction laws, the RSF law with aging law is commonly used to reproduce the major features of earthquake cycles (e.g., *Lapusta et al.*, 2000; *Lapusta and Liu*, 2009; *Erickson and Dunham*, 2014; *Yu et al.*, 2018). The RSF law defines the frictional strength τ as a function of effective normal stress σ , slip rate V and state variable θ :

$$\tau = \sigma \left(f_0 + a \ln \frac{V}{V_0} + b \ln \frac{V_0 \theta}{L} \right). \quad (3.6)$$

The parameters a and b correspond to the rate-dependency and the state-dependency of the frictional strength, respectively. L is the characteristic slip distance. f_0 is a reference friction coefficient associated with a reference steady state slip rate V_0 . The state variable θ evolves according to the aging law

$$\frac{d\theta}{dt} = 1 - \frac{V\theta}{L}. \quad (3.7)$$

In dynamic rupture simulations, the elastodynamic equations coupled with the RSF law lead to a set of stiff partial differential equations that cannot achieve numerical stability with an explicit time stepping scheme (*Rojas et al.*, 2009). Therefore, in addition to using the central difference time scheme for FEM in the whole domain, we implement the trapezoidal scheme as a special treatment for friction evolution on the fault boundary. The friction strength τ at time t is defined as the average of $\tau(\sigma_t, V_{t-\Delta t/2}, \theta_t)$ and $\tau(\sigma_t, V_{t+\Delta t/2}, \theta_t)$, which are evaluated through Equation (3.6) using the velocity at half time step before and after time t , respectively. Then τ_t is converted to shear stress and added to \mathbf{F}_t in equation (3.2). Now $V_{t+\Delta t/2}$ appears in both (3.2) and (3.3), and we use the Newton-Raphson method to solve these equations simultaneously for $V_{t+\Delta t/2}$. Note that this treatment is for the nodes on the fault boundary only but can be applied independently along with the regular central difference updating scheme in the model volume.

During dynamic rupture propagation, the shear stress rises and falls rapidly in the cohesive zone of the rupture front, which requires a certain number of elements to resolve these features and thus imposes a spatial resolution criterion on the element size Δx on the fault (*Palmer and Rice*, 1973; *Day et al.*, 2005). The cohesive zone size Λ_0 at rupture speed $v_R = 0^+$ under the RSF law we use here is given as

$$\Lambda_0 = c_1 \frac{\mu^* L}{b\sigma}, \quad (3.8)$$

where C_1 is a constant and μ^* is μ for mode III or $\mu/(1 - \nu)$ for mode II, with μ the shear modulus and ν the Poisson's ratio (Lapusta and Liu, 2009). For finite element or finite difference methods, it is found that 3 to 5 elements within Λ_0 is good enough to resolve the dynamic rupture (Day et al., 2005).

The outer boundaries of the model domain use perfectly matched layers (PML) to absorb seismic waves (Liu and Duan, 2018), which prevent seismic waves from reflecting from the truncated model boundaries .

3.2.2 Static Modeling Using Adaptive Dynamic Relaxation Method

The dynamic relaxation (DR) method is a widely used numerical technique for static analyses of nonlinear structural systems (e.g., Qiang, 1988; Oakley and Knight, 1995; Kilic and Madenci, 2010; Ali et al., 2017). It stems from the fact that the steady-state part of the dynamic solution represents the static solution. Therefore, solving for the static solution to an elastostatic problem of a system can be transformed to reaching the long-term limit of a damped dynamic process, which is a solution to an elastodynamic problem of the same system. Previous studies (e.g. Duan and Oglesby, 2005b) show that dynamic codes can be used to simulate quasi-static processes during the interseismic phase on slip-weakening dipping fault systems using DR. In practice, DR introduces a viscous damping term with a mass damping factor α to the semidiscrete FEM matrix form (3.1) of the elastodynamic equation so that it becomes

$$\mathbf{M}\mathbf{a} + \alpha\mathbf{M}\mathbf{v} + \mathbf{K}\mathbf{u} = \mathbf{F}, \quad (3.9)$$

where $\alpha\mathbf{M}\mathbf{v}$ is the viscous damping term. When the acceleration and velocity fields are damped to zero, the final displacement solution \mathbf{u}^* satisfies the equation $\mathbf{K}\mathbf{u}^* = \mathbf{F}$ and thus becomes a solution to the elastostatic problem. The dynamic relaxation technique is referred to as a pseudo-dynamic method in which the system evolves dynamically from an unbalanced state to its final equilibrium state where the final static solution \mathbf{u}^* is obtained. Since the artificial dynamic process is undesired, the mass matrix \mathbf{M} and the damping factor α are fictitious and do not represent the physical system. They can be designed to optimize the convergence performance of the system, in other words, to allow the system to decay to its equilibrium state with the least number of time steps. Stability analyses provide a theoretical means to find out the setting for the best decaying rate of the damping process. Using the central difference time integration scheme to integrate equation (3.9), one can obtain the updating equation with respect to the displacement vector

$$\mathbf{u}_{t+\Delta t} = [(1 + \beta)\mathbf{I} - \gamma\mathbf{M}^{-1}\mathbf{K}]\mathbf{u}_t - \beta\mathbf{u}_{t-\Delta t} + \gamma\mathbf{M}^{-1}\mathbf{F}, \quad (3.10)$$

where $\beta = \frac{2-\alpha\Delta t}{2+\alpha\Delta t}$, $\gamma = \frac{2\Delta t^2}{2+\alpha\Delta t}$, and \mathbf{I} denotes the identity matrix. In order to evaluate the convergence characteristics, one can define the error vector $\mathbf{e}_t = \mathbf{u}_t - \mathbf{u}^*$ and transform equation (3.10) into an error equation

$$\mathbf{e}_{t+\Delta t} = [(1 + \beta)\mathbf{I} - \gamma\mathbf{M}^{-1}\mathbf{K}]\mathbf{e}_t - \beta\mathbf{e}_{t-\Delta t}. \quad (3.11)$$

Note that $\mathbf{M}^{-1}\mathbf{K}\mathbf{u}^* = \mathbf{M}^{-1}\mathbf{F}$. To analyze the relationship between successive error vectors given by equation (3.11), one may define $\mathbf{e}_{t+\Delta t} = \kappa\mathbf{e}_t$ and substitute it into equation (3.11). Here $|\kappa|$ represents the convergence of the displacement vector toward the final solution \mathbf{u}^* . With some arrangement, the equation becomes

$$\frac{\kappa^2 - (1 + \beta)\kappa + \beta}{\kappa\gamma} \mathbf{e}_t = \mathbf{M}^{-1}\mathbf{K}\mathbf{e}_t. \quad (3.12)$$

This equation can be viewed as an eigenvalue problem regarding the matrix $\mathbf{M}^{-1}\mathbf{K}$ which contains structural information of the system. By means of linear algebra, κ can be evaluated from equation (3.12). For convergence to occur, $|\kappa|$ must be less than one. For the best convergence performance of the dynamic relaxation process, the smallest possible $|\kappa|$ should be obtained. As shown by *Papadrakakis* (1981) and *Oakley and Knight* (1995), the optimal damping factor is given by

$$\alpha_{opt} = 2 \sqrt{\frac{\lambda_{min}\lambda_{max}}{\lambda_{min} + \lambda_{max}}}, \quad (3.13)$$

where λ_{min} and λ_{max} are the minimum and the maximum eigenvalue of the matrix $\mathbf{M}^{-1}\mathbf{K}$, respectively.

The adaptive dynamic relaxation (ADR) method treats the damping factor α , the fictitious mass matrix \mathbf{M} and the time step Δt as integration parameters and strives to optimize the convergence process by choosing an adaptive scheme of integration parameters for the system. We adopt the ADR scheme proposed by *Qiang* (1988), which is one of the top schemes in a comparative analysis of 12 classical DR schemes (*Rezaiee-*

Pajand and Estiri, 2017). In this scheme, the diagonal elements of the fictitious mass matrix is set to the L1 norm of the rows of the stiffness matrix,

$$M_{ii} = \sum_j |K_{ij}|, \quad (3.14)$$

and the damping factor and time step are

$$\alpha = 2 \sqrt{\frac{\omega_0^2}{1 + \omega_0^2}}, \quad (3.15)$$

$$\Delta t = \frac{2}{\sqrt{1 + \omega_0^2}}, \quad (3.16)$$

where $\omega_0 = \sqrt{(\mathbf{u}^T \mathbf{K} \mathbf{u}) / (\mathbf{u}^T \mathbf{M} \mathbf{u})}$ is the minimum frequency of the system. It should be noted that the anti-hourglass force \mathbf{H} corresponds to a stiffness \mathbf{K}_h that should be superimposed onto the one-point quadrature FEM stiffness \mathbf{K}_0 . Therefore, a total stiffness $\mathbf{K} = \mathbf{K}_0 + \mathbf{K}_h$ should be considered when evaluating the ADR integration parameters in this scheme.

3.2.3 Quasi-Static Modeling with Rate- and State-Dependent Friction

The explicit time integration scheme for elastodynamic equations imposes a CFL time step constraint of milliseconds for the sake of numerical stability. Thus, a direct extension of the dynamic FEM code EQdyna for the long-term process of years is computationally impractical. Fortunately, the evolution of faulting behavior during the long-term process between dynamic events is slow and can be viewed as quasi-static. In a

quasi-static process, the inertial effect is negligible and the system is at the equilibrium state at each time step. This approximation converts the governing equations from dynamic to quasi-static and removes the CFL time step constraint, which makes it possible to use longer time steps in simulating the slow deformation processes of an earthquake cycle. The evolution of the quasi-static system is dictated by the time-dependent fault boundary following the RSF law. Here, we adopt the variable time stepping scheme proposed by *Lapusta et al. (2000)* in the spirit of a second-order Runge-Kutta procedure. They observe that in the quasi-static simulation, slower particle velocities should correspond to longer time steps, but the time steps should also satisfy the stability conditions in integrating the constitutive friction laws. Depending on how fast the fault is sliding, the length of the time step varies to ensure both computational efficiency and numerical stability. They derive the following time step constraint from linear stability analysis of the RSF law

$$\Delta t \leq \min_{x_s, x_d} [\xi(x_s, x_d) L(x_s, x_d) / V(x_s, x_d)], \quad (3.17)$$

where ξ is a prescribed parameter, typically a proper fraction, determined by frictional parameters. The pair (x_s, x_d) are the strike and dip coordinates of the discretized two-dimensional fault surface. This criterion implies that slip over the fault surface within one time step is limited to a fraction of the characteristic slip distance L , which leads to an upper bound for the feasible time step in the simulation.

The key features of the quasi-static simulation procedure are summarized here. Suppose slip δ_t , slip velocity V_t and state variable θ_t are all known at the same time t .

According to the time step constraint, the slip velocity V_t over the fault determines the time step length Δt . To solve for these quantities at the next moment $t + \Delta t$, we first make predictions of the slip and state variable at $t + \Delta t$ by

$$\delta^* = \delta_t + V_t \Delta t, \quad (3.18)$$

$$\theta^* = G(\theta_t, V_t, \Delta t), \quad (3.19)$$

where function G is the explicit integration of the aging law. Assuming the new slip δ^* on the fault as a fixed boundary condition, the corresponding static elastic tractions, including shear traction $\tau_e(\delta^*)$ and effective normal traction $\sigma_e(\delta^*)$, are computed using the aforementioned ADR technique. Further, the quasi-static assumption neglects the trivial inertial effect in the slow processes and equates the elastic traction $\tau_e(\delta^*)$ to the rate- and state-dependent frictional strength τ_f

$$\tau_f[\sigma_e(\delta^*), V^*, \theta^*] = \tau_e(\delta^*). \quad (3.20)$$

Since $\tau_e(\delta^*)$, $\sigma_e(\delta^*)$ and θ^* are known, the new slip velocity V^* can be easily found by solving equation (3.20). We then make another predictions of the slip δ^{**} and state variable θ^{**} at $t + \Delta t$ using the average of the slip velocity V_t at current time t and the new slip velocity V^*

$$\delta^{**} = \delta_t + \frac{V_t + V^*}{2} \Delta t, \quad (3.21)$$

$$\theta^{**} = G\left(\theta_t, \frac{V_t + V^*}{2}, \Delta t\right). \quad (3.22)$$

Again, use the ADR method to evaluate $\tau_e(\delta^{**})$ and $\sigma_e(\delta^{**})$, then solve equation (3.20) with the new θ^{**} for a new slip velocity V^{**} . Finally, adopt δ^{**} , θ^{**} and V^{**} as the numerical estimates $\delta_{t+\Delta t}$, $\theta_{t+\Delta t}$ and $V_{t+\Delta t}$ at time $t + \Delta t$.

The function G is used twice in each time step to integrate the state variable θ . We employ the following form

$$G(\theta, V, \Delta t) = \frac{L}{V} + \left(\theta - \frac{L}{V} \right) \exp \left(-\frac{V\Delta t}{L} \right). \quad (3.23)$$

which is an explicit solution to the aging law assuming the velocity is constant. *Noda and Lapusta* (2010) have compared three different forms of the state variable integration under a two-iteration scheme. They theoretically show that two of them are second-order accurate and the remaining one is only first-order accurate. The updating method we apply here for the state variable integration differs from the two-iteration scheme they discussed. While they advance θ for the first half time step using the known velocity at time t and then the second half time step using a corrected velocity, we advance θ for a whole time step twice using equation (3.23), first with the known velocity and then with a corrected slip velocity. Following the line of their mathematical argument, our integration method can be shown to be of second-order accuracy.

We treat interseismic tectonic loading as an external source of deformation and impose the loading rate to the outer boundaries of the model. At every quasi-static moment, free boundary conditions are applied at the free surface and the bottom at depth, and fixed (Dirichlet) boundary conditions are specified on part of the lateral boundaries of the model domain to account for far-field plate motions. Similar to the fault boundary,

these lateral boundaries are held fixed at every quasi-static moment but the fixed value evolves linearly over time at a prescribed constant loading rate. Different fault geometries require different settings to impose appropriate loading from these boundaries onto the fault. More details of boundary condition configuration will be discussed in section 2.5.

In the quasi-static processes, the faulting behavior develops steadily from the interseismic phase to the nucleation phase under the control of the RSF law. Therefore, the frictional parameters are crucial for dynamic instability to occur on the fault. In the aging law (3.7), equating $d\theta/dt$ to zero provides the condition for steady state sliding, that is, $\theta_{ss} = L/V_{ss}$, where θ_{ss} and V_{ss} are steady-state state variable and slip velocity, respectively. The corresponding steady state frictional strength τ_{ss} is then given as $\tau_{ss} = \sigma[f_0 + (a - b) \ln(V_{ss}/V_0)]$. When $a - b > 0$, τ_{ss} is positively correlated with V_{ss} and is called steady state velocity strengthening (VS). Similarly, when $a - b < 0$, τ_{ss} is negatively correlated with V_{ss} and is called steady state velocity weakening (VW). A region on the fault with velocity weakening property is a necessary condition for dynamic rupture to nucleate, and is often a numerical representation for the observed seismogenic zone of a realistic fault in the lithosphere. For instability to occur, this VW zone must be larger than a critical nucleation patch size h^* which is determined by the energy balance of a quasi-statically expanding crack. Various theoretical estimates for h^* are proposed (e.g. *Rice, 1993; Lapusta et al., 2000; Rubin and Ampuero, 2005*). An estimate for three-dimensional modeling (*Chen and Lapusta, 2009; Lapusta and Liu, 2009*) is

$$h^* = \frac{\pi}{2} \frac{\mu^* b L}{(b - a)^2 \sigma}. \quad (3.24)$$

The critical nucleation dimension h^* plays two important roles in earthquake cycle simulations. First, its ratio to the VW zone width W is an important indicator of fault response pattern, such as aseismic oscillation or seismic sequences (*Liu and Rice, 2007; Rubin, 2008*). Second, its ratio to the element size imposes a spatial resolution constraint on the model discretization in the sense that the element size should be sufficiently smaller than h^* to avoid slip instability occurring on a single element during the simulation (*Rice, 1993; Lapusta et al., 2000; Liu and Rice, 2007*).

3.2.4 Integrated Modeling of Full Earthquake Cycles

The full earthquake cycle simulation consists of both dynamic and quasi-static processes. In our method, the two states are handled differently using the aforementioned dynamic code and the quasi-static method. The quasi-static method is used when the fault is slowly creeping (low slip velocity), and the dynamic code is directly used when the fault experiences fast slip (high slip velocity). We choose the maximum slip velocity V_{max} over the whole fault as an indicator to represent the intensity of fault sliding, because V_{max} is directly related to the time step constraint in the quasi-static simulation. The quasi-static simulation is switched to the dynamic simulation when V_{max} crosses V_{thr} , a threshold value, from below to above, and vice versa. The selection of V_{thr} is based on the balance between numerical accuracy and computational efficiency. With some numerical experiments, we found that an empirical threshold value near 0.01 m/s is suitable for dividing the two states, a value consistent with the choice of seismic limit in *Chen and*

Lapusta (2009) that defines the separation of seismic and aseismic slip rates. If V_{thr} is too large, such as 0.1 m/s, the simulation may use the quasi-static method to simulate a dynamic process when the inertial effect has already become significant. If V_{thr} is too small, such as 0.001 m/s, the simulation that is still undergoing a slow process may be switched prematurely to the dynamic phase with a unreasonably small dynamic time step that significantly slows down the simulation. In practice, we use $V_{thr} = 0.01$ m/s for the quasi-static to dynamic transition, and $V_{thr} = 0.005$ m/s for the dynamic to quasi-static transition, to prevent the system from oscillating between the two states when V_{max} is around the transition threshold.

The full earthquake cycle simulation starts with the interseismic phase that is handled by the quasi-static method. An initial slip velocity V_{ini} , an initial effective normal stress σ_0 and a corresponding initial steady state shear stress $\tau_0 = \sigma_0[f_0 + (a - b) \ln(V_{ini}/V_0)]$ are assumed on the fault. The initial state variable for steady state is given as $\theta_{ini} = L/V_{ini}$. To initiate the simulation, artificial perturbation is added by imposing a nucleation patch on the fault where steady-state shear stress is higher than the background. Slip within the nucleation patch accelerates until V_{max} on the fault exceeds the threshold V_{thr} , then we switch to the dynamic method which takes specific physical quantities on the fault at the end of the preceding nucleation phase as the initial condition. These quantities include the fault node particle velocities, the state variable, and the normal and shear stresses. The coseismic rupture grows and arrests spontaneously, with seismic waves radiating from the fault, propagating in the medium and being absorbed by the PML boundary of the model. When slip on the fault settles and V_{max} drops back to below V_{thr} ,

the coseismic phase ends and the postseismic phase begins. We switch back to the quasi-static method and use the output of the on-fault quantities of the coseismic phase as the initial condition for the postseismic phase. Under the quasi-static framework, the fault evolves through the postseismic, interseismic, and nucleation phases successively, until V_{max} exceeds V_{thr} again. The quasi-static and dynamic methods are applied alternately to simulate the four phases and the whole process repeats to perform multiple earthquake cycle simulations. At each transition between the two methods, the numerical mesh is reset and the fault geometry is preserved. Transferring the on-fault quantities when switching the methods ensures the continuity of the earthquake cycle simulation. Therefore, except for the first nucleation which is triggered by artificial perturbation added to the assumed initial condition, the nucleation in the subsequent events is part of the solution, dictated by stresses that spontaneously evolve from the previous events under the influence of tectonic loading.

3.2.5 Fault Geometry and Model Configuration

The FEM dynamic code EQdyna is naturally suitable for complex geometrical structures. Therefore, the earthquake cycle method developed based on EQdyna inherits such an advantageous property and is ready for simulations on complex fault systems. In this initial study, we work on two types of fault geometry, the vertical fault and the shallow-dipping thrust fault. The vertical fault is used to verify the method, and we apply the method to study earthquake cycle behaviors of the thrust fault. The fault boundary

embedded in the three-dimensional uniform linear elastic half-space separates the finite model domain into two blocks. The vertical fault is placed in the x-z plane of the Cartesian coordinate system (Figure 3. 1a). The thrust fault boundary tilts at a dip angle ϕ and intersects the free surface at the x-axis on the top of the model (Figure 3. 1b). The code uses the traction-at-split-node (TSN) method to characterize the discontinuity of the fault boundary (Andrews, 1999; Day *et al.*, 2005). Specifically, we represent the thrust fault geometry using the degeneration technique (Duan, 2010; Duan, 2012; Luo and Duan, 2018), which cuts through a hexahedral element to create discontinuity and divides the element into two wedges. In this study, the element is cut along the diagonal of the lateral faces that are parallel to the y-z plane. The hexahedral elements are designed to have special aspect ratio on the y-z faces such that the diagonal of the y-z faces is aligned with the dipping fault geometry with desired dip angle ϕ . Specifically, we choose $\Delta y = \Delta x \cos \phi$ and $\Delta z = \Delta x \sin \phi$ in order to form square on-fault elements. Note that in this design, Δx_{min} varies with different ϕ , which leads to different stable time step lengths in the different dynamic models according to the CFL condition (3.5).

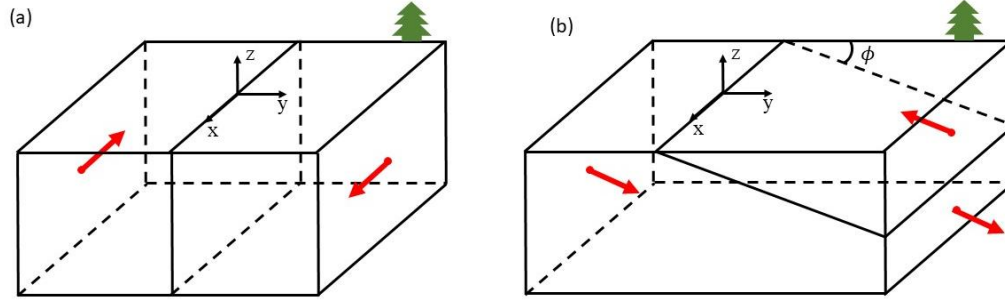


Figure 3. 1 Schematic diagrams that show (a) a right-lateral strike-slip planar fault model and (b) a thrust planar fault model with dip angle ϕ . The fault boundary completely separates the model domain into two blocks to avoid singular solution. The red arrows represent the major movement direction of the blocks.

In this study, we mainly investigate five different fault models based on the vertical and thrust fault geometry. They include a vertical strike-slip fault model, a vertical dip-slip fault models, and three pure-thrust fault models with dip angles of 45° , 30° and 15° . Note that the vertical dip-slip fault geometry is for comparison purpose only in this study, since it is rarely seen in nature. Boundary condition configurations during the quasi-static process vary from model to model, depending on the fault geometry and the plate motion. For this study, there are three types of boundary condition configurations associated with the six fault models. In general, the top surface and the bottom boundary in these models are assumed traction-free. For the vertical strike-slip fault model, tectonic loading is implemented as $u_x = V_{pl}t/2$ on the $y = y_{max}$ boundary and $u_x = -V_{pl}t/2$ on the $y = y_{min}$ boundary. In addition, u_y is fixed to zero on all the lateral boundaries. For the vertical dip-slip fault models, the tectonic displacements that drive the blocks moving along dip

direction are $u_z = V_{pl}t/2$ on the $y = y_{max}$ boundary and $u_z = -V_{pl}t/2$ on the $y = y_{min}$ boundary. Also, u_y is fixed to zero on all lateral boundaries, and u_x is fixed on the boundaries $x = x_{max}$ and $x = x_{min}$. For the thrust faults, the downgoing displacement of the footwall is along the downdip direction parallel to the fault plane and is assigned on the $y = y_{min}$ boundary and part of the $y = y_{max}$ boundary that belongs to the footwall. The opposite upgoing displacement of the hanging wall is in the updip direction parallel to the fault plane and is assigned on part of the $y = y_{max}$ boundary that belongs to the hanging wall. Additionally, u_x is fixed to zero on the boundaries $x = x_{max}$ and $x = x_{min}$. In these models, the displacement components that are not mentioned on the outer boundaries are set to be free. Note that the time-dependent displacement on the outer boundary of the models prescribes the displacement value for the fixed boundary condition at each quasi-static time step, similar to the treatment to the slip quantity on the fault boundary controlled by the constitutive friction law.

Parameter values used in this study are summarized in Table 3. 1. As discussed in section 2.1 and 2.3, spatial resolution conditions (3.5) and (3.24) require appropriate selection of element size. Given the frictional parameters and elastic bulk properties listed in Table 3. 1, $h^* = 13$ km for mode II and 10 km for mode III, $\Lambda_0 = 472$ m for mode II and 353 m for mode III. Apparently, the physical scale of the cohesive zone size dominates the numerical constraint on grid size. We carry out grid resolution tests to compare the performance of various grid sizes in dynamic rupture simulation using the parameters listed in Table 3. 1. Figure 3. 2 compares the dynamic slip profiles along strike and dip directions of these dynamic tests and demonstrates that the results of $\Delta x = 200$ m

are adequately close to those of $\Delta x = 100$ m. The test of $\Delta x = 400$ m shows obvious deviation from the other two tests in the results. Considering the balance of numerical accuracy and computational efficiency, we choose $\Delta x = 200$ m for the subsequent numerical experiments in this study.

Table 3. 1 Summary of Model Parameters in This Study

Parameter	Value
Large fault size Ω_1	60 km by 30 km
Large fault VW zone length L_{s1}	36.3 km
Large fault VW zone width W_{s1}	18.3 km
Small fault size Ω_2	40 km by 25 km
Small fault VW zone length L_{s2}	29.5 km
Small fault VW zone width W_{s2}	15.7 km
P-wave speed v_p	6000 km/s
S-wave speed v_s	3464 km/s
Shear modulus μ	32 GPa
Poisson's ratio ν	0.25
Density ρ	2670 kg/m ³
RSF parameter a in VW zone	0.012
RSF parameter b in VW zone	0.016
Characteristic slip distance L	0.01 m
Reference slip velocity V_0	10 ⁻⁶ m/s
Steady state friction coefficient f_0	0.6
Uniform effective normal stress σ_{ini}	50 MPa
Loading rate V_{pl}	10 ⁻⁹ m/s
Element edge length in x direction Δx	200 m

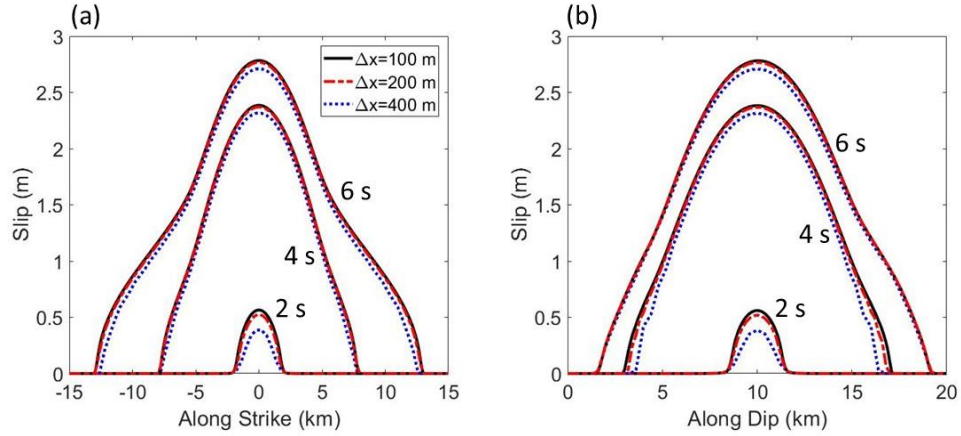


Figure 3. 2 Comparison of (a) along-strike and (b) along-dip dynamic slip profiles in grid resolution tests with grid size of 100 m, 200 m, and 400 m. These dynamic rupture tests use the large fault geometry Ω_1 and model parameters presented in Table 3. 1. Slip profiles at 2 s, 4 s, and 6 s are shown.

We set up two kinds of fault dimensions for the five fault models, including a larger one for a vertical strike-slip fault model and a smaller one for a strike-slip fault model and three thrust fault models. The use of a smaller size of fault area is for better computational efficiency in solving equations on the degenerated FEM mesh used in thrust fault models. The larger fault surface Ω_1 is 60 km along strike and 30 km along dip. Spatial distribution of frictional parameters for the larger fault is shown in Figure 3. 3, with a uniform velocity-weakening area that ranges from -17.5 km to 17.5 km along strike and from 4 km to 20.5 km along dip. The parameters a and b are uniform inside this area and linearly transitioned to velocity-strengthening values at the periphery of the area, therefore, the seismogenic zone where $a - b > 0$ is slightly larger than the uniform VW

area. The smaller fault surface Ω_2 is 40 km by 25 km, with a smaller uniform VW zone ranging from -13.5 km to 13.5 km along strike and from 4 km to 17.5 km along dip. For all models, we consider homogenous initial effective normal stress $\sigma_{ini} = 50$ MPa throughout the fault surface by assuming fluid overpressurization that keeps the difference between lithostatic stress and hydrostatic pore pressure a constant. Initial slip velocity V_{ini} over the fault is set to the loading rate V_{pl} , in the direction parallel to the loading displacement assigned on the outer boundary. Initial steady state shear traction τ_{ini} is in the same direction but with a heterogeneous magnitude determined by $\tau_{ini} = \sigma_{ini}[f_0 + (a - b) \ln(V_{ini}/V_0)]$. In the uniform VW area, $\tau_{ini} = 31.38$ MPa.

The earthquake cycle simulation is initiated by a patch of artificially high initial steady state shear stress, which is 2% higher than the background value in the VW zone. The high stress corresponds to an initial slip rate roughly 20 times smaller than the background value, which leads to immediate stress concentration at the edge of the patch after the simulation begins. For the large fault surface, the 12 km by 9 km patch is located between -7 km and 5 km along strike and between 12 km and the bottom edge of the VW zone along dip (Figure 3. 3). For the small fault surface, the 10 km by 8 km patch is located between -6 km and 4 km along strike and between 9 km and the bottom edge of the VW zone along dip. The patch is set slightly off the central point of the fault to avoid a perfect symmetric setting because earthquake cycle simulation is a nonlinear process that easily gives unpredictable asymmetric results for symmetric settings after a long simulation time (*Erickson and Day, 2016*).

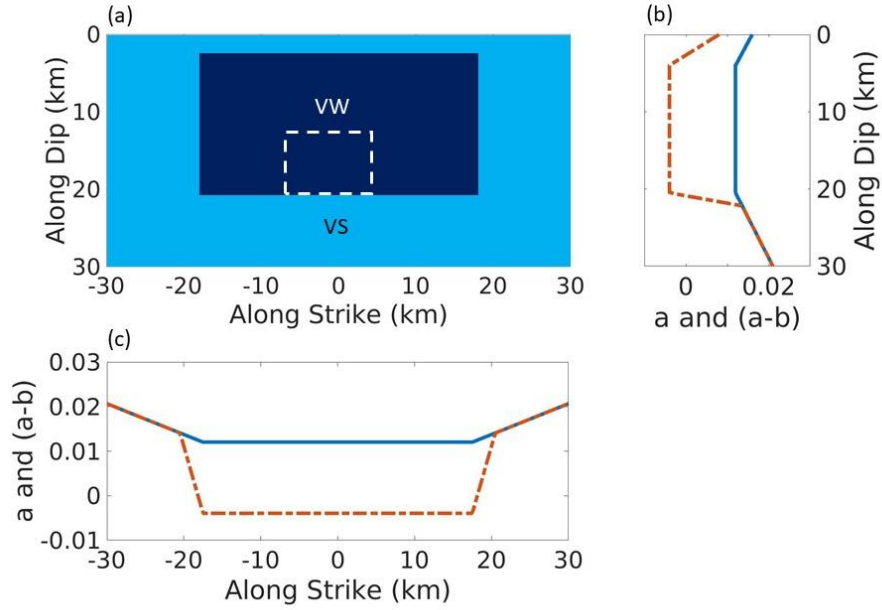


Figure 3.3 Spatial distribution of frictional parameters on the large fault surface. (a) shows spatial areas of $a - b < 0$ (dark blue) and $a - b > 0$ (light blue). (b) shows the vertical profile of a (blue curve) and $a - b$ (red curve) at $x_s = 0$. (c) shows the horizontal profile of same parameters at $x_d = 10$ km. The central area where $a - b < 0$ is the seismogenic zone with steady state velocity weakening property (VW). The surrounding area outside the seismogenic zone where $a - b > 0$ is the stable creep area with steady state velocity strengthening property (VS). High initial shear stress is assigned in the rectangular patch marked by the dashed white line to artificially initiate the first event in the earthquake cycle simulation.

Earthquake cycle simulations in this study have been done in parallel with MPI implementation. The strike-slip fault model with large fault surface Ω_1 and element size $\Delta x = 200$ m has about 2.8 million elements. The thrust fault models with small fault surface Ω_2 and the same element size, have about 5.4 million elements. Using 400 cores on a supercomputer system with 2.5 GHz 10-core Intel Xeon E5-2670 v2 processors, the

strike-slip fault model with Ω_1 fault surface takes about 6.8 minutes of wall-clock time on average in each dynamic rupture simulation and 44.4 minutes on average in each quasi-static simulation. Computational cost for thrust fault models generally increases as the dip angle becomes shallower and shallower, since the minimum element length determines the time step constraint in simulation. Roughly speaking, with the same number of cores on the same cluster, the thrust fault models with Ω_2 fault surface take about 15~30 minutes of wall-clock time in each dynamic rupture simulation and 1~2 hours in each quasi-static simulation.

3.3 Verification of the Dynamic Earthquake Simulator

3.3.1 Quasi-Static Simulation Benchmark

We test the ADR method against the analytic displacement solution of a two-dimensional anti-plane benchmark problem of an ideal transform fault model presented in the work by *Savage and Prescott (1978)*. As shown in Figure 3. 4a, the vertical fault at $x = 0$ in the Earth is assumed uniform along strike and separates two elastic plates that move in the opposite directions along the strike. The plates are moving at prescribed constant rate $\pm v$ at remote distance from the fault and at depth deeper than $z = D$ on the fault, where the plus sign denotes the plate at $x > 0$ and the minus sign denotes the plate at $x < 0$. The fault area above $z = D$ up to the free surface $z = 0$ is assumed locked for a period of T . After a cycle of T , the relative displacement between the two plates at far-field and at depth $z = D$ below is $2vT$ while the slip on the locked zone of the fault remains

zero. Then, a sudden slip of $2vT$ is applied to the locked area and the surrounding region catches up with the far field plate motion, which represents the seismic release of the accumulated elastic stress in the two plates. In this model, an analytic solution to the displacement evolution at the free surface $z = 0$ over n cycles is given as

$$\frac{u(x, 0, t)}{2vT} = \pm \frac{n}{2} + \frac{t - nT}{\pi T} \tan^{-1} \frac{x}{D}, \quad nT < t < (n + 1)T. \quad (3.25)$$

Without loss of generality, we consider the displacement evolution when $n = 0$, which leads to $u(x, 0, t) = (2vt/\pi) \tan^{-1}(x/D)$, where $0 < t < T$. At any time t , the displacement field $u(x, 0, t)$ is an analytic static solution to this ideal earthquake cycle problem. Assuming $2v = 32$ mm/yr, $T = 50$ yr, we can also solve the elastostatic equations numerically using the code EQdyna together with the ADR method. Selected results of every 10 years are shown in Figure 3. 4b. The numerical results exhibit a good agreement with the analytic solutions and prove the applicability of the methodology – using EQdyna with the ADR to simulate the quasi-static processes of an earthquake cycle.

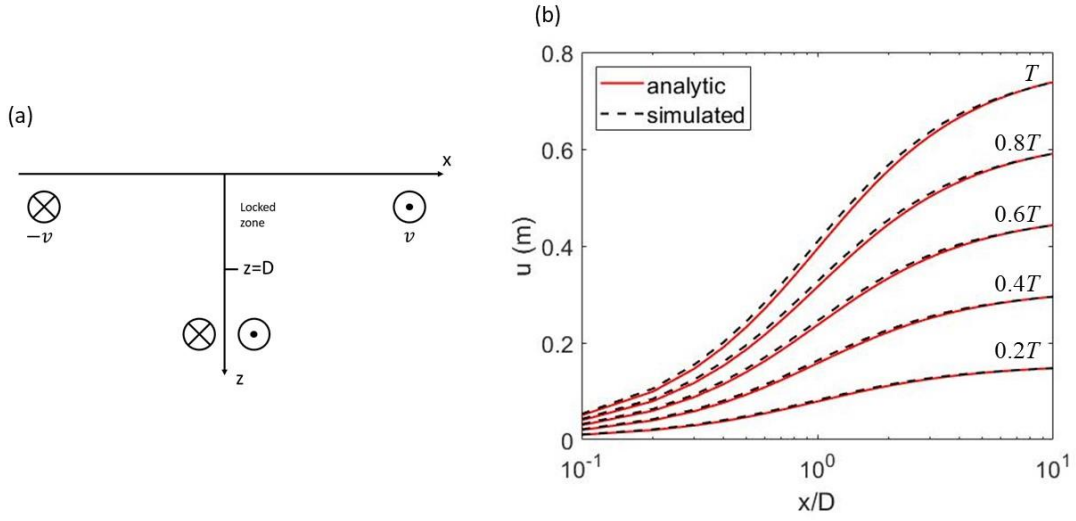


Figure 3. 4 (a) A schematic diagram showing the two-dimensional anti-plane vertical fault geometry for an ideal earthquake cycle benchmark problem. (b) Comparison of the analytic (solid) and numerical (dashed) solutions of the displacement distributions at the free surface every 10 years in an earthquake cycle of 50 years. The horizontal coordinate x is normalized by the width D of the locked zone and presented in a logarithmic scale. The results are anti-symmetrical about the fault and thus only the $x < 0$ part is shown.

3.3.2 Earthquake Cycle Simulation on a Vertical Strike-Slip Fault

Since there is no analytical solution for the nonlinear governing equations of earthquake cycle simulation with full elastodynamics, we rely on qualitative comparison of our method with other dynamic earthquake cycle modeling study. Three-dimensional earthquake cycle simulation on a vertical strike-slip fault was first carried out by *Lapusta and Liu* (2009) using a boundary integral method. Here we reproduce comparable

simulation using our newly developed earthquake cycle simulator based on the finite element method.

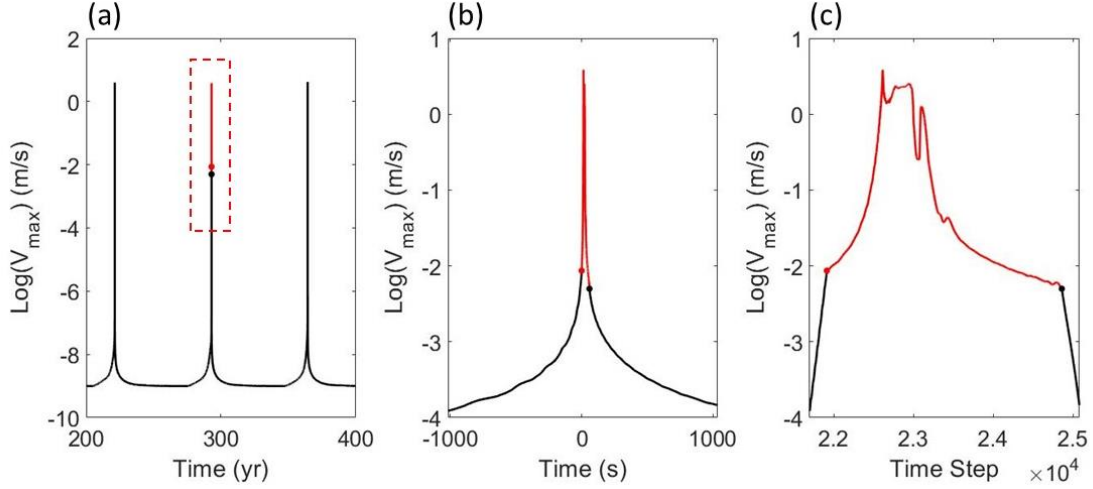


Figure 3. 5 Logarithmic maximum slip rate history of the fifth cycle in various time scales. (a) shows part of the simulated earthquake sequence (black curve) from 200 to 400 years, in which the fifth event (red curve) occurs in year 293. Red dot marks the onset of the dynamic process, and black dot marks the onset of the quasi-static process. Evolution details of V_{\max} in the red dashed box are shown in (b) time scale of seconds and (c) simulation time steps. The start and the end of data in (b) correspond to the first and the last time step shown in (c). The time origin in (b) is reset to the beginning of the dynamic event.

The simulated earthquake sequence on the vertical strike-slip fault of area Ω_1 has an average recurrence interval $T_r = 72$ years and an average seismic moment $M_0 = 3.6 \times 10^{19} \text{ N} \cdot \text{m}$, which amounts to Mw 7 in moment magnitude. The average seismic slip per

event $\bar{\delta}_{seis}$ is 1.69 m, which constitutes 75% of the total fault slip $\bar{\delta}_{tot} = V_{pl}T_r = 2.27$ m over an average recurrence interval. In other words, the seismic coupling coefficient defined as $\chi = \bar{\delta}_{seis}/\bar{\delta}_{tot}$ is 0.75 for this run. Figure 3. 5 shows temporal details of the faulting evolution of the fifth cycle. The fault is at the quasi-static state in most of the time. The maximum slip rate has reached 10^{-4} m/s at about 1000 s before the dynamic process occurs. The dynamic process lasts for 59 s and then returns to the quasi-static state. In the following 1000 s, the maximum slip rate drops back to 10^{-4} m/s. The transitions between the two states are obvious as the shape of the curve changes abruptly in the equally time stepping illustration (Figure 3. 5c), but these transitions become smooth and indiscernible when the variable time steps are taken into consideration (Figure 3. 5b).

Spatial details of faulting evolution of the fifth cycle are illustrated in Figure 3. 6. After decades after the fourth event (Figure 3. 6a), the seismogenic zone with steady state velocity weakening property is mostly locked at a prescribed slip rate of 10^{-12} m/s. The surrounding area with steady state velocity strengthening property is creeping at the tectonic loading rate $V_{pl} = 10^{-9}$ m/s. During the interseismic phase (Figure 3. 6a-d), the sharp change of slip rate at the periphery of the locked zone induces elastic stress that drives the periphery into the center of the locked zone. As the periphery moves inward from all directions, the trailing slip rate starts to accelerate, especially the area to the upper right of the locked zone in Figure 3. 6d. This accelerated patch forms a slowly propagating front that travels aseismically around the locked zone that continuously shrinks (Figure 3. 6e). It develops into an elliptical nucleation patch that leads to the fifth event (Figure 3. 6f). Once V_{max} exceeds V_{thr} , simulation switches from the quasi-static method to the

dynamic method and the coseismic phase begins. The nucleation patch to the lower left of the tiny remaining locked zone (Figure 3. 6g) grows spontaneously into dynamic rupture that expands in all directions within the VW zone (Figure 3. 6h), arrests by the VS zone (Figure 3. 6i) and vanishes eventually (Figure 3. 6j). As V_{max} falls below V_{thr} , simulation returns to the quasi-static method. Postseismic slip rate gradually decreases over the ruptured area, and at the same time the affected area in the VS zone continues to expand, causing afterslip (Figure 3. 6k). As postseismic slip rate continues decreasing, the fault returns to its interseismic state and a cycle is completed (Figure 3. 6l). Similar faulting behavior occurs in the following interseismic (Figure 3. 6m) and nucleation (Figure 3. 6n and o) phases, except that the whole pattern is reversed laterally this time.

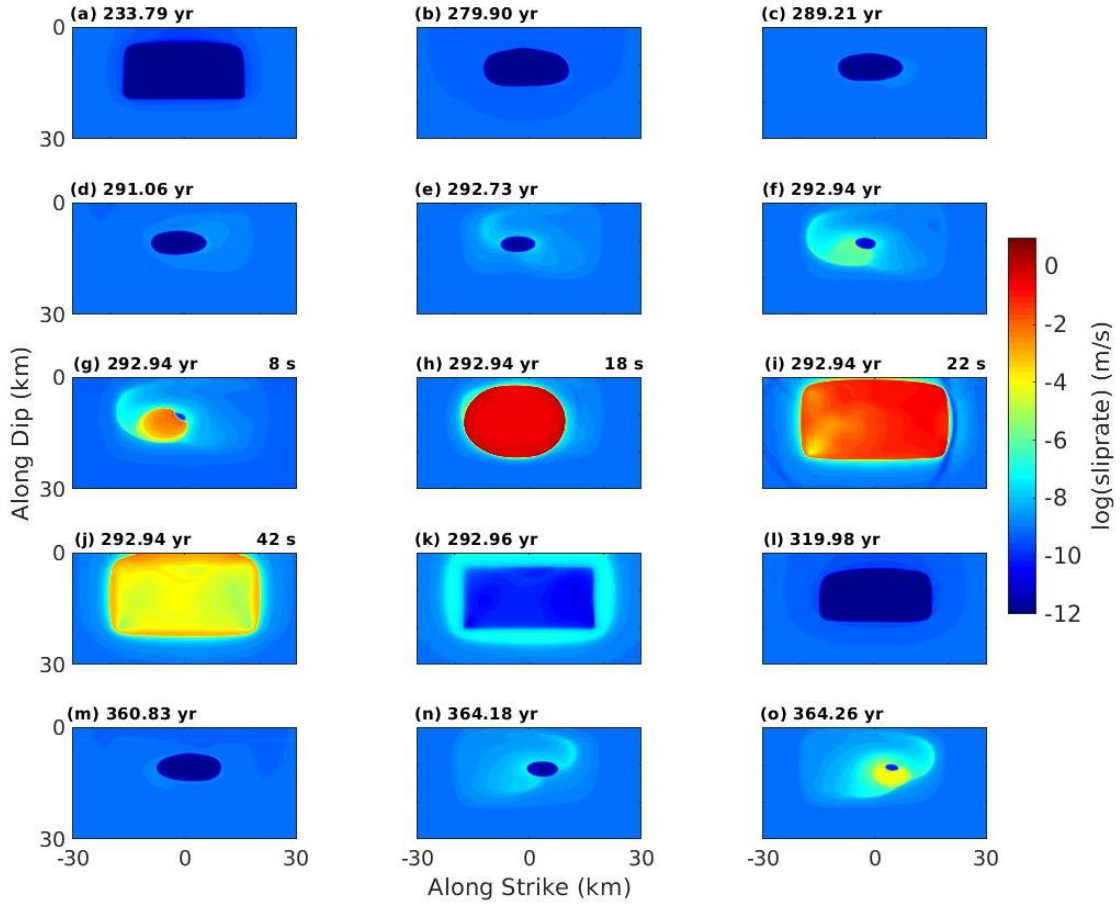


Figure 3. 6 Snapshots of slip rate spatial distribution on the vertical strike-slip fault surface of Ω_1 from the interseismic phase before the fifth event to the nucleation phase before the sixth event. Slip rate in log scale ranges from 10^{-12} m/s (interseismic locking) to 1 m/s (seismic slip). The elapsed time of the snapshot from the beginning of the run is shown at the top left corner. For the coseismic snapshots, the elapsed time from the switch moment is also shown at the top right corner. Snapshots are selected to illustrate key features observed in the earthquake cycles: (a-d) interseismic, (e-f) nucleation, (g-j) coseismic, (k) postseismic, (l-m) interseismic, (n-o) nucleation.

This faulting pattern is also seen in previous earthquake cycle studies (*Lapusta and Liu, 2009; Erickson and Day, 2016*), with a relatively large L that leads to $W/h^* \sim 1$ and the resultant periodic two-event pattern. Moreover, the average recurrence time and seismic moment of the simulated sequence is highly consistent with the scaling relation fitting the repeating small earthquakes along the Parkfield segment of the San Andreas fault (*Nadeau and Johnson, 1998*). This scaling relation, which has been confirmed universal by independent observations in other environments (*Chen et al., 2007*) as well as numerical experiments (*Chen and Lapusta, 2009*), predicts 73.4 years for Mw 7 earthquakes. Although such magnitude of the simulated events is at the high end of the scaling relation, the developed methodology is still reasonably verified for its applicability in earthquake cycle simulations.

3.4 Application of the Dynamic Earthquake Simulator: Earthquake Cycle Behaviors of Thrust Faults

We examine a group of experiments on three-dimensional thrust faults with various dip angles ($\phi = 90^\circ, 45^\circ, 30^\circ, 15^\circ$) to understand how thrust fault geometry may affect the behavior of earthquake sequences. Asymmetric dipping fault geometry has been shown to have large effects on individual dynamic events, including rupture propagation and resultant ground motion (*Oglesby et al., 1998; Oglesby et al., 2000*). These fault models have a smaller size of fault area Ω_2 and correspondingly smaller VW zone Ω_{VW} for better computational efficiency in solving equations on the degenerated FEM mesh.

Model configurations except for the dip angle are kept identical in order to study the effect of asymmetric fault geometry on earthquake cycle behavior. Major characteristics are summarized in Table 3. 2. The average recurrence interval has obvious inverse relation with the dip angle. For instance, the 15° dipping thrust fault has an average interval about 40 years longer than that of a 90° dipping fault. In fact, as shown in Figure 3. 7a, the average interval scales well with $\sin \phi$ following a fitted linear relation

$$T_r = -43.2 \sin \phi + 107, \quad (3.26)$$

Here T_r is in years and ϕ in degrees between 0 and 90° . Note that due to the finite range of dip angle, this apparent relation describes limited variation of recurrence interval from about 100 years to 60 years with respect to the dip angle, given a certain configuration of the fault model. The average seismic moment M_0 also scales with $\sin \phi$ in an inversely linear relation (Figure 3. 7b)

$$M_0 = -1.76 \sin \phi + 4.17, \quad (3.27)$$

Here M_0 is in a unit of $10^{19} \text{ N} \cdot \text{m}$ for convenience. Both quantities have a simple inverse linear relation with $\sin \phi$, which implies a linear relation between these two quantities. The exponent between T_r and M_0 (the slope of the fitted $\log T_r - \log M_0$ curve) we obtained in our numerical experiments is about 0.77 (Figure 3. 7c). Since $\bar{\delta}_{tot} = V_{pl} T_r$ and $\bar{\delta}_{seis} = M_0 / \mu / \Omega_{VW}$, these two average slip quantities are also positively correlated, resulting in a roughly constant seismic coupling coefficient χ in a narrow range of 80%~84%. The average stress drop for each event lies within a reasonable range of 3~4 MPa, without significant correlation with the dip angle.

Table 3. 2 Measured Quantities of Earthquake Cycles on Various Thrust Fault Models

ϕ	T_r (yr)	M_0 (N · m)	$\bar{\delta}_{seis}$ (m)	$\bar{\delta}_{tot}$ (m)	$\Delta\bar{\tau}$ (MPa)
90°	63.8	2.4×10^{19}	1.60	2.01	3.28
45°	75.7	3.0×10^{19}	1.99	2.38	3.82
30°	86.7	3.3×10^{19}	2.23	2.73	4.15
15°	95.2	3.7×10^{19}	2.48	3.00	3.92

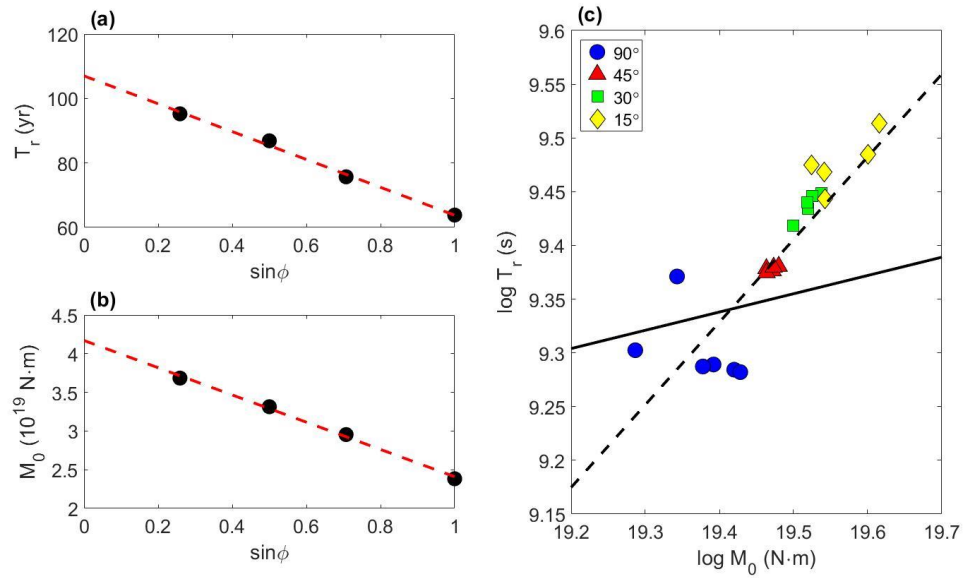


Figure 3. 7 Scaling of (a) the average recurrence interval and (b) the average seismic moment with respect to $\sin \phi$ of various thrust fault models. Red dashed lines denote the least squares fitted lines of the data. (c) shows the $T_r - M_0$ relation of all the events in simulated earthquake sequences of the four dip-slip fault models. Note that both quantities are in log scale and T_r is in seconds. The black dashed line passing through the simulated data represents the fitted line of the simulated events and suggests a relation $T_r \propto M_0^{0.77}$. The black solid line, which suggests $T_r \propto M_0^{0.17}$, represents the fitted line of the observed repeating small earthquakes (more than 90% right-lateral strike-slip) in the Parkfield segment of SAF where repeating M6 events are expected (Nadeau and Johnson, 1998).

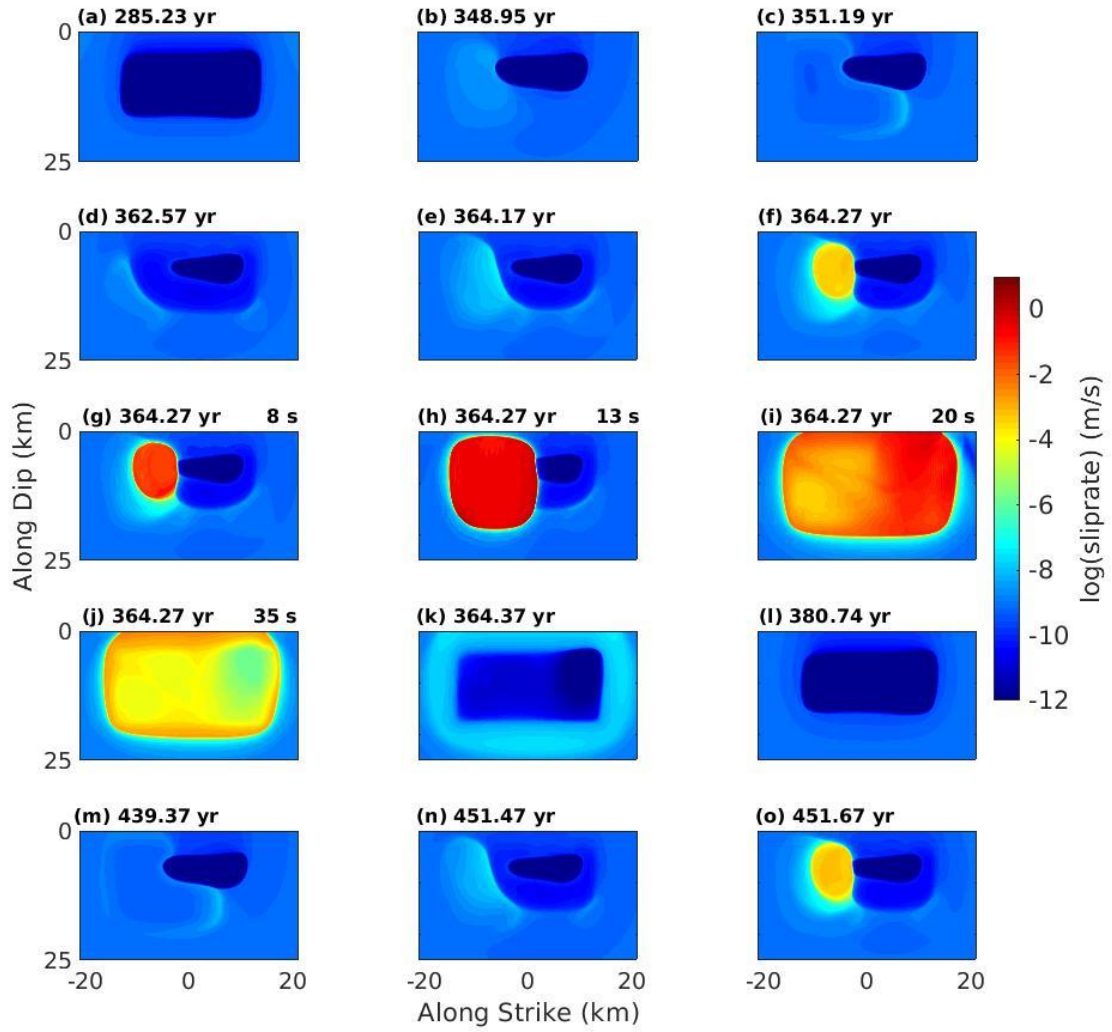


Figure 3. 8 Snapshots of slip rate spatial distribution on the 30° dip thrust fault surface of Ω_2 from the interseismic phase before the fifth event to the nucleation phase before the sixth event. Similar to Figure 3. 6, snapshots are selected to illustrate key features observed in the earthquake cycles: (a-d) interseismic, (e-f) nucleation, (g-j) coseismic, (k) postseismic, (l-m) interseismic, (n-o) nucleation.

Figure 3. 8 illustrates typical features of the faulting behavior on the 30° dip thrust fault. Figure 3. 8a and b show the gradual inward propagation of the periphery of the locked zone, which exhibits notable difference between the left edge and the right edge of the locked zone. The left propagating edge dominates the interseismic evolution process and reaches a much further distance inside the locked zone than the right edge. A slightly accelerated patch emerges on the left of the VW zone. The patch excites aseismic fronts that propagate around the locked zone (Figure 3. 8c). After the aseismic transient settles, another aseismic front initiates from the left edge of the VW zone (Figure 3. 8d), which propagates inward toward the remaining locked patch and directly leads to nucleation in the accelerated area (Figure 3. 8e and f). In addition, the roughly elliptical shape of the nucleation patch has a major axis along dip direction, which is different from the one observed in the strike-slip run (Figure 3. 6f and g) but is consistent with the expression (3.24) that the mode II nucleation patch dimension is greater than mode III dimension. In the coseismic phase, since the nucleation locates on the left side of the VW zone (Figure 3. 8g), the initiated rupture is soon bounded on the left and mainly propagates unilaterally toward the right. The rupture is eventually terminated on the right edge of the VW zone (Figure 3. 8h-j). With a stronger rupture front in the dip direction, the dynamic rupture penetrates the VS zone near the free surface and shakes the ground (Figure 3. 8i). In contrast, the dynamic rupture in the strike-slip test run barely touches the free surface (Figure 3. 6i). Postseismic slip behaves similarly in both runs, and the cycle ends as the fault returns back to the interseismic state (Figure 3. 8k and l). Identical faulting behavior

repeats in the interseismic and nucleation phases (Figure 3. 8m-o), without alteration of the nucleation location as shown in the strike-slip fault simulation (Figure 3. 6).

Figure 3. 9 compares the fault slip evolution over multiple earthquake cycles for all four dip-slip fault models. Without changing the frictional parameters and elastic bulk properties, these models have identical critical nucleation patch size as the previous two models with a larger fault surface area. Therefore, it is unsurprising that the 90° dipping fault model with smaller Ω_{VW} exhibits variable nucleation locations in its earthquake sequence. However, the nucleation location changes only for three times in the entire sequence of nine events (not shown). The first time occurs at the second event, the second time at the sixth event (the fourth dynamic event shown in Figure 3. 9a), and the third time at the ninth event. Before the nucleation location shifts from one side to the other, it remains on the same side for several events. We interpret this pattern as a transition between the alternating two-event pattern and the periodic one-sided-event pattern, due to the reduction of fault area with the same critical nucleation patch. Unlike this run, the other runs with dipping fault geometry exhibit one-sided pattern similar to the run in section 3.2, with preferred nucleation location on the left hand side of the fault and unilateral rupture directivity from left to right. Seismic slip in each event is distributed uniformly over the VW zone but with increasing magnitude for decreasing dip angle, which is consistent with the average seismic slip $\bar{\delta}_{seis}$ reported in Table 3. 2. As a result, few events are shown in a fixed range of cumulative fault slip for a model with shallower dip angle. Outside the VW zone, fault slip is accommodated by aseismic creep between

dynamic events, which also increases as dip angle decreases to keep up with the seismic slip and conforms to our discussion about a roughly constant seismic coupling coefficient.

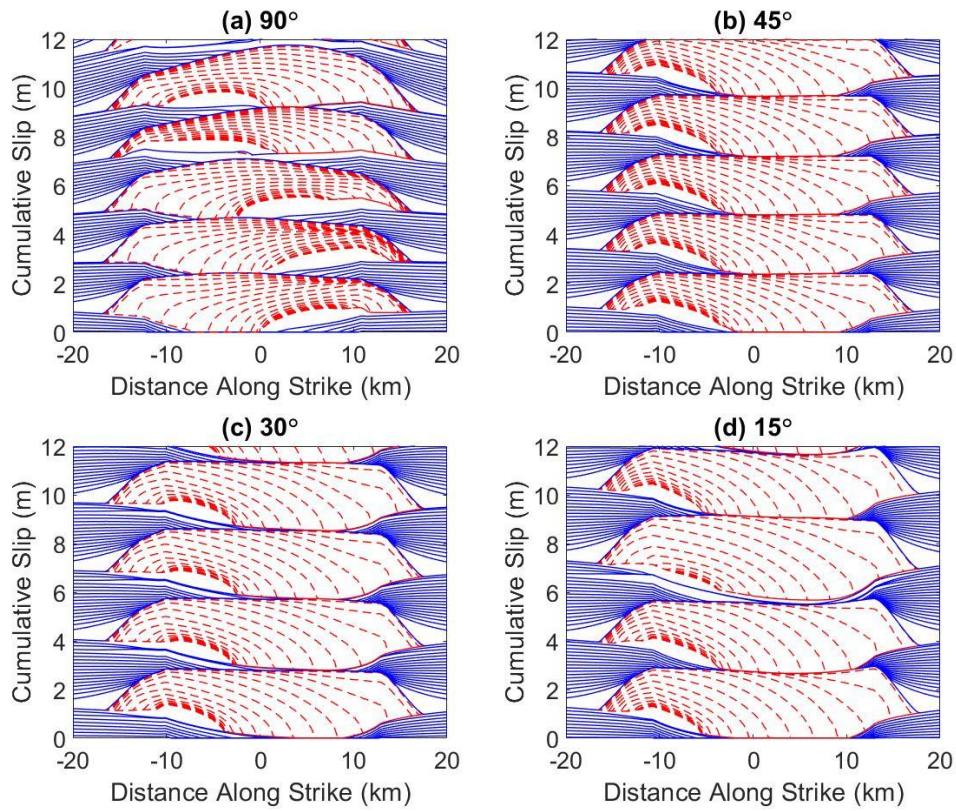


Figure 3. 9 Cumulative slip history of the along-strike profile at $x_d = 7 \text{ km}$ on the thrust faults with (a) 90° , (b) 45° , (c) 30° and (d) 15° dip angles. Solid curves denote slow aseismic slip at an interval of five years. Dashed curves denote fast seismic slip at an interval of one second. The origin of the slip history is set to the moment in the middle of the interseismic period between the second and the third event. Five successive events are shown in (a) and (b), four are shown in (c) and (d).

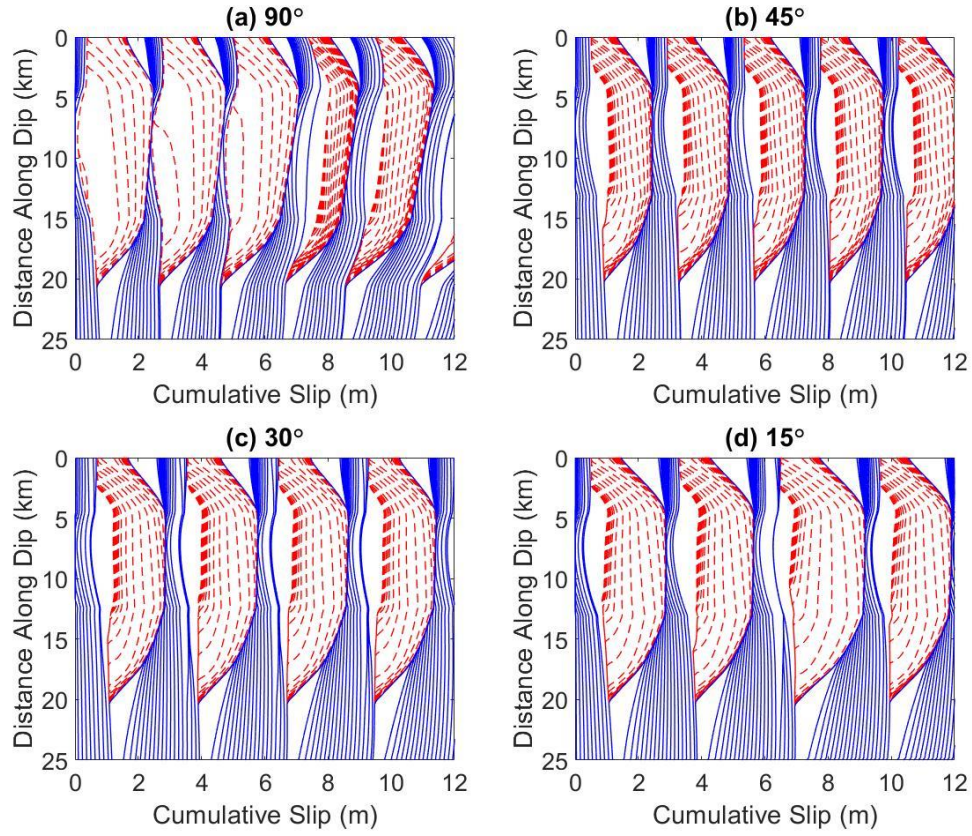


Figure 3. 10 Cumulative slip history of the along-dip profile at $x_s = -8 \text{ km}$ on the thrust faults with (a) 90° , (b) 45° , (c) 30° and (d) 15° dip angles. Solid curves denote slow aseismic slip at an interval of five years. Dashed curves denote fast seismic slip at an interval of one second. Five successive events are shown in (a) and (b) and four are shown in (c) and (d).

Along-dip profiles of cumulative fault slip show details of earthquake cycle behavior in another dimension (Figure 3. 10). We select the profile at $x_s = -8 \text{ km}$ passing through the common nucleation location for most events. However, note that the first three events in Figure 3. 10a nucleate on the other side of the VW zone and the seismic slip

contours in the figure only shows the arrival of the rupture front. For the other events, it can be seen that the along-dip dimension of the nucleation patches is comparable to the VW zone. Nonetheless, these patches can develop into dynamic ruptures that spread over the whole VW area. In all models, dynamic rupture can reach the free surface, although the seismic slip tapers toward the free surface due to the near-surface steady state velocity strengthening property. The VS area near free surface experiences significant amount of afterslip (the blank area after seismic slip contour). For the three non-vertical dipping faults, seismic slip within the VW zone is nearly uniform along dip. However, the vertical dip-slip fault possesses relatively larger seismic slip near the updip edge of the VW zone than the downdip edge, which may be a consequence of the excessively large critical nucleation patch compared to the size of the VW zone. Without sufficient fault area left to develop its size through expansion, the dynamic rupture is soon confined by the surrounding VS zone and imprints relatively strong seismic slip at the updip VW edge and relatively weak slip at the other edges (Figure 3. 9a and Figure 3. 10a). Such spatial variation of final seismic slip cannot be relaxed during interseismic phase and accumulates after multiple cycles.

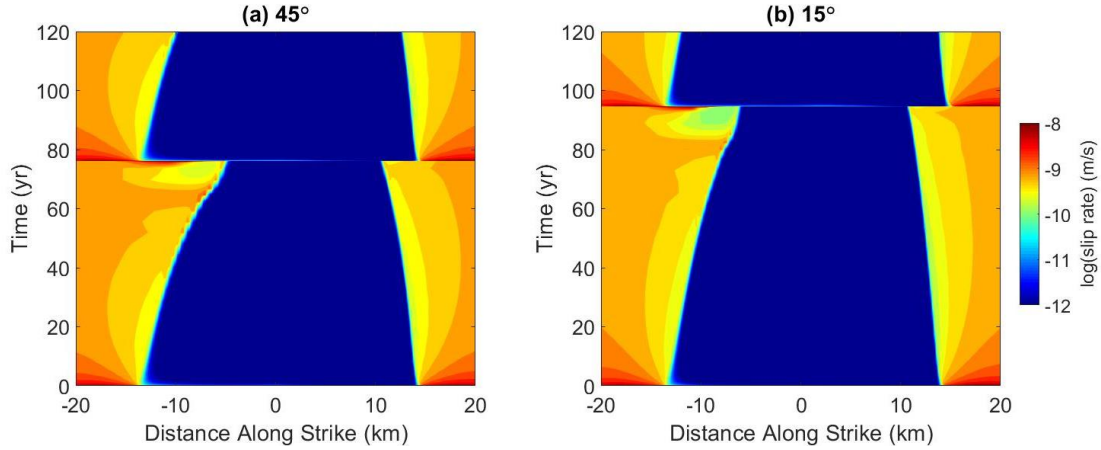


Figure 3. 11 Spatiotemporal evolution of interseismic slip rate along the horizontal line at $x_d = 7 \text{ km}$ on the thrust faults with (a) 45° and (b) 15° dip angles in 120 years after the fifth event. The color scale for slip rate ranges from 10^{-12} to 10^{-8} m/s to emphasize interseismic features. The time origin is reset to the end of the coseismic phase of the fifth event where the following postseismic phase begins. The sixth event occurs in year 76 in (a) and in year 94 in (b).

Comparison of the spatiotemporal evolution of interseismic slip rate of two selected models with dip angles of 45° and 15° (Figure 3. 11) shows that the elongated interseismic period for the shallower dipping fault is a consequence of the relatively slow inward propagation speed of the locked-to-creeping transition front, especially the front on the preferred left side of the fault, although both models are loaded by the same magnitude of slip rate in the shear direction. In both models, when afterslip vanishes, the transition fronts on both sides slowly propagate inward, with increasing slip rate trailing behind. Comparatively, transition front on one side propagates faster, and the trailing slip rate on that side also grows faster, leading to an aseismic transient event that decelerates local slip. This decelerated area eventually develops into a nucleation patch followed by

the dynamic event. All models in this study show similar behavior in the interseismic phase, except that different models evolve at different speed and that sometimes the dominant side may switch to the other side and nucleation location alters accordingly.

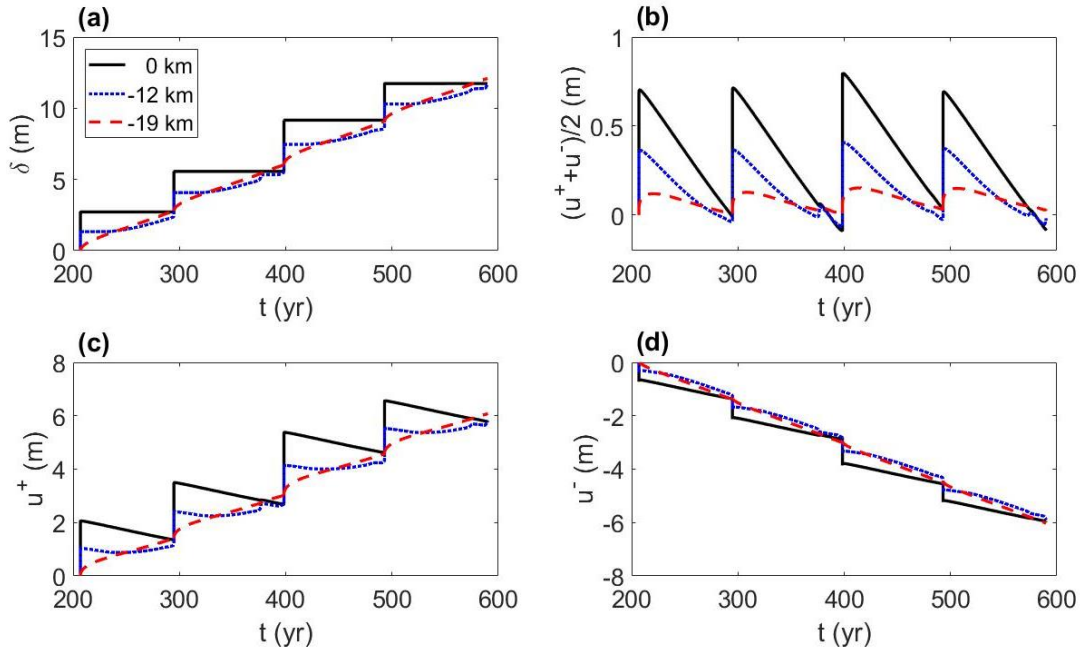


Figure 3. 12 Particle motion histories of the sliding pairs at $x_d = 7 \text{ km}$ and different strike location $x_s = 0 \text{ km}$ (black solid), -12 km (blue dotted) and -19 km (red dashed) on the 15° dipping thrust fault, including (a) cumulative slip, (b) cumulative mean particle displacement, (c) cumulative particle displacement on the hanging wall, and (d) cumulative particle displacement on the foot wall. Quantities are measured along updip direction and particle motions are in opposite directions between the hanging wall and the footwall. The time ranges from the beginning of the third event to the beginning of the seventh event, in which four cycles are included. Cumulative motion starts with zero at the beginning of the time range.

We also examine the particle motions in details for the dipping fault geometry. In Figure 3. 12, particle motion histories of the sliding pairs at different representative locations of the 15° dipping thrust fault are shown. In the seismogenic zone ($x_s = 0$ km), the pair of on-fault points exhibits a staircase stick-slip pattern, while in the stable creep zone ($x_s = -19$ km), the on-fault particles slide steadily relative to each other over multiple cycles. The particle pair at $x_s = -12$ km, which are close to the edge of the VW zone, show mixed behavior. They experience fast slip in the coseismic phase and stick with each other for a while after the dynamic event, but afterwards they switch to steady sliding, similar to the particles in the creep zone, until the next event occurs. The histories of individual particle displacement u^+ and u^- on the hanging wall and the foot wall, respectively, are illustrated in Figure 3. 12c and d. The asymmetric fault geometry causes considerable difference in displacement pattern between u^+ and u^- at $x_s = 0$ km, but little difference at $x_s = -19$ km. Coseismic displacement at $x_s = 0$ km is much greater on the hanging wall than on the footwall, which is one of the most prominent features of thrust fault rupture that has been observed in previous studies (*Oglesby et al.*, 1998; *Oglesby et al.*, 2000). Between the seismic events, however, the particle pair move together in the same direction. The particle on the hanging wall, which has moved a larger distance in the updip direction during the seismic event, reverses its motion to downdip in the interseismic phase. In contrast, the particle on the footwall, which has less coseismic displacement, continues its motion to downdip along with the hanging wall particle in the interseismic phase. Similar to what we observed in the cumulative slip comparison, the particle pair at $x_s = -12$ km exhibits mixed behavior between those at $x_s = 0$ km and

$x_s = -19$ km. The complex difference can be more clearly interpreted by looking at the mean displacement of the particle pair in Figure 3. 12b. The asymmetry of the coseismic displacement at $x_s = 0$ leads to significant offset of the center of the pair from its original position, which is about 0.7 m in this case. During the interseismic phase, their center gradually retrograde to its original position at a nearly constant rate of about 7 mm/yr. Comparatively, the pair at $x_s = -12$ km has half central offset, and the pair at $x_s = -19$ km has the least central offset close to zero. The interseismic retrogradation helps the pairs that has asymmetric displacements in the coseismic phase keep pace with the pairs in the far field whose particles slide relatively in a symmetric manner. This phenomenon is the most significant for the shallowest dipping fault geometry in our study due to the fact that the coseismic asymmetry in particle displacement is the greatest for the shallowest dipping fault. As the dip angle increases, the coseismic central offset in the rupture area decreases accordingly. For the vertical fault geometry, the symmetric displacement pattern on both sides of the fault leads to no offset of the pair center, and thus no retrogradation during the interseismic phase.

3.5 Discussion

The new earthquake simulator developed in this study successfully reproduces earthquake cycles on both vertical and thrust faults. In these numerical experiments, we observe different faulting patterns on different fault geometries. For comparison, we carry out an additional experiment on the vertical strike-slip fault with large fault area Ω_1 but

with fault slip in dip direction. Figure 3. 13 compares the difference in the cumulative slip history of this dip-slip run and the strike-slip run in verification section. In the strike-slip run, dynamic rupture nucleates near the center of the VW zone and propagates bilaterally, but the exact nucleation location alternates laterally around the center over time. In the dip-slip run, dynamic rupture always nucleates from the preferred leftmost side of the VW zone and propagates unilaterally toward the right side, without any alteration of the nucleation location. Both faulting patterns are seen in previous earthquake cycle studies (*Lapusta and Liu, 2009; Erickson and Day, 2016*), with various characteristic slip distance L that leads to different critical nucleation patch size h^* according to expression (3.24). The larger L , which results in larger h^* compared to the seismogenic width W , generates earthquake cycles with the periodic two-event pattern similar to the one observed in our strike-slip run. The smaller L , on the other hand, corresponds to smaller h^* compared to the same W and produces periodic earthquake cycle similar to the one observed in our dip-slip run. By such comparison, the difference in faulting patterns we observed in our models with different slip directions is likely to stem from the different consequent h^* with respect to different slip directions. The crucial parameter for this argument is μ^* in equation (3.24), which is μ for mode III slip and $\mu/(1 - \nu)$ for mode II slip. Given $\nu = 0.25$ which is generally applied for earth material, h_{III}^* is predicted to be 1.33 times smaller than h_{II}^* . Rotating slip direction from strike to dip results in mode III rupture propagation in the strike direction and thus shorter nucleation patch size in this direction. Reduction in nucleation patch size gives more room in the strike direction for dynamic rupture to grow and propagate.

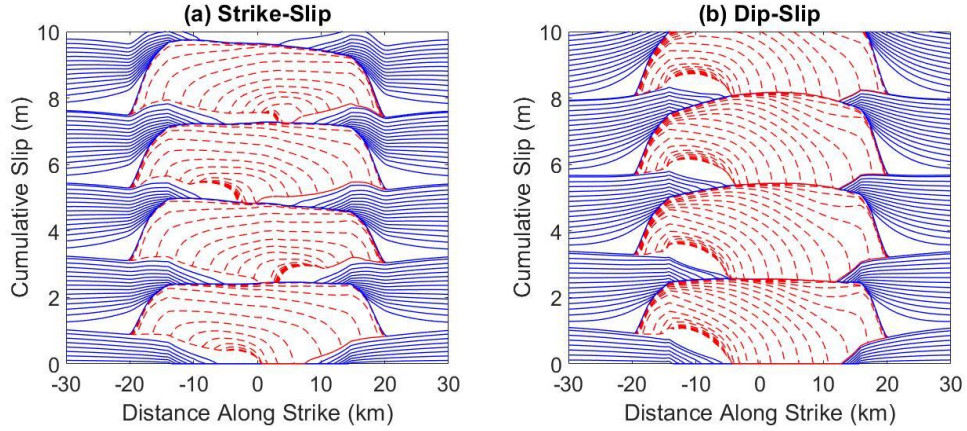


Figure 3. 13 Cumulative slip history of the along-strike profile at $x_d = 10$ km on the vertical (a) strike-slip and (b) dip-slip faults. Solid curves denote slow aseismic slip at an interval of five years. Dashed curves denote fast seismic slip at an interval of one second. The origin of the slip history is set to the moment in the middle of the interseismic period between the second and the third event. Both plots show the cumulative slip history of four subsequent cycles.

Figure 3. 14 shows stress evolution in the quasi-static processes before and after the fifth event. It clearly shows that the residual stress in the strike-slip run is more or less around 28 MPa, but the residual stress in the dip-slip run has notable spatial variation, with 28 MPa on the left and as low as 26 MPa on the right. The residual stress appears to be lower as the rupture propagates further from its nucleation origin. The low residual stress region acts as an anti-asperity that significantly inhibits the inward propagation of the locked zone edge on the right. The side with longer propagation distance of the locked zone edge has a larger area being accelerated and becomes dominant in rupture nucleation. The anti-asperity effect is also true for the strike-slip case, but to a much less extent, as we can observe in Figure 3. 14a that the residual stress from the fourth event is slightly lower

on the left and higher on the right, which leads to shorter propagation distance on the left than on the right. Neither side is dominant, but the side with slightly longer propagation distance of the locked zone edge initiates an aseismic transient (as observed in Figure 3. 6) that circulates around the locked zone and reaches the opposite side of the locked zone. The aseismic fronts join together and lead to nucleation on that opposite side, resulting in alteration of the nucleation location in the earthquake sequence. In this study, we impose an artificial nucleation patch slightly off the center toward the left before the first cycle, which leads to longer dynamic rupture propagation distance, lower residual stress and slower propagation speed of the locked zone edge on the right. As a result, nucleation on the dip-slip faults, including the vertical fault and the thrust faults, prefers the left side of the VW zone.

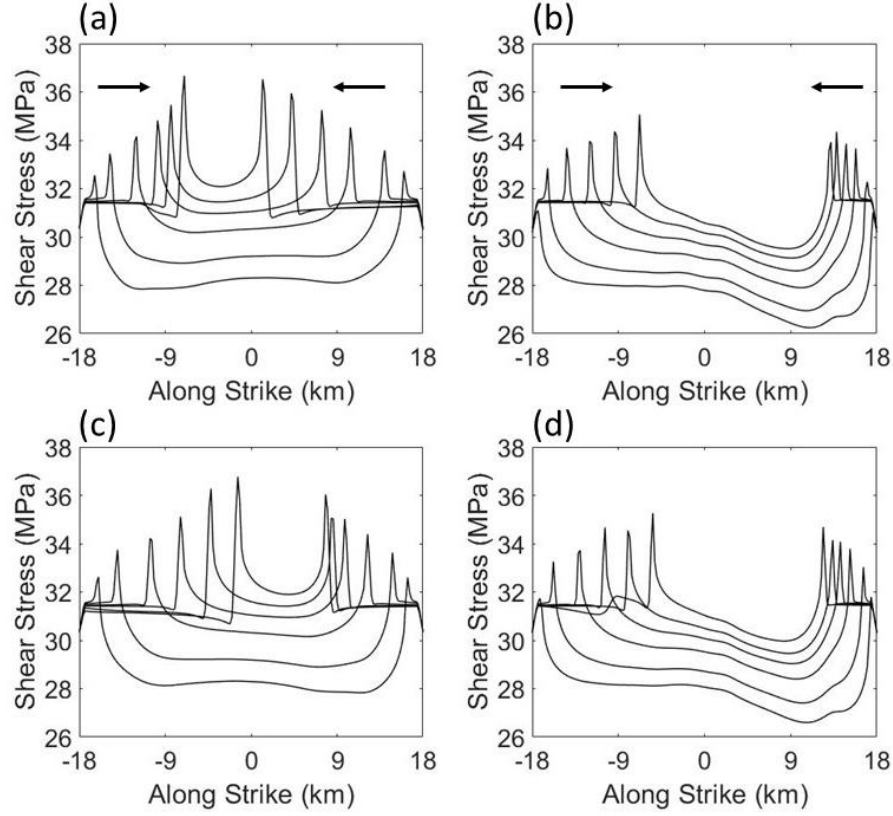


Figure 3. 14 Interseismic evolution of the along-strike shear stress profiles at $x_d = 10 \text{ km}$ in the VW zone of the vertical (a and c) strike-slip and (b and d) dip-slip faults. (a and b) show the interseismic period before the fifth event, and (c and d) show the period before the sixth event. Black arrows denote the propagation direction of the inward propagating edge of the locked zone where shear stress reaches a local peak value. Note that the curves associated with the stress peaks at the outermost of the VW zone are at early stage of the interseismic period and show residual stress level of the preceding dynamic event, while the curves associated with the peaks at the innermost of the VW zone are at late stage and about to trigger nucleation.

The empirical scaling relation for various dip angles observed in the present work is different from either the empirical scaling relation $T_r \propto M_0^{0.17}$ observed from repeating small earthquakes (Nadeau and Johnson, 1998; Chen *et al.*, 2007), or the theoretical

scaling relation $T_r \propto M_0^{1/3}$ derived from an ideal circular crack model (*Beeler et al.*, 2001) assuming that static stress drop and loading rate have no dependence on M_0 . However, the results of the 90° dipping fault model lie around the fitted line of observational data, which implies its consistency with natural repeating earthquakes and other simulation results of vertical faults, although vertical dip-slip faults are seldom seen in nature. Also, the effect of the dip angle on the variation of both T_r and M_0 is limited to a finite range due to the fact that $\sin \phi$ can only vary from 0 to 1. Therefore, while the scaling relation presented by previous studies describes universal features of repeating earthquakes of a wide range of sizes, especially for the earthquakes on vertical faults, the scaling relation we obtained in this work may serve as a complementary rule that describes how repeating earthquakes on a fault system with given fault properties, geologic conditions and tectonic loading rate may scale with the dipping fault geometry. Due to the relatively large exponent in the scaling relation, absolute value of the variation of the recurrence interval may be notably large for large events, such as the Mw 7 event sequences in our study associated with over 40 years difference between the vertical dip-slip fault and the 15° thrust fault, which may be not negligible for earthquake hazard analysis.

The interseismic retrogradation phenomenon observed in our study is a consequence of material elasticity and boundary configuration. In dipping fault models, the time-dependent tectonic loading displacement imposed on the model boundaries is evenly distributed to either side of the relatively sliding blocks, and therefore the boundary condition enforces such distribution of particle motion across the fault throughout the model. When seismic motion temporally breaks the symmetry in particle motions across

the fault surface in the rupture area due to the dipping fault geometry, the model boundary would respond quasi-statically and eliminate the resultant asymmetry through the elastic medium. We suspect that other types of boundary conditions of tectonic loading for thrust faults, such as fixing the hanging wall and moving the footwall (e.g. *Govers et al.*, 2017), may lead to different interseismic evolution patterns of the on-fault pairs. Then the question will be what boundary conditions are more realistic, which may be a question for future studies.

The thrust models in this initial study are relatively simple in comparison to realistic situations, such as earthquake cycles on subduction zones. For example, nucleation in our dipping fault models prefers to occur on the left side and close to the updip edge of the VW zone, which is similar to the strike-slip fault model but may not be consistent with realistic situations in which megathrust earthquakes tend to nucleate near the bottom part of the seismogenic zone. One possible reason is that the distribution of the effective normal stress may increase with depth, which could lead to a smaller nucleation patch at depth and favors nucleation from the bottom. Another possibility is that the lateral VS zone in the current model may act as a source of loading to the system from the lateral sides, which may not be true in subduction zones with a long dimension of locked zones along strike compared to their dimension along dip. Further efforts are needed to explore these variations in the models in the future.

3.6 Conclusions

Earthquake cycle simulations provide an important means to explore faulting behavior and understand earthquake characteristics on large-scale fault systems. In this work, we present a new dynamic earthquake simulator that is developed based on a three-dimensional dynamic FEM code EQdyna, which has been successfully used for dynamic rupture simulations in previous studies. Using the ADR technique, the dynamic code EQdyna finds the solution to a static problem by simulating the pseudo-dynamic iteration process from an initially unbalanced state to a final equilibrium state. This static method is then incorporated into the quasi-static simulation of the relatively slow process between dynamic events. The static method finds the equilibrium state at each moment while the whole model evolves over time under the influence of the rate- and state-dependent friction law and the far-field tectonic loading. Combining the dynamic code EQdyna and the static method that is based on EQdyna and the ADR technique, we successfully perform full earthquake cycle simulations that can capture the complete gamut of faulting behavior on complex fault systems.

We employ the developed methodology in this study for numerical investigations of earthquake cycle behavior on vertical and thrust faults. Numerical simulation on a vertical strike-slip fault verifies the dynamic earthquake simulator. We then examine the thrust faults with various dip angles to study the effect of dipping fault geometry on faulting behavior and have found linear scaling relations of recurrence time and seismic moment with respect to the sinusoidal function of the dip angle. Thrust faults tend to produce earthquake cycles with elongated recurrence times and increased released seismic

energy. Moreover, we confirm that the particle pair across fault surface experience asymmetric displacement between the hanging wall and the footwall during seismic rupture, which results in offset of the pair center. This coseismic offset can be gradually recovered in the interseismic phase until the next event occurs.

CHAPTER IV

THREE-DIMENSIONAL MODELING OF MEGATHRUST EARTHQUAKES ALONG THE JAPAN TRENCH SUBDUCTION ZONE

4.1 Introduction

The northeast coast of Japan was severely struck by the M9 Tohoku-Oki earthquake in the Japan Trench subduction zone in 2011. According to some paleoseismic studies, this unexpectedly large event is likely to be part of an irregular earthquake recurrence pattern in the area. The tsunami deposits on the Sendai plain were found to be related to the historical Jogan earthquake of AD 869 (*Minoura et al.*, 2001; *Sawai et al.*, 2012; *Sugawara et al.*, 2013), which was estimated to be M8.6 (*Namegaya and Satake*, 2014). In addition, a sparsely documented tsunami along with turbidite evidence may collectively indicate another earthquake of similar size in AD 1454 (*Sawai et al.*, 2015; *Ikehara et al.*, 2016; *Ikehara et al.*, 2017; *Usami et al.*, 2018). These paleoseismic studies reveal a possible supercycle of ~700 years for megathrust earthquakes on top of large repeating earthquakes (*Satake*, 2015). However, in the history before the 2011 Tohoku event, many moment magnitude M7~8 earthquakes had occurred along the Japan Trench subduction zone. These earthquakes include the 1968 M8.2 earthquake along the Tokachi section, the 1896 M8.5, 1901 M7.4, 1931 M7.6, 1933 M7.6 earthquakes along the Sanriku section, the 1897 M7.4, 1936 M7.4, 1978 M7.4, 2005 M7.2 earthquake along the Miyagi section, and the 1938 M7.4, 1938 M7.7, 1938 M7.8 earthquakes along the Fukushima section (e.g., *Yamanaka and Kikuchi*, 2004; *Hashimoto et al.*, 2009; *Simons et al.*, 2011).

These M7~8 historical earthquakes did not occur within the large slip area of the 2011 event. Seismic activity along this subduction zone has been suggested to be dominated by M7+ earthquakes recurring every 30 to 40 years. These observations lead to an important question: what geological and physical features along the subduction zone control generation of earthquakes of various sizes, and how these features operate over multiple earthquake cycles to control their generation. Understanding complexities in earthquake recurrence is essential for seismic hazard analysis, particularly subduction zone areas where the largest earthquakes in the world occur.

Some earthquake source mechanisms were proposed to reproduce and understand long-term and coseismic observations of the supercycle. For example, *Hori and Miyazaki* (2011) modeled the complex earthquake cycle behaviors using large and small fracture energy areas for M9 and M7~8 events, respectively. *Shibazaki et al.* (2011) performed quasi-dynamic earthquake cycle simulation and assumed heterogeneous frictional properties over the fault surface by setting several asperities with velocity weakening property at low slip rate on the fault surface, which exhibits velocity strengthening property at low slip rate but strong velocity weakening property at high slip rate. While rupture on these asperities occurs at intervals of several tens of years, megathrust events over a much larger area including both velocity weakening and velocity strengthening zones occur at a much longer interval of hundreds of years. Similar idea was employed by *Noda and Lapusta* (2013) who hypothesized that stable creeping fault segments may experience substantial dynamic weakening at seismic slip rate and conducted earthquake simulation with fully dynamic description of the coseismic features.

These simulations are limited to investigating effects of hypothesized heterogeneous frictional properties or mechanisms on the fault interface in controlling the earthquake cycle behavior. However, field observations identify volumetric geologic conditions such as complex fault geometry and structural heterogeneity in the large slip area of the 2011 event (e.g., *Ito et al.*, 2005; *Miura et al.*, 2005; *Zhao et al.*, 2011; *Yamamoto et al.*, 2014; *Bassett et al.*, 2016; *Liu and Zhao*, 2018). Geometrical effects have long been considered as one of the major factors that affect long-term faulting behavior and short-term rupture process. In the subduction area, topographic reliefs on the seafloor, such as seamounts and plateaus, can be dragged into the fault interface along with the subducting oceanic plate and generate large-scale geometrical complexities. *Duan* (2012) carries out 3D modeling of spontaneous rupture with a high stress patch, mimicking a seamount of $70 \times 23 \text{ km}^2$ updip of the hypocenter of the 2011 event. The patch with lower pore fluid pressure and high strength stalls initial rupture expansion until its failure occurs, leading to massive rupture over the entire fault surface. *Yang et al.* (2013) investigates the explicit geometrical effects of a subducted seamount with elevated normal stress as a barrier on stopping megathrust earthquakes. They demonstrate that strength of the seamount in resisting dynamic rupture depends on the level of increased normal stress, the seamount height-to-width ratio and the seamount-to-nucleation distance. *Yang et al.* (2012) carry out 2D numerical simulations of long-term earthquake cycles on thrust interface with elevated normal stress representing a subducted seamount and demonstrate that the subducted seamount can either act as a high strength barrier in stopping rupture

propagation and reducing earthquake size or act as an asperity with large coseismic slip when it fails to resist the rupture.

Variable fault zone bulk properties are also crucial in affecting both long-term and short-term faulting behavior according to previous studies (e.g., *Kaneko et al.*, 2011; *Erickson and Dunham*, 2014; *Erickson and Day*, 2016). For example, *Kaneko et al.* (2011) carry out 2D long-term fault slip simulation using spectral-element method to investigate the effect of low-rigidity layers on earthquake cycle behavior. They find that compared to homogeneous fault zone, heterogeneous media causes reduction in earthquake nucleation size, amplification of coseismic slip rate, elongated recurrence time, and decrease in aseismic slip. *Erickson and Dunham* (2014) conduct 2D finite difference simulation of earthquake cycles on faults cutting through heterogeneous media with compliant sedimentary basin structure at shallow depth. Their results show that one or several events are confined below the basin, followed by large rupture that breaks through the basin up to the surface. Alternating subsurface and surface-rupturing events are possibly a scenario for the various earthquake sizes in the subduction zone with the accretionary prism.

In this study, we employ our newly developed earthquake simulator based on a fully dynamic finite element method (FEM) to conduct earthquake cycle modeling in a volumetric medium with realistic heterogeneous structure and fault geometrical complexity, respectively. The advanced earthquake simulator is able to capture full details of long-term fault slip (both quasi-static and dynamic) on a subduction fault plane governed by the laboratory derived rate-and-state friction law, with major characteristics including stable sliding during the interseismic phase, smooth but rapid growth of slip

velocity during the nucleation phase, spontaneous rupture propagation during the coseismic phase, and gradual decay of slip velocity during the post-seismic phase. Using the FEM-based earthquake simulator, we aim to reproduce a possible scenario for the supercycles of megathrust earthquakes along the Japan Trench subduction zone and investigate the relation between and earthquake cycles of different sizes and complex fault geometry and bulk properties.

4.2 Model Setup

The FEM dynamic code EQdyna is naturally suitable for volumetric modeling with complex geometrical fault discontinuities and bulk properties. The earthquake cycle simulator developed based on EQdyna inherits this advantage and is ready for simulations on structural heterogeneity and complex fault systems. In EQdyna, the space domain is discretized by hexahedral elements, with degenerated elements (wedge or tetrahedral elements) for geometrical complexities. The code uses the traction-at-split-node (TSN) method to characterize the discontinuity of the fault boundary (*Andrews, 1999; Day et al., 2005; Duan, 2010*). Specifically, we represent the shallow-dipping subduction fault geometry using the degeneration technique (*Duan, 2010; Duan, 2012; Luo and Duan, 2018*), which splits a hexahedral element into two wedges to create dipping fault discontinuity. In this study, we construct two individual subduction fault models, one with approximate realistic structural heterogeneity but planar fault geometry, the other with

nonplanar fault geometry but homogenous bulk property, to investigate independently the effects of these geologic conditions on earthquake cycle behavior.

4.2.1 Structural Heterogeneity

For the heterogeneous model, we construct a subduction fault plane embedded in a 3D heterogeneous elastic medium. The fault surface is 450 km along strike and 240 km along dip, dipping at $\phi = 15^\circ$. As shown in Figure 4. 1, the fault plane dips in the y-z plane and separates the whole domain into hanging wall and footwall blocks. The oceanic crust and its underlying mantle are simplified as a homogeneous region (blue) in the footwall block. In the hanging wall block, the continental crust consists of the upper crust (red and yellow) from free surface to 20 km deep and the lower crust (purple and green) from 20 km to 40 km deep, lying on top of the mantle (blue) below 40 km deep. In this study, we assume that these lithologic regions differ only in terms of density and elastic properties. No viscoelastic properties are considered in the lower crust and the mantle. Specifically, we construct the 3D velocity structure of the Tohoku forearc in light of the structural heterogeneity model obtained from tomographic inversion of P-wave arrival data by *Liu and Zhao* (2018), which is updated from a general 1D model velocity structure beneath northeast Japan obtained by *Zhao et al.* (1992). In this 1D velocity model, P-wave velocity V_p is 5.99 km/s in the upper crust, 6.67 km/s in the lower crust, and 7.70 km/s in the upper mantle, and S-wave velocity V_s is 3.55 km/s in the upper crust, 3.78 km/s in the lower crust, and 4.34 km/s in the upper mantle. The inversion result by *Liu and Zhao*

(2018) suggests that the crustal lithology above the deeper portion of the subduction zone mainly exhibits high V_p anomaly, while the lithology in the wedge near the trench exhibits high V_p anomaly in the Tohoku earthquake rupture area but low V_p anomaly to the north and south along the trench. Therefore, in the yellow and green regions, we set uniform V_p as 6.23 km/s and 6.94 km/s, respectively, which are 4% higher than the corresponding crustal V_p in the 1D velocity model. We also set varying V_p values along strike direction (Figure 4. 2a) in the red and purple regions which are within 150 km landward from the trench line. Similar spatial perturbation ratio is applied to the 1D model of V_s in this study. Rock density is mainly 2700 kg/m³ in the crust and 3100 kg/m³ in the mantle. Investigation of residual topographic anomaly and gravity anomaly by *Bassett et al.* (2016) reveals south-to-north change in density in the upper plate near the south bound of the Tohoku earthquake rupture area. Such density contrast is incorporated in the continental crust layers (both upper and lower crust), as shown in Figure 4. 2b.

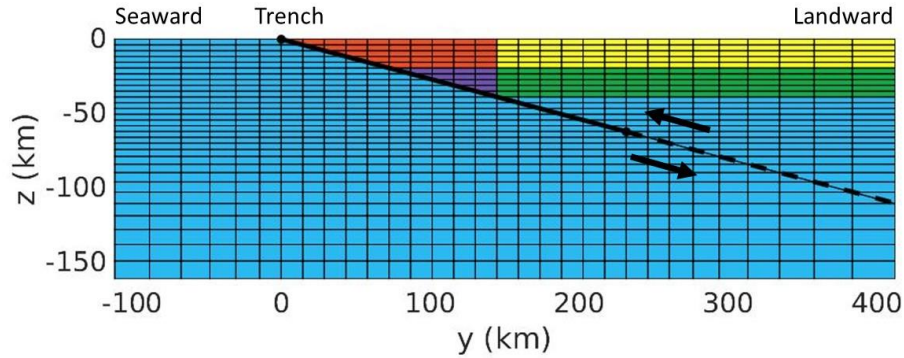


Figure 4. 1 Depth cross-section of the major portion of the finite element mesh for the subduction fault model, including geometry of the fault plane between hanging wall and footwall and layers in the overriding plate. See text for more details of the color-coded structural heterogeneity. Solid black line denotes the fault area of interest in this study, while dashed black line denotes the deep portion of the fault plane that always slides freely at plate convergence rate. Black arrows denote relative plate motions across the fault plane. Element size is 15 km for illustration purpose.

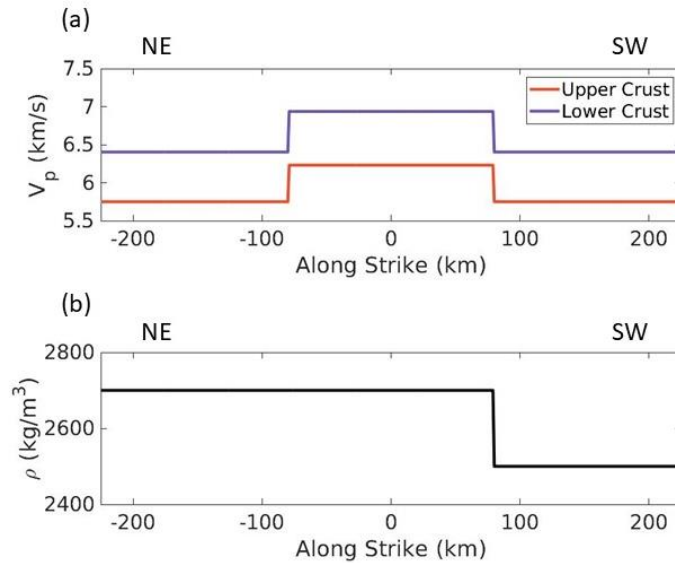


Figure 4. 2 (a) Along-trench P-wave velocity profiles in the upper and lower portions of the continental crust within 150 km from the trench line. (b) Along-trench rock density profile in the continental crust.

4.2.2 Nonplanar Fault Geometry

For the nonplanar fault model, we design a subduction fault interface embedded in homogenous elastic medium ($V_p=6$ km/s, $V_s=3.646$ km/s, $\rho=2670$ kg/m³, as shown in Figure 4. 3a) with an explicit bulging geometry representing a low-height broad-width topographic relief subducted along with the oceanic plate. According to the ~ 0.8 km residual topography change along trench axis obtained from bathymetric measurement of the upper plate (Bassett et al., 2016), we explicitly construct the possible subducted relief in the FEM mesh with 2 km maximum topographic height in a 140 km by 80 km elliptical region on the fault updip of the 2011 hypocenter (~ 0 km along strike, ~ 100 km along dip, as shown in Figure 4. 3b).

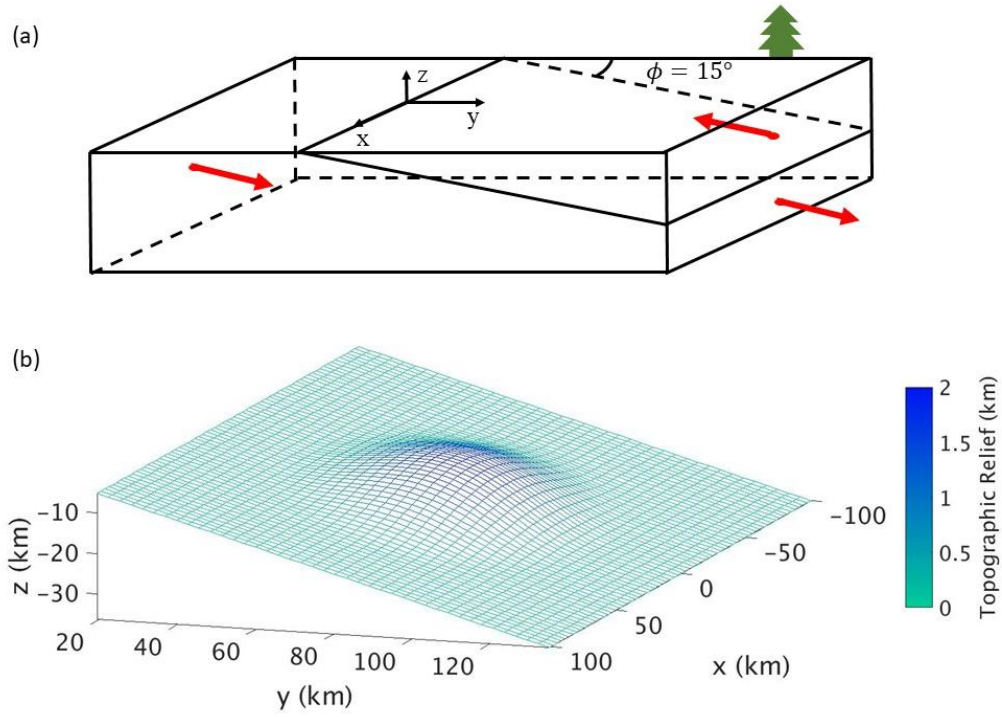


Figure 4.3 (a) A fault plane with 15° dip from the free surface embedded in a hexahedral model domain. The fault plane divides the model domain into two blocks. The red arrows represent the major movement direction of the blocks. (b) FEM mesh of the nonplanar fault surface discretized by square elements. Only the part with the bump geometry is shown. Element size is 3 km for illustration purpose.

4.2.3 Frictional Parameters

In this subduction model, both long-term and short-term fault slips are governed by the laboratory-derived rate- and state-dependent friction (RSF) law (*Dieterich, 1979; Ruina, 1983*), which describes the constitutive relation between frictional stress τ and slip velocity V and state variable θ :

$$\tau = \sigma \left(f_0 + a \ln \frac{V}{V_0} + b \ln \frac{V_0 \theta}{L} \right), \quad (4.1)$$

where σ represents effective normal stress, f_0 is reference friction coefficient for reference sliding velocity V_0 , a and b are parameters for rate dependence and state dependence, respectively, and L is characteristic slip distance. Here the state variable is described by the aging law:

$$\frac{d\theta}{dt} = 1 - \frac{V\theta}{L}. \quad (4.2)$$

The frictional parameters, together with elastic properties of surrounding material, are crucial in determining the sliding pattern of the fault over time. Frictional stability analysis of the RSF law on 1D spring-slider model show that dynamic instability can occur only when the stiffness of the spring K is less than a critical stiffness $K_{crit} = -\sigma(a - b)/L$ (Ruina, 1983; Scholz, 1998). Positive $a - b$, which indicates velocity strengthening (VS) frictional property, implies negative K_{crit} and intrinsically stable sliding. Negative $a - b$, or velocity weakening (VW) frictional property, provides a positive value for K_{crit} and thus allows conditionally unstable sliding. Further analysis (Scholz, 1998) on 2D and 3D models suggest that the static stiffness K is inversely proportional to the length scale of the crack size, which indicates that a slipping region will remain stable sliding until it grows into a sufficiently large size (therefore sufficiently small K) and allows dynamic instability to occur. One practical estimate for this critical size, also called the nucleation patch size, is given as (Chen and Lapusta, 2009; Lapusta and Liu, 2009)

$$h^* = \frac{\pi}{2} \frac{\mu^* b L}{(b - a)^2 \sigma}, \quad (4.3)$$

where μ^* is $\mu/(1 - \nu)$ for mode II and μ for mode III, with μ the shear modulus and ν the Poisson's ratio.

Here we follow *Lapusta and Liu* (2009) to set up typical laboratory-measured frictional properties on the fault. Along-dip and along-strike profiles of $a - b$ are shown in Figure 4. 4. The parameters a and b are uniformly assigned to 0.01 and 0.014, respectively, in the region from -150 km to 150 km along strike and from 30 km to 185.5 km along dip. The difference between a and b is thus uniformly -0.004 in this region, representing the major part of the VW zone on the fault. In the shallower part, $a - b$ increases linearly up to 0.008 at the trench to represent the velocity strengthening property of the abundant sediments near the trench. In the deeper part, $a - b$ also increases linearly to positive values corresponding to the increased temperature in the brittle-ductile transition region and the ductile region at depth. Lateral regions outside the uniform $a - b$ region also has linear transition from VW to VS property to constrain lateral propagating dynamic rupture, which is an artificial setting that does not necessarily represent realistic stopping factors in nature.

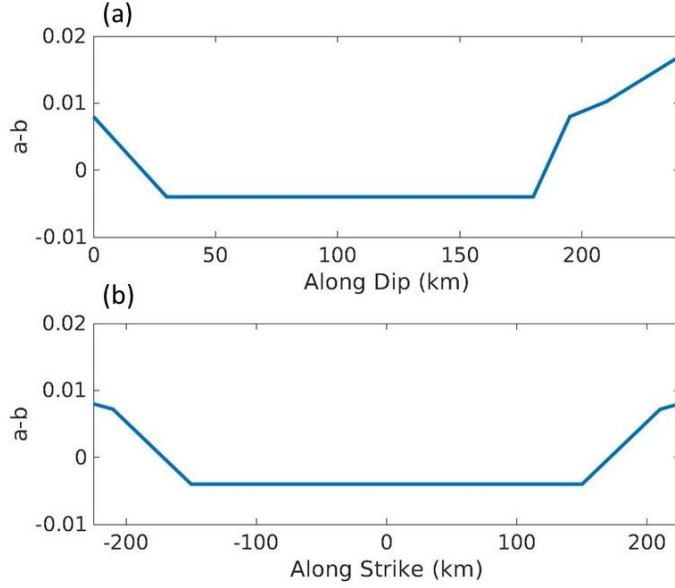


Figure 4. 4 Profiles of frictional parameter $a - b$ along (a) dip and (b) strike directions.

4.2.4 Boundary and Initial Conditions

Our earthquake cycle simulator explicitly characterizes the volume surrounding the fault and thus requires prescribed boundary conditions. In the short-term dynamic rupture process where tectonic loading is negligible, the top surface of the model is traction-free to mimic the ground and the subsurface boundaries are assigned perfectly matched layers (PML) in order to absorb radiated seismic waves. In the long-term quasi-static process where tectonic loading is non-negligible, half of the loading displacement increment $V_{pl}\Delta t$ in a time step Δt is assigned to part of the $y = y_{max}$ boundary that belongs to the hanging wall in the updip direction parallel to the fault surface. The other half of the

loading displacement increment $V_{pl}\Delta t$ in a time step Δt is assigned to the $y = y_{min}$ boundary and part of the $y = y_{max}$ boundary that belongs to the footwall. The along-strike displacement u_x is fixed to zero on the boundaries $x = x_{max}$ and $x = x_{min}$. The top surface and the bottom boundary are both assumed traction-free. Other displacement components on the outer boundaries of the model domain are set to be free.

We assume initial slip velocity $V_{ini} = V_{pl}$ over the fault. Initial effective normal stress is assumed as $\sigma_{ini} = 50$ MPa throughout the fault surface by assuming fluid overpressurization that keeps the difference between lithostatic stress and hydrostatic pore pressure a constant. Initial steady state shear traction τ_{ini} is in the same direction as V_{ini} but with a heterogeneous magnitude determined by $\tau_{ini} = \sigma_{ini}[f_0 + (a - b) \ln(V_{ini}/V_0)]$. In the uniform VW area where $-b = -0.004$, $\tau_{ini} = 31.18$ MPa. Other model parameters are summarized in Table 4. 1.

Table 4. 1 Model Parameter Summary

Parameter	Value
Fault VW zone length L_s	342.9 km
Fault VW zone width W_s	168.6 km
Characteristic slip distance L	0.15 m
Reference slip velocity V_0	10^{-6} m/s
Steady state friction coefficient f_0	0.6
Uniform effective normal stress σ_{ini}	50 MPa
Loading rate V_{pl}	86 mm/yr
Element edge length in x direction Δx	1500 m

Simulations in this study are done in parallel using 400 cores on supercomputer system. The subduction fault model with structural heterogeneity has about 11.4 million elements. It takes about 2 hours of wall-clock time on average to complete each dynamic rupture simulation and 5.8 hours on average to complete each quasi-static simulation. A simulation of six cycles on this model takes about 47 hours in total to complete. The subduction fault model with nonplanar fault geometry has the same model size and element size as the heterogeneous model, therefore it also has about 11.4 million elements in the mesh. It takes about 1.4 hours of wall-clock time on average to complete each dynamic rupture simulation and 6.3 hours on average to complete each quasi-static simulation. Therefore, it takes about 54 hours in total to complete the simulation of seven cycles in a sequence.

4.3 A Subduction Fault Model with Structural Heterogeneity

4.3.1 Earthquake Sequence and Fault Slip

The overall faulting behavior of the earthquake sequence can be examined by the history of maximum slip velocity V_{max} over the fault plane (Figure 4. 5a). Six ~M9 events, during which V_{max} reaches coseismic level (> 1 m/s), are reproduced in a roughly periodic manner with a recurrence interval of ~360 years during the simulation time of 2000 years. Between these giant earthquakes, numerous irregular aseismic transient events emerge, with V_{max} two to three orders of magnitude higher than V_{pl} but yet much less than coseismic slip velocity. These aseismic transients typically emerge after a quiescent period

of 150-200 years that follows the occurrence of a giant earthquake. They appear sequentially with an increasing V_{max} until a peak of $\sim 10^{-6}$ m/s is reached, which is about 100 years before the next giant event occurs. Figure 4. 5b and c show the details of these aseismic transients before the fourth and the sixth events, respectively.

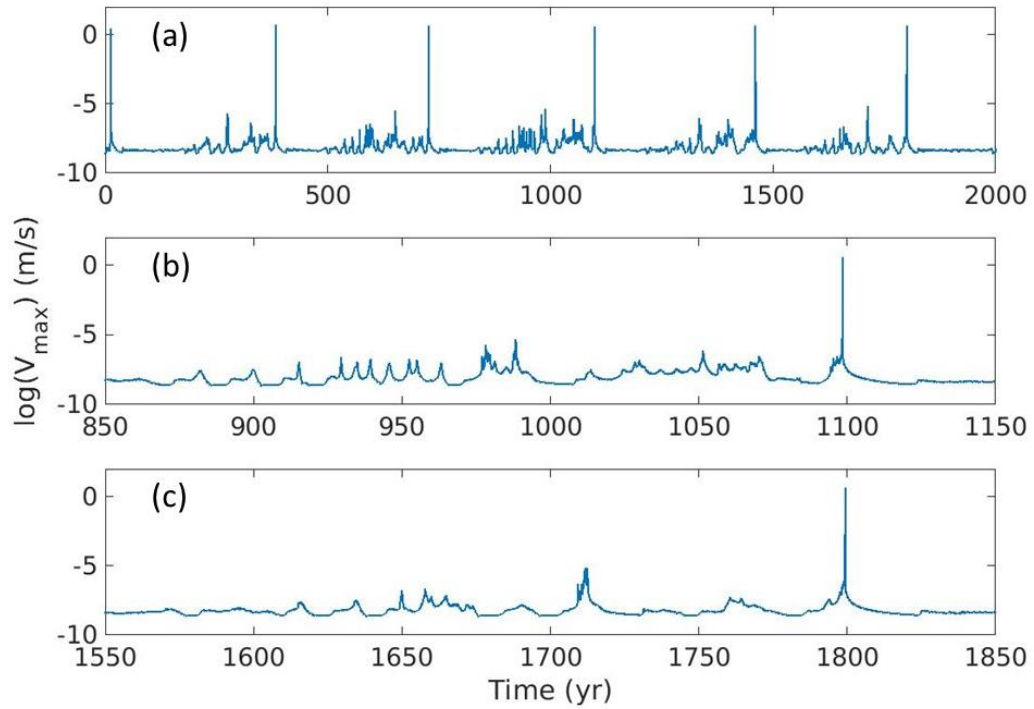


Figure 4. 5 Maximum slip velocity histories in log scale (a) between year 0 and 2000, (b) between year 850 and 1150, and (c) between year 1550 and 1850. A total of six events (large spikes) are shown in (a). The fourth and the sixth events are shown in (b) and (c), respectively.

Cumulative slip profiles at various depths show spatial heterogeneity of long-term slip behavior (Figure 4. 6) on the fault. We examine two along-strike profiles, one at 70 km and the other at 140 km along dip from the trench line. Both profiles pass through the VW zone, but their slip behaviors appear differently. In the shallow profile, there are pure seismic slip in the VW zone and pure aseismic slip near the fault edge. At the transition area between VW and VS area, there is a mix of both seismic slip and aseismic slips. In addition, relatively fast slips occur during the interseismic phase (the wider gaps between blue curves), which corresponds to the aseismic transients between giant earthquakes. In each giant event, seismic slip initiates from the right portion of the VW zone and then propagates toward the left edge of the VW zone. It appears that the final seismic slip in each event is generally greater on the left than on the right. Such difference is accommodated by following aseismic transient slips in the interseismic phase, as we can observe that there are apparently more aseismic transient slips on the right transition edge than on the left transition edge, and the cumulative slip before the next giant event is roughly even across the VW zone. Five earthquakes are shown in a total of 160 m cumulative slip, suggesting an average of 32 m of slip in each earthquake cycle. In the deep profile, similar amount of fault slip occurs in each cycle, but aseismic transient slips at this depth occur through the whole VW zone in an irregular manner in terms of both size and location. They take up more portion of the total slip, which leads to less seismic slip in this area.

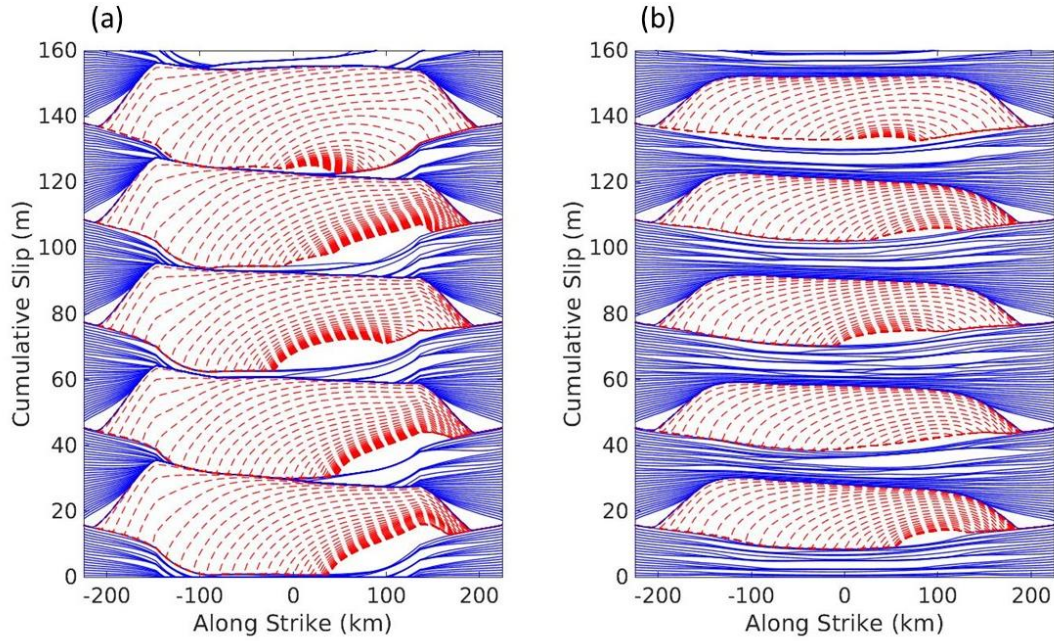


Figure 4. 6 Cumulative slip history of the along-strike profile at (a) 70 km and (b) 140 km along dip from the trench line. Blue solid curves denote slow aseismic slip at an interval of ten years. Red dashed curves denote fast seismic slip at an interval of five seconds. The origin of the slip history is set to the moment in the middle of the interseismic period between the first and the second event in the sequence. Five successive events are shown.

4.3.2 Earthquake Rupture

In this earthquake sequence, dynamic events nucleate predominantly on the right portion of the seismogenic zone after long-term interseismic deformation. Among these events, the sixth one has a similar nucleation location to the 2011 Tohoku earthquake. This dynamic rupture nucleates near the center of the fault zone and then propagates spontaneously on the fault surface. Figure 4. 7 illustrates the snapshots of slip velocity on

the fault to demonstrate the spontaneous rupture propagation process. Starting at the moment when maximum slip velocity in the nucleation zone is greater than 0.3 m/s, the rupture first propagates toward the trench with high slip velocity at the updip rupture front (Figure 4. 7a-c). The updip propagating rupture front penetrates into the shallow velocity strengthening zone and reaches the trench line at 30 s. At 40 s, the downdip propagating rupture front is arrested by the VW bottom edge at depth, causing a stopping phase that propagates updip into the main rupture area. Slip velocity on the lateral sides of the rupture becomes high and the rupture starts to propagate bilaterally. At 60 s, the right front reaches the right edge of the VW zone first and vanishes, also radiating a stopping phase back toward the main rupture area. The left front continues propagating toward the left edge of the velocity weakening zone with enhanced slip velocity. The rupture finally stops when the left front gets arrested at the left edge.

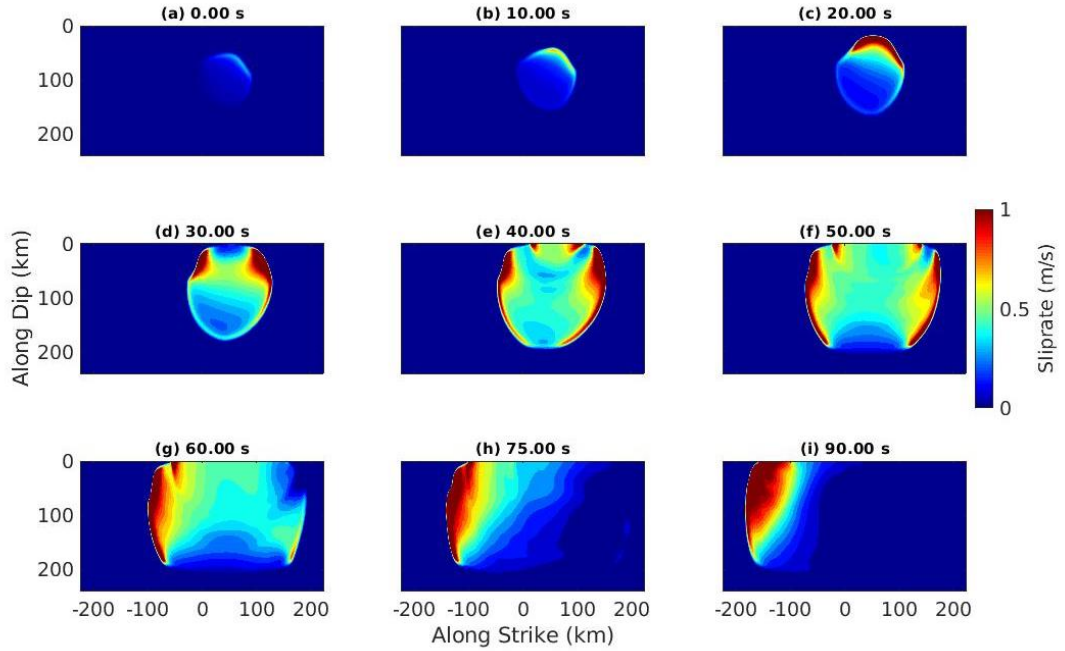


Figure 4. 7 Snapshots of slip velocity on the fault plane for the sixth dynamic event in the earthquake sequence. Corresponding time is shown on each snapshot. For illustration purpose, the onset time is set to the moment when maximum slip velocity in the nucleation zone becomes greater than 0.3 m/s.

Final slip distribution of this giant event (Figure 4. 8a) shows an obvious asperity with large coseismic slip (> 30 m) immediately updip of the nucleation zone of this event. Large coseismic slip region (> 20 m) also extends laterally to the edges of the VW zone and updip to the trench line, but is limited within 100 km in dip direction from the trench line. Coseismic slip decreases significantly in the deep portion of the fault, where aseismic transient slips occupy greater portion of the total fault slip of an earthquake cycle, as illustrated in the cumulative slip profile (Figure 4. 6b). Shear stress drop distribution (Figure 4. 8b) shows correspondingly high stress drop in the asperity area. Linear features

with high stress drop are remnants of the stress concentration fronts that propagate during interseismic phase. The stress drop inside the nucleation zone is nearly zero during the coseismic phase because the stress in this site has been relaxed when nucleation develops. Stress drop near the deep portion of the fault is also relatively low, corresponding to less coseismic slip. A circle of negative stress drop surrounding the VW area exists in the VS area, which is associated with the stress concentration in the cohesive zone of the dynamic rupture that penetrates into the VS zone and will be relaxed by afterslip later in the postseismic phase.

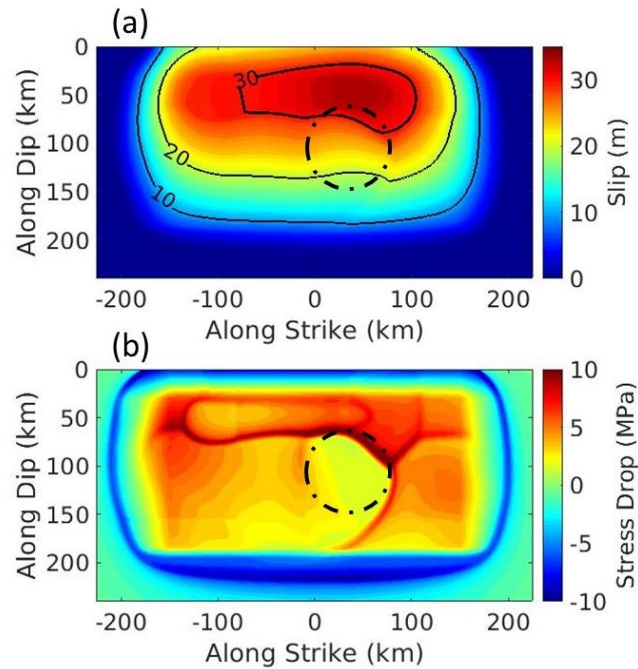


Figure 4. 8 Distributions of (a) final slip and (b) stress drop on the fault plane for the sixth dynamic event in the earthquake sequence. Black dash dotted circles indicate the rough size and location of the nucleation zone.

4.3.3 Aseismic Transients and Earthquake Nucleation

The subduction fault model used in this study reproduces complex interseismic deformation behavior as demonstrated above. We further investigate interseismic fault evolution details by examining the slip velocity snapshots in the interseismic and nucleation phases (Figure 4. 9). These snapshots reveals three major aseismic transients, among which the last one turns into nucleation for the sixth giant earthquake. Figure 4. 9a and b shows the nearly 200 year quiescent period after the fifth giant earthquake, during which the locked zone gradually shrinks under consistent loading, mainly from the bottom part, with barely any active slips over the fault surface. The first aseismic transient is illustrated in Figure 4. 9c-f, which emerges at the bottom right corner of the VW zone where slip has been accelerated and propagates first upward and then leftward along the accelerated area in the VW zone. The second aseismic transient is illustrated in Figure 4. 9g-m, which has similar behavior to the first one, but acts more intensely in terms of slip velocity and affected area. It also joins another small aseismic transient that concurrently emerges at the bottom left corner of the VW zone and amplifies the local slip velocity. In Figure 4. 9n-q, the locked zone is loaded again from the bottom twice, which leads to an aseismic transient on the left portion of the VW zone that eventually develops into a nucleation patch (Figure 4. 9r).

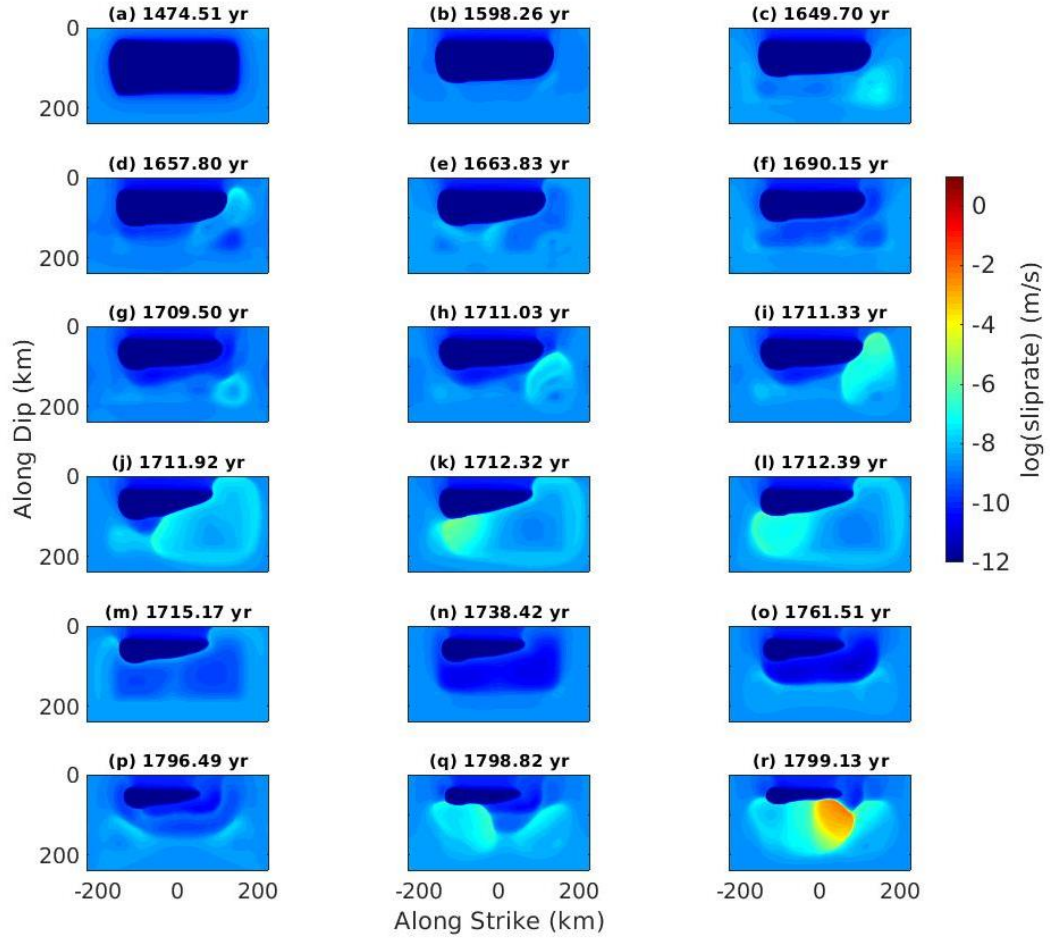


Figure 4. 9 Snapshots of logarithmic sliprate over the fault for the interseismic period before the sixth event.

Space-time diagram of the sliprate evolution at 100 km dip from the trench line shows the propagation of the last aseismic transient within 30 days before the sixth event occurs (Figure 4. 10). In the first 25 days, the aseismic front propagates from 0 km to 20 km at a constant rate of 0.8 km/day. In the last few days, the aseismic front expands rapidly

from a concentrated area at around 20 km into a large region ranging from -20 km to 60 km, forming the nucleation patch with accelerated sliprate. This slip behavior to some extent resembles the sequences of foreshocks that migrates along the trench axis from the epicenter of the M7.3 foreshock in the north to the epicenter of the 2011 Tohoku earthquake in the south. *Kato et al.* (2012) reexamine the Japan Meteorological Agency (JMA) catalog and identify two migrating foreshock sequences, one before and one after the M7.3 foreshock that occurs three days prior to the M9 mainshock. The first sequence starts about 25 days prior to the M9 event. It first migrates at a speed of 2 km/day and later speeds up to 5 km/day, followed by a quiet period of 8 days and then the burst of the M7.3 foreshock. Although our simple model is unable to resolve the realistic complexity of the foreshock seismicity due to the numerical limitation, it reproduces an aseismic front that has similar trending and propagates smoothly at a constant but smaller speed for over 20 days. The second sequence, which occurs immediately after the M7.3 foreshock and roughly fits a parabolic curve for diffusive process (*Ando and Imanishi, 2011*), migrates at an average speed of 10 km/s toward the mainshock epicenter. This sequence may correspond to the rapid expansion of the accelerated area in our modeled result, which also occurs within a few days prior to the sixth event.

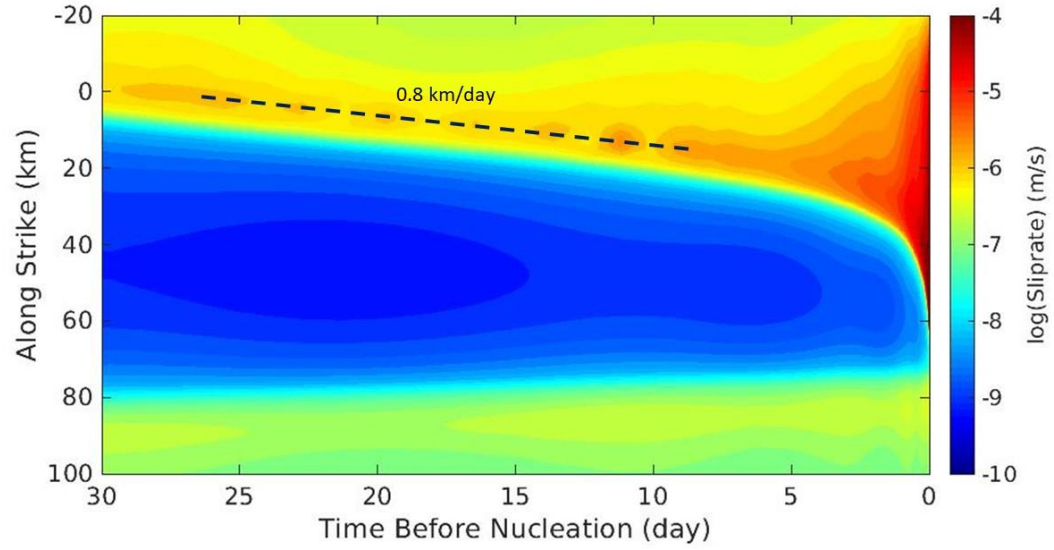


Figure 4. 10 Space-time diagram of sliprate in log scale at 100 km dip from the trench line. The sliprate evolution indicates the north-to-south propagation of the aseismic transient within 30 days before rupture initiation of the sixth event in the modeled earthquake sequence. The black dashed line denotes the front (peak sliprate along strike) that migrates at a constant speed of 0.8 km/day.

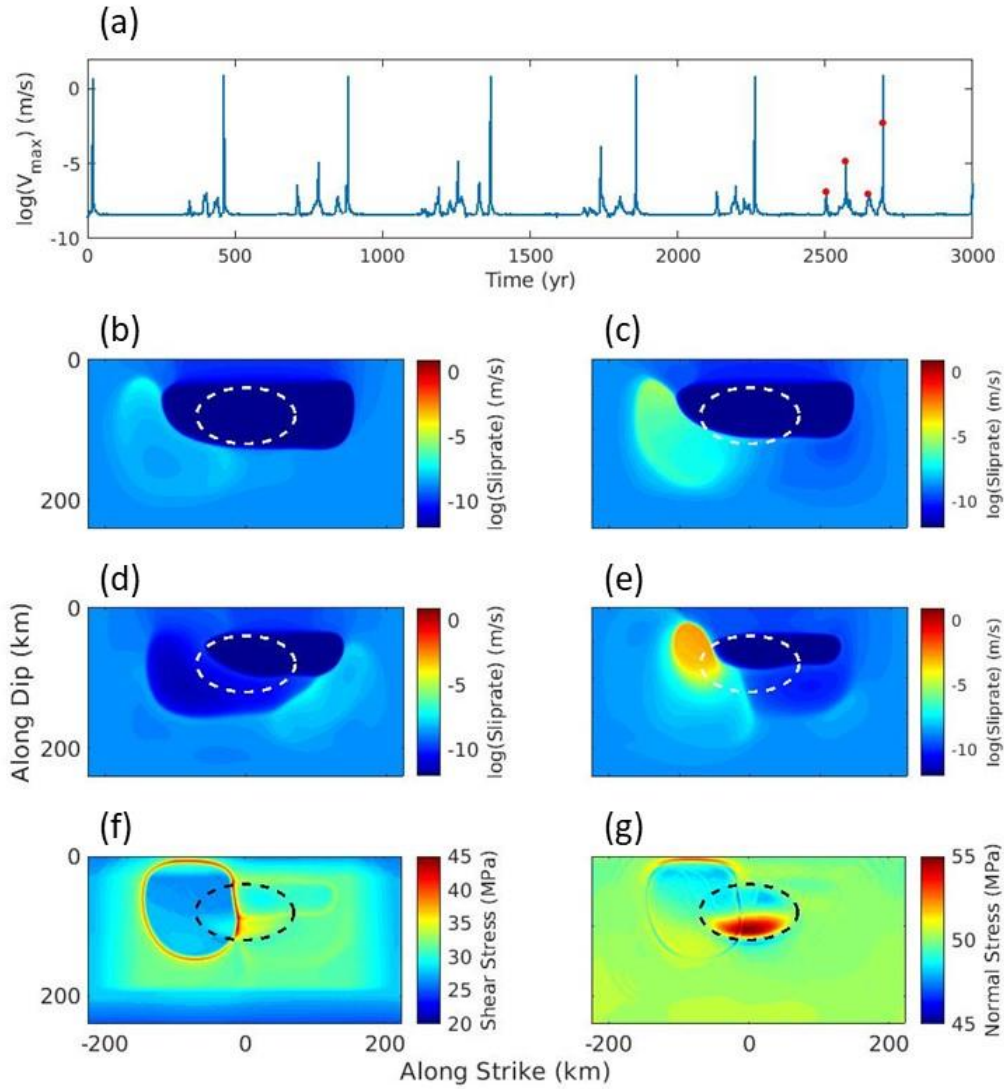


Figure 4. 11 Simulation results of the nonplanar subduction fault model with a low-height, broad-base bump. (a) shows maximum slip velocity history in log scale. Red dots in the interseismic and nucleation phases before the seventh event sequentially denote the time of the logarithmic sliprate snapshots in (b), (c), (d), and (e). Shear and normal stress distributions for a coseismic moment of the seventh event are shown in (f) and (g), respectively. White ellipses in the sliprate snapshots and black ellipses in the stress distributions denote the size and location of the bump geometry on the fault.

4.4 A Subduction Fault Model with Nonplanar Fault Geometry

We examine the geometrical effect in controlling earthquake cycle patterns by conducting earthquake cycle simulation on the nonplanar fault model. Numerical simulation results are collectively presented in Figure 4. 11. The maximum sliprate history shows a sequence of seven M9 great earthquakes in a time span of 3000 years, with an average recurrence interval of 446 years (Figure 4. 11a). Before each giant earthquake occurs, a series of three successive aseismic transients are typically observed, with various magnitudes of maximum sliprate. These three aseismic transients emerge and propagate along the edge of the locked zone which shrinks continuously during the interseismic phase (Figure 4. 11b-d), followed by the last aseismic transient in the interseismic phase that will eventually develop into a nucleation patch for the giant earthquake (Figure 4. 11e). In most cases, we do not observe significant geometrical effects of the bump geometry on interseismic faulting behavior. In the coseismic phase, the bump geometry has little effect in stopping the rupture front (Figure 4. 11f). Nevertheless, our numerical results indicate that fault slip on the explicit nonplanar fault geometry, either seismic or aseismic, will induce local normal stress change (elevated on downdip side and reduced on the updip side, as shown in Figure 4. 11g), which can be accumulated over time as fault slip continues. However, the explicit low-height, broad-width bump geometry inferred from observed residual topography accumulates normal stress perturbation at a relatively slow rate, resulting in a total change of ~ 5 MPa over a time span of 3000 years. Suppose every cycle has a total fault slip of 40 m, the low height-to-width ratio along dip direction (semi-minor axis) in this model ($2 \text{ km} / 40 \text{ km} = 0.05$) suggests a shortening of ~ 2 m in

the overriding plate perpendicular to the downdip compressional side of the bump geometry in every cycle. Using a shear modulus of ~ 32 GPa, such a compression along the 40 km semi-minor axis gives a rough estimate of 1.6 MPa increase in normal stress on the downdip compressional side, which has the same order of magnitude as what we observe in our simulation. Therefore, a significantly high stress/strength condition is not yet established by the specific nonplanar geometry in the model and the earthquake cycle pattern is barely affected.

4.5 Discussion

In this study, we apply our FEM-based earthquake cycle simulator to conduct earthquake cycle simulations of the Japan Trench Subduction zone in the Tohoku area. We incorporate structural heterogeneity in the subduction model to better understand multicycle behavior of the megathrust fault. The modeled earthquake sequence exhibits rich complexity in faulting behavior and resembles many observed features of seismicity in the Tohoku area, including the 2011 Tohoku earthquake. The FEM-based earthquake cycle simulator also enables us to perform earthquake cycle simulations on fault surface with geometrical complexities.

4.5.1 Slip Pattern of the 2011 Tohoku Megathrust Earthquake

The 2011 Tohoku earthquake was extensively observed by dense seismic, geodetic, and tsunami networks. Numerous inversions of the source model for the 2011 event have been constructed from diverse data sets by different research groups (e.g., *Ammon et al.*, 2011; *Ide et al.*, 2011; *Lay et al.*, 2011; *Simons et al.*, 2011; *Yokota et al.*, 2011; *Iinuma et al.*, 2012; *Bletery et al.*, 2014; *Minson et al.*, 2014). *Sun et al.* (2017) compile 45 models from various inversion strategies and show that these models commonly indicate massive slip updip of the hypocenter extending to the trench and tapered slip downdip of the hypocenter toward to deeper portion of the fault. However, due to the poor constraint of the far off-shore area from the geophysical data mainly collected near onshore, it remains controversial whether the largest slip occurs near the hypocenter or the trench area. In our preferred modeled giant earthquake, although the dynamic rupture penetrates into the velocity strengthening area and generates large slip near the trench, the strongest asperity is located immediately updip of the nucleation zone, which corresponds to the large stress drop area on the fault. We attribute the less slip near the trench to the velocity-strengthening property near the trench accounting for the abundant sediments brought into the subduction zone by the subducting process, which reduces the amount of slip by generating in situ negative stress drop. Nevertheless, our preferred model shows a possible scenario that interseismic deformation activates the downdip portion of the fault and keeps the updip portion locked, which is responsible for largest slip updip of the nucleation patch. Whether the largest slip occurs near the hypocenter or the trench may require additional knowledge of geologic conditions near

the trench that can significantly modulate coseismic slip, such as thermal pressurization (Bletery *et al.*, 2014) and/or neutral frictional property instead of velocity strengthening (Sun *et al.*, 2017).

4.5.2 Giant Earthquake Sequence

In both the heterogeneous model and the nonplanar fault model, roughly periodic giant earthquakes are generated, mainly due to the setting of a single VW zone on the fault, as pointed out by previous studies (e.g., Hori and Miyazaki, 2011; Bassett *et al.*, 2016). Both model show a recurrence interval of 300~400 years for the M9 giant earthquakes, shorter than the ~700 year value inferred from paleoseismic studies. The largest slip on the fault in both models is 30~40 m, also less than the ~50 m maximum slip measured from various inversion models for the 2011 event. Although the observations are rough estimates, deficiency in both recurrence time and maximum coseismic slip may still imply some oversimplified features in our model, such as lack of highly stressed area in the seismogenic zone that could lead to greater stress drop and stronger asperity, and/or the velocity-strengthening condition in shallow portion of the fault that inhibits larger slip near the trench.

Nucleation of these giant earthquakes in both models tends to occur on the left or the right side of the VW zone, resulting in unilateral rupture propagation. There are only two modeled events in the heterogeneous model that nucleate close to the center of the fault and generate bilateral rupture, one with large slip on the side of the nucleation patch

and the other with large slip updip of the nucleation patch. The latter one is the preferred event that resembles the 2011 earthquake the most among all simulated events. This preferred event nucleates when an aseismic transient propagates laterally along the fault and encounters heterogeneous stress imprinted by previous aseismic transients, which provides a possible scenario for the nucleation process of the 2011 earthquake. However, considering that this preferred event is one of a kind in the modeled sequence, it remains an open question whether the same pattern will recur again if simulation continues.

4.5.3 Aseismic Transients and M7~8 Large Earthquakes

In comparison with M9 giant earthquakes, M7~8 large earthquakes can be viewed as “small” events with relatively small ruptured area distributed on the subduction fault zone. Coexistence of large and small events in earthquake cycle simulation requires small value of the characteristic slip distance L , as pointed out by *Lapusta and Rice* (2003), because small events nucleate from small nucleation patches, which is proportional to L as shown by equation (4.3). When a small L is used, both large and small events can be reproduced with a similar nucleation patch size, and the final earthquake size depends on whether the conditions on the fault favor further spontaneous rupture propagation from the nucleation patch. In contrast, large L leads to large critical nucleation patch dimension that is unable to resolve small events on the fault. Therefore, realistic L value of micrometers measured in laboratory experiments is desired in attempts to simulate realistic earthquake cycles. However, from numerical perspective, the parameter L strictly

constrains the element size of the model and the time step length in a proportional manner, which leads to extremely challenging computational problems when small L is desired in resolving small events and large model size is desired in reproducing large events. In this study, we adopt an unrealistically large value of 0.15 m for L (corresponding to $W_s/h^* \sim 1$), mainly for feasibility of numerical calculation. As a consequence, only M9 earthquakes but no M7~8 events are generated in the heterogeneous model and the nonplanar fault model. Nevertheless, aseismic transients are seen during the interseismic phase, mainly in the area close to the locked-to-creeping edge, similar to previous numerical studies using RSF laws with heterogeneous frictional properties (VS and VW) to simulate slow slip events (e.g., *Liu and Rice, 2005; Liu and Rice, 2007; Liu and Rice, 2009; Li and Liu, 2016*). Some of the aseismic slips have accelerated to moderate sliprate levels and have expanded to moderate sizes. They are likely to turn into dynamic events, but the critical nucleation patch dimension does not allow. Otherwise, some of them may turn into small events that are confined by unfavorable conditions, leaving highly heterogeneous stress distribution on the fault, and the others may turn into large events that are promoted by favorable conditions, rupturing the entire fault area.

Comparison between the planar fault model with heterogeneous structure and the nonplanar model with homogeneous medium suggests that the complex structure can generate complex pattern of the aseismic transients. In the heterogeneous model, much more aseismic bursts are identified in the interseismic phase after the 150 to 200 year quiescent period, with intervals ranging from 5 to 50 years between individual transients. In contrast, homogeneous model shows a simple three transient pattern preceding the main

events with roughly 70 year interval. Although no subevents of M7~8 are reproduced in both models, the complex pattern with numerous aseismic transients and shorter intervals is more likely to resemble the realistic seismicity including the M7~8 events observed in the Miyagi-Oki and Fukuyama-Oki zones near the deep portion of the Japan Trench subduction zone during the past century. The complex structure, especially the 1D velocity model, may play a role similar to the low-rigidity layer or the shallow compliant basin structure in previous studies in slowing down updip propagation of the stress concentration front from the loading bottom of the VW zone when it crosses the transition between high and low rigidity. While homogeneous model allows natural development of the aseismic transients, the 1D layering model confines the aseismic slip to the deep portion of the fault temporarily, leading to rapid and numerous recurrence of these small aseismic events (possibly small seismic events if L is small enough). Failure of constraining the development of aseismic transients will lead to seismic/aseismic events of greater size, even the giant megathrust earthquakes.

In this study, the nonplanar fault geometry model with large-scale relief of low height-to-width ratio does not show significant impact within a specific length of simulation time, but this model does not rule out the possible effect of nonplanar fault geometry, which is still an important source of stress heterogeneity that could modulate earthquake cycle behavior. As pointed out by previous studies, nonplanar fault geometry can generate highly stressed patches that can either act as barriers or fail as strong asperities, depending on the prestress level. More experiments of appropriate setting for nonplanar fault geometry are desired to explore how geometrical irregularities may

elongate recurrence time of giant events and control the generation of earthquakes of various sizes. In addition, application of small value of L is important in exploring geometrical effects. When L is large, dynamic rupture nucleates from large patch sizes and is more likely to be energetic and insensitive to stress heterogeneity on the fault. When L is small, dynamic rupture nucleates from small patches and conditionally turns into small or large events, depending on stress heterogeneity on the fault. To apply small L , better FEM mesh scheme is needed to improve computational efficiency of the model such that a small element size satisfying the strict constraint from a small L can be used in modeling.

4.6 Conclusions

The 2011 M9 Tohoku earthquake, which is possibly part of a supercycle of similar megathrust earthquakes, occurred in the Japan Trench subduction zone where only M7~8 earthquakes are recorded in the past century. In order to do a better job in seismic hazard analysis, it is important to investigate the conditions that operate multiple earthquake cycles and generate both giant and large earthquakes. In this study, we employ our newly developed FEM-based earthquake cycle simulator with rate-and-state friction law to explore the effects of realistic structural heterogeneity and complex fault geometry near the large slip area of the 2011 event on generating both M9 and M7~8 events. These two factors are explored independently by two individual models, a heterogeneous model with planar fault, and a homogeneous model with a nonplanar fault. We find that both models generate M9 giant earthquake sequences, but with contrasting details. The heterogeneous model reproduces one giant event in the sequence that exhibits similarities to the 2011

Tohoku event in terms of slip distribution and foreshock sequences. The modeled earthquake sequence also shows complex aseismic slip transients that are possibly associated with M7~8 events between megathrust earthquakes. The nonplanar fault model with low height and broad base exhibits stress accumulation on the geometrical irregularity over time, but its earthquake sequence pattern is relatively simple and the geometrical irregularity has little effect on dynamic rupture. The heterogeneity model is more likely to reveal the realistic situation, but more efforts should be made to refine model parameters for better understanding of the physical controls on supercycles of megathrust earthquakes along with regular large earthquakes.

CHAPTER V

SUMMARY

Scientific questions regarding the 2011 Tohoku earthquake and the megathrust fault along the Japan Trench subduction zone remain to be addressed. We developed powerful numerical modeling tools to conduct numerical experiments to explore physical conditions that affect dynamic rupture and earthquake cycle processes. We explicitly incorporate nonplanar thrust fault geometry into a three-dimensional finite element model to numerically simulate spontaneous dynamic rupture, and explore how dynamic ruptures would behave on a nonplanar fault surface under the influence of different friction laws. Our results show that a subducted oceanic relief (a bump) could act as a rupture barrier with its high strength area being unfavorable for rupture propagation, and such a geometrical effect varies with the dimension of a bump. When a bump is too high, the dynamic rupture is completely arrested. When the bump is too low, the rupture is barely affected. When the bump is of an intermediate height, the rupture is obstructed by the bump and splits into two parts, which circumvent the high strength area of the bump and then converge on the other side, triggering a strong slip velocity pulse. The relation between these rupture behaviors and bump geometry under a given prestress condition varies with the specific forms of friction law, which determines how fast a rupture releases energy and how strong a bump can be as a barrier.

We then present a new earthquake simulator to describe faulting behavior and explain earthquake characteristics on fault systems. The method is developed based on the dynamic FEM EQdyna for three-dimensional spontaneous rupture modeling. Numerical simulation on a vertical strike-slip fault verifies the applicability of the methodology. We employ the developed methodology for numerical investigation of earthquake cycle behavior on thrust faults with various dipping angles. We find an empirical linear scaling relations of recurrence time and seismic moment with respect to the sinusoidal function of the dip angle. Thrust faults tend to produce earthquake cycles with elongated recurrence time and increased released seismic energy. Moreover, we find that the asymmetry in particle displacement between the hanging wall and the footwall caused by earthquakes on dipping fault geometry is recovered during the interseismic phase.

We further employ our FEM-based earthquake cycle simulator with rate-and-state friction law to explore the effects of realistic structural heterogeneity and complex fault geometry near the large slip area of the 2011 event on generating both M9 and M7~8 events. We find that both heterogeneous model and nonplanar fault model generate M9 giant earthquake sequences, but with contrasting details. The heterogeneous model reproduces one giant event in the sequence that exhibits some similar features to the 2011 Tohoku event in terms of slip distribution and foreshock sequences. The modeled earthquake sequence also shows complex aseismic slip transients between megathrust earthquakes that are possibly associated with M7~8 events. The nonplanar fault model with low height and broad base exhibits stress accumulation on the geometrical irregularity over time, but its earthquake sequence pattern is relatively simple and the

geometrical irregularity has little effect on dynamic rupture. The heterogeneity model is more likely to reveal the realistic situation, but more efforts should be made to refine model parameters (such as characteristic slip distance) for better understanding of the physical controls on supercycles of megathrust earthquakes along with regular large earthquakes.

REFERENCES

- Aagaard, B. T., M. G. Knepley, and C. A. Williams (2013), A domain decomposition approach to implementing fault slip in finite-element models of quasi-static and dynamic crustal deformation, *J. Geophys. Res. Solid Earth*, *118*(6), 3059-3079.
- Ali, N. B. H., A. C. Sychterz, and I. F. Smith (2017), A dynamic-relaxation formulation for analysis of cable structures with sliding-induced friction, *International Journal of Solids and Structures*, *126*, 240-251.
- Ammon, C. J., T. Lay, H. Kanamori, and M. Cleveland (2011), A rupture model of the 2011 off the Pacific coast of Tohoku Earthquake, *Earth Planets and Space*, *63*(7), 693.
- Ampuero, J. P., and A. M. Rubin (2008), Earthquake nucleation on rate and state faults—Aging and slip laws, *J. Geophys. Res.*, *113*, B01302, doi:10.1029/2007JB005082.
- Ando, R., and K. Imanishi (2011), Possibility of M w 9.0 mainshock triggered by diffusional propagation of after-slip from M w 7.3 foreshock, *Earth, planets and space*, *63*(7), 47, doi:10.5047/eps.2011.05.
- Andrews, D. J. (1976), Rupture velocity of plane strain shear cracks, *J. Geophys. Res.*, *81*(32), 5679-5687, doi:10.1029/JB081i032p05679.
- Andrews, D. J. (1999), Test of two methods for faulting in finite-difference calculations, *Bull. Seismol. Soc. Am.*, *89*(4), 931-937.
- Bangs, N. L. B., S. P. S. Gulick, and T. H. Shipley (2006), Seamount subduction erosion in the Nankai Trough and its potential impact on the seismogenic zone, *Geology*, *34*(8), 701-704, doi:10.1130/G22451.1.

- Barall, M. (2009), A grid-doubling finite-element technique for calculating dynamic three-dimensional spontaneous rupture on an earthquake fault, *Geophys. J. Int.*, *178*, 845-859, doi:10.1111/j.1365-246X.2009.04190.x.
- Bassett, D., D. T. Sandwell, Y. Fialko, and A. B. Watts (2016), Upper-plate controls on co-seismic slip in the 2011 magnitude 9.0 Tohoku-oki earthquake, *Nature*, *531*(7592), 92, doi:10.1038/nature16945.
- Beeler, N., D. Lockner, and S. Hickman (2001), A simple stick-slip and creep-slip model for repeating earthquakes and its implication for microearthquakes at Parkfield, *Bull. Seismol. Soc. Am.*, *91*(6), 1797-1804, doi:10.1785/0120000096.
- Beeler, N. M., T. E. Tullis, and D. L. Goldsby (2008), Constitutive relationships and physical basis of fault strength due to flash heating, *J. Geophys. Res.*, *113*(B1), doi:10.1029/2007JB004988.
- Bhat, H. S., M. Olives, R. Dmowska, and J. R. Rice (2007), Role of fault branches in earthquake rupture dynamics, *J. Geophys. Res.*, *112*(B11309), doi:10.1029/2007JB005027.
- Bizzarri, A., and M. Cocco (2003), Slip-weakening behavior during the propagation of dynamic ruptures obeying rate- and state-dependent friction laws, *J. Geophys. Res.*, *108*(B8), doi:10.1029/2002JB002198.
- Bizzarri, A., M. Cocco, D. J. Andrews, and E. Boschi (2001), Solving the dynamic rupture problem with different numerical approaches and constitutive laws, *Geophys. J. Int.*, *144*(3), 656-678, doi:10.1046/j.1365-246x.2001.01363.x.

- Bletery, Q., et al. (2014), A detailed source model for the Mw9.0 Tohoku-Oki earthquake reconciling geodesy, seismology, and tsunami records, *J. Geophys. Res. Solid Earth*, 119(10), 7636-7653, doi:10.1002/2014JB011261.
- Chen, K. H., R. M. Nadeau, and R. J. Rau (2007), Towards a universal rule on the recurrence interval scaling of repeating earthquakes?, *Geophys. Res. Lett.*, 34(16), doi:10.1029/2007GL030554.
- Chen, T., and N. Lapusta (2009), Scaling of small repeating earthquakes explained by interaction of seismic and aseismic slip in a rate and state fault model, *J. Geophys. Res. Solid Earth*, 114(B1), doi:10.1029/2008JB005749.
- Chester, F. M., et al. (2013), Structure and composition of the plate-boundary slip zone for the 2011 Tohoku-Oki earthquake, *Science*, 342(6163), 1208-1211.
- Cloos, M. (1992), Thrust-type subduction-zone earthquakes and seamount asperities: A physical model for seismic rupture, *Geology*, 20(7), 601-604, doi:10.1130/0091-7613(1992)020<0601:TTSZEA>2.3.CO;2.
- Collot, J. Y., et al. (2017), Subducted Oceanic Relief Locks the Shallow Megathrust in Central Ecuador, *J. Geophys. Res. Solid Earth*, doi:10.1002/2016JB013849.
- Das, S., and B. V. Kostrov (1983), Breaking of a single asperity: rupture process and seismic radiation, *J. Geophys. Res.*, 88(B5), 4277-4288, doi:10.1029/JB088iB05p04277.
- Day, S. M., L. A. Dalguer, N. Lapusta, and Y. Liu (2005), Comparison of finite difference and boundary integral solutions to three-dimensional spontaneous rupture, *J. Geophys. Res.*, 110(B12), doi:10.1029/2005jb003813.

- Di Toro, G., et al. (2011), Fault lubrication during earthquakes, *Nature*, 471(7339), 494-498, doi:10.1038/nature09838.
- Dieterich, J. H. (1978), Time-dependent friction and the mechanics of stick-slip, *Pure Appl. Geophys.*, 116(4-5), 790-806, doi:10.1007/BF00876539.
- Dieterich, J. H. (1979), Modeling of rock friction: 1. Experimental results and constitutive equations, *J. Geophys. Res.*, 84(B5), 2161-2168, doi:10.1029/JB084iB05p02161.
- Dieterich, J. H. (1992), Earthquake nucleation on faults with rate-and state-dependent strength, *Tectonophysics*, 211(1), 115-134.
- Dieterich, J. H., and K. B. Richards-Dinger (2010), Earthquake recurrence in simulated fault systems, *Pure Appl. Geophys.*, 167(8-9), 1087-1104.
- Ding, M., and J. Lin (2016), Deformation and faulting of subduction overriding plate caused by a subducted seamount, *Geophys. Res. Lett.*, 43(17), 8936-8944, doi:10.1002/2016GL069785.
- Dominguez, S., S. E. Lallemand, J. Malavieille, and R. Von Huene (1998), Upper plate deformation associated with seamount subduction, *Tectonophysics*, 293(3), 207-224, doi:10.1016/S0040-1951(98)00086-9.
- Duan, B. (2010), Role of initial stress rotations in rupture dynamics and ground motion: A case study with implications for the Wenchuan earthquake, *J. Geophys. Res. Solid Earth*, 115(B5), doi:10.1029/2009JB006750.

- Duan, B. (2012), Dynamic rupture of the 2011 Mw 9.0 Tohoku-Oki earthquake: Roles of a possible subducting seamount, *J. Geophys. Res.*, *117*(B5), doi:10.1029/2011JB009124.
- Duan, B., and S. M. Day (2008), Inelastic strain distribution and seismic radiation from rupture of a fault kink, *J. Geophys. Res.*, *113*(B12), doi:10.1029/2008JB005847.
- Duan, B., and D. D. Oglesby (2005a), The dynamics of thrust and normal faults over multiple earthquake cycles: Effects of dipping fault geometry, *Bull. Seismol. Soc. Am.*, *95*(5), 1623-1636, doi:10.1785/0120040234.
- Duan, B., and D. D. Oglesby (2005b), Multicycle dynamics of nonplanar strike-slip faults, *J. Geophys. Res.*, *110*(B3), doi:10.1029/2004JB003298.
- Duan, B., and D. D. Oglesby (2006), Heterogeneous fault stresses from previous earthquakes and the effect on dynamics of parallel strike-slip faults, *J. Geophys. Res.*, *111*(B5), doi:10.1029/2005JB004138.
- Duan, B., and D. D. Oglesby (2007), Nonuniform prestress from prior earthquakes and the effect on dynamics of branched fault systems, *J. Geophys. Res.*, *112*(B5), doi:10.1029/2006JB004443.
- Dunham, E. M. (2007), Conditions governing the occurrence of supershear ruptures under slip-weakening friction, *J. Geophys. Res. Solid Earth*, *112*(B7), doi:10.1029/2006JB004717.
- Dunham, E. M., P. Favreau, and J. M. Carlson (2003), A supershear transition mechanism for cracks, *Science*, *299*(5612), 1557-1559, doi:10.1126/science.1080650.

- Erickson, B. A., and S. M. Day (2016), Bimaterial effects in an earthquake cycle model using rate-and-state friction, *J. Geophys. Res. Solid Earth*, *121*(4), 2480-2506.
- Erickson, B. A., and E. M. Dunham (2014), An efficient numerical method for earthquake cycles in heterogeneous media: Alternating subbasin and surface-rupturing events on faults crossing a sedimentary basin, *J. Geophys. Res. Solid Earth*, *119*(4), 3290-3316, doi:10.1002/2013JB010614.
- Fujii, Y., K. Satake, S. i. Sakai, M. Shinohara, and T. Kanazawa (2011), Tsunami source of the 2011 off the Pacific coast of Tohoku Earthquake, *Earth, planets and space*, *63*(7), 815-820.
- Fukuyama, E., and S. Hok (2015), Dynamic Overshoot Near Trench Caused by Large Asperity Break at Depth, *Pure Appl. Geophys.*, *172*(8), 2157-2165, doi:10.1007/s00024-013-0745-z.
- Fukuyama, E., and R. Madariaga (1998), Rupture dynamics of a planar fault in a 3D elastic medium: rate-and slip-weakening friction, *Bull. Seismol. Soc. Am.*, *88*(1), 1-17.
- Fukuyama, E., and R. Madariaga (2000), Dynamic propagation and interaction of a rupture front on a planar fault, in *Microscopic and Macroscopic Simulation: Towards Predictive Modelling of the Earthquake Process*, edited, pp. 1959-1979, Springer, doi:10.1007/978-3-0348-7695-7_9.
- Fulton, P., et al. (2013), Low coseismic friction on the Tohoku-Oki fault determined from temperature measurements, *Science*, *342*(6163), 1214-1217.

- Gabriel, A. A., J. P. Ampuero, L. A. Dalguer, and P. M. Mai (2012), The transition of dynamic rupture styles in elastic media under velocity-weakening friction, *J. Geophys. Res. Solid Earth*, 117(B9), doi:10.1029/2012JB009468.
- Govers, R., K. Furlong, L. Wiel, M. Herman, and T. Broerse (2017), The Geodetic Signature of the Earthquake Cycle at Subduction Zones: Model Constraints on the Deep Processes, *Rev. Geophys.*, doi:10.1002/2017RG000586.
- Harris, R. A., et al. (2018), A Suite of Exercises for Verifying Dynamic Earthquake Rupture Codes, *Seismol. Res. Lett.*, 89(3), 1146-1162, doi:10.1785/0220170222.
- Harris, R. A., et al. (2011), Verifying a computational method for predicting extreme ground motion, *Seismol. Res. Lett.*, 82(5), 638-644, doi:10.1785/gssrl.82.5.638.
- Harris, R. A., et al. (2009), The SCEC/USGS dynamic earthquake rupture code verification exercise, *Seismol. Res. Lett.*, 80(1), 119-126, doi:10.1785/gssrl.80.1.119.
- Hashimoto, C., A. Noda, T. Sagiya, and M. Matsu'ura (2009), Interplate seismogenic zones along the Kuril–Japan trench inferred from GPS data inversion, *Nat. Geosci.*, 2(2), 141-144.
- Hori, T., and S. i. Miyazaki (2011), A possible mechanism of M 9 earthquake generation cycles in the area of repeating M 7~ 8 earthquakes surrounded by aseismic sliding, *Earth, planets and space*, 63(7), 48, doi:10.5047/eps.2011.06.022.
- Ida, Y. (1972), Cohesive force across the tip of a longitudinal-shear crack and Griffith's specific surface energy, *J. Geophys. Res.*, 77(20), 3796-3805, doi:10.1029/JB077i020p03796.

- Ide, S., A. Baltay, and G. C. Beroza (2011), Shallow dynamic overshoot and energetic deep rupture in the 2011 Mw 9.0 Tohoku-Oki earthquake, *Science*, 332(6036), 1426-1429.
- Iinuma, T., et al. (2012), Coseismic slip distribution of the 2011 off the Pacific Coast of Tohoku Earthquake (M9.0) refined by means of seafloor geodetic data, *J. Geophys. Res. Solid Earth*, 117(B7), doi:10.1029/2012JB009186.
- Ikehara, K., et al. (2016), Documenting large earthquakes similar to the 2011 Tohoku-oki earthquake from sediments deposited in the Japan Trench over the past 1500 years, *Earth Planet. Sci. Lett.*, 445, 48-56.
- Ikehara, K., K. Usami, T. Kanamatsu, T. Danhara, and T. Yamashita (2017), Three important Holocene tephras off the Pacific coast of the Tohoku region, Northeast Japan: implications for correlating onshore and offshore event deposits, *Quaternary International*, 456, 138-153, doi:10.1016/j.quaint.2017.08.022.
- Ito, A., et al. (2005), Bending of the subducting oceanic plate and its implication for rupture propagation of large interplate earthquakes off Miyagi, Japan, in the Japan Trench subduction zone, *Geophys. Res. Lett.*, 32(5), doi:10.1029/2004GL022307.
- Jacobs, A., D. Sandwell, Y. Fialko, and L. Sichoix (2002), The 1999 (M w 7.1) Hector Mine, California, earthquake: Near-field postseismic deformation from ERS interferometry, *Bull. Seismol. Soc. Am.*, 92(4), 1433-1442, doi:10.1785/0120000908.

- Kaneko, Y., J. P. Ampuero, and N. Lapusta (2011), Spectral-element simulations of long-term fault slip: Effect of low-rigidity layers on earthquake-cycle dynamics, *J. Geophys. Res. Solid Earth*, *116*(B10), doi:10.1029/2011JB008395.
- Kase, Y., and S. M. Day (2006), Spontaneous rupture processes on a bending fault, *Geophys. Res. Lett.*, *33*(10), doi:10.1029/2006GL025870.
- Kato, A., et al. (2012), Propagation of slow slip leading up to the 2011 Mw 9.0 Tohoku-Oki earthquake, *Science*, *1215*141, doi:10.1126/science.1215141.
- Kilic, B., and E. Madenci (2010), An adaptive dynamic relaxation method for quasi-static simulations using the peridynamic theory, *Theoretical and Applied Fracture Mechanics*, *53*(3), 194-204.
- Kodaira, S., N. Takahashi, A. Nakanishi, S. Miura, and Y. Kaneda (2000), Subducted seamount imaged in the rupture zone of the 1946 Nankaido earthquake, *Science*, *289*(5476), 104-106, doi:10.1126/science.289.5476.104.
- Kosloff, D., and G. A. Frazier (1978), Treatment of hourglass patterns in low order finite element codes, *International journal for numerical and analytical methods in geomechanics*, *2*(1), 57-72, doi:10.1002/nag.1610020105.
- Kyriakopoulos, C., and A. V. Newman (2016), Structural asperity focusing locking and earthquake slip along the Nicoya megathrust, Costa Rica, *J. Geophys. Res. Solid Earth*, *121*(7), 5461-5476, doi:10.1002/2016JB012886.
- Lapusta, N., and Y. Liu (2009), Three-dimensional boundary integral modeling of spontaneous earthquake sequences and aseismic slip, *J. Geophys. Res. Solid Earth*, *114*(B9), doi:10.1029/2008JB005934.

- Lapusta, N., and J. R. Rice (2003), Nucleation and early seismic propagation of small and large events in a crustal earthquake model, *J. Geophys. Res. Solid Earth*, *108*(B4).
- Lapusta, N., J. R. Rice, Y. Ben-Zion, and G. Zheng (2000), Elastodynamic analysis for slow tectonic loading with spontaneous rupture episodes on faults with rate- and state-dependent friction, *J. Geophys. Res.*, *105*(B10), 23765-23789, doi:10.1029/2000JB900250.
- Latour, S., et al. (2011), Effective friction law for small-scale fault heterogeneity in 3D dynamic rupture, *J. Geophys. Res. Solid Earth*, *116*(B10).
- Lay, T., C. J. Ammon, H. Kanamori, L. Xue, and M. J. Kim (2011), Possible large near-trench slip during the 2011 M w 9.0 off the Pacific coast of Tohoku Earthquake, *Earth, planets and space*, *63*(7), 32, doi:10.5047/eps.2011.05.033.
- Li, D., and Y. Liu (2016), Spatiotemporal evolution of slow slip events in a nonplanar fault model for northern Cascadia subduction zone, *J. Geophys. Res. Solid Earth*, *121*(9), 6828-6845, doi:10.1002/2016JB012857.
- Liu, D., and B. Duan (2018), Scenario Earthquake and Ground-Motion Simulations in North China: Effects of Heterogeneous Fault Stress and 3D Basin Structure, *Bull. Seismol. Soc. Am.*, doi:10.1785/0120170374.
- Liu, X., and D. Zhao (2018), Upper and lower plate controls on the great 2011 Tohoku-oki earthquake, *Science Advances*, *4*(6), eaat4396, doi:10.1126/sciadv.aat4396.

- Liu, Y., and J. R. Rice (2005), Aseismic slip transients emerge spontaneously in three-dimensional rate and state modeling of subduction earthquake sequences, *J. Geophys. Res. Solid Earth*, *110*(B8), doi:10.1029/2004JB003424.
- Liu, Y., and J. R. Rice (2007), Spontaneous and triggered aseismic deformation transients in a subduction fault model, *J. Geophys. Res. Solid Earth*, *112*(B9), doi:10.1029/2007JB004930.
- Liu, Y., and J. R. Rice (2009), Slow slip predictions based on granite and gabbro friction data compared to GPS measurements in northern Cascadia, *J. Geophys. Res. Solid Earth*, *114*(B9), doi:10.1029/2008JB006142.
- Luo, B., and B. Duan (2018), Dynamics of Non-planar Thrust Faults Governed by Various Friction Laws, *J. Geophys. Res. Solid Earth*, doi:10.1029/2017JB015320.
- Madariaga, R. (1976), Dynamics of an expanding circular fault, *Bull. Seismol. Soc. Am.*, *66*(3), 639-666.
- Minoura, K., F. Imamura, D. Sugawara, Y. Kono, and T. Iwashita (2001), The 869 Jogan tsunami deposit and recurrence interval of large-scale tsunami on the Pacific coast of northeast Japan, *Journal of Natural Disaster Science*, *23*(2), 83-88.
- Minson, S., et al. (2014), Bayesian inversion for finite fault earthquake source models—II: the 2011 great Tohoku-oki, Japan earthquake, *Geophys. J. Int.*, *198*(2), 922-940, doi:10.1093/gji/ggu170.

- Miura, S., et al. (2005), Structural characteristics off Miyagi forearc region, the Japan Trench seismogenic zone, deduced from a wide-angle reflection and refraction study, *Tectonophysics*, 407(3), 165-188.
- Mochizuki, K., T. Yamada, M. Shinohara, Y. Yamanaka, and T. Kanazawa (2008), Weak interplate coupling by seamounts and repeating M~7 earthquakes, *Science*, 321(5893), 1194-1197, doi:10.1126/science.1160250.
- Nadeau, R. M., and L. R. Johnson (1998), Seismological studies at Parkfield VI: Moment release rates and estimates of source parameters for small repeating earthquakes, *Bull. Seismol. Soc. Am.*, 88(3), 790-814.
- Namegaya, Y., and K. Satake (2014), Reexamination of the AD 869 Jogan earthquake size from tsunami deposit distribution, simulated flow depth, and velocity, *Geophys. Res. Lett.*, 41(7), 2297-2303, doi:10.1002/2013GL058678.
- Noda, H., and N. Lapusta (2010), Three-dimensional earthquake sequence simulations with evolving temperature and pore pressure due to shear heating: Effect of heterogeneous hydraulic diffusivity, *J. Geophys. Res.*, 115(B12), doi:10.1029/2010JB007780.
- Noda, H., and N. Lapusta (2013), Stable creeping fault segments can become destructive as a result of dynamic weakening, *Nature*, 493(7433), 518, doi:10.1038/nature11703.
- Oakley, D. R., and N. F. Knight (1995), Adaptive dynamic relaxation algorithm for non-linear hyperelastic structures Part I. Formulation, *Computer methods in applied mechanics and engineering*, 126(1-2), 67-89.

- Oglesby, D. D., and R. J. Archuleta (2003), The three-dimensional dynamics of a nonplanar thrust fault, *Bull. Seismol. Soc. Am.*, 93(5), 2222-2235, doi:10.1785/0120020204.
- Oglesby, D. D., R. J. Archuleta, and S. B. Nielsen (1998), Earthquakes on dipping faults: the effects of broken symmetry, *Science*, 280(5366), 1055-1059.
- Oglesby, D. D., R. J. Archuleta, and S. B. Nielsen (2000), The three-dimensional dynamics of dipping faults, *Bull. Seismol. Soc. Am.*, 90(3), 616-628.
- Ozawa, S., M. Kaidzu, M. Murakami, T. Imakiire, and Y. Hatanaka (2004), Coseismic and postseismic crustal deformation after the M_w 8 Tokachi-oki earthquake in Japan, *Earth, planets and space*, 56(7), 675-680, doi:10.1186/BF03352530.
- Ozawa, S., et al. (2011), Coseismic and postseismic slip of the 2011 magnitude-9 Tohoku-Oki earthquake, *Nature*, 475(7356), 373-376.
- Page, M. T., E. M. Dunham, and J. Carlson (2005), Distinguishing barriers and asperities in near-source ground motion, *J. Geophys. Res. Solid Earth*, 110(B11), doi:10.1029/2005JB003736.
- Palmer, A. C., and J. R. Rice (1973), The growth of slip surfaces in the progressive failure of over-consolidated clay, *Proc. R. Soc. London*, 332, 527-548, doi:10.1098/rspa.1973.0040.
- Papadrakakis, M. (1981), A method for the automatic evaluation of the dynamic relaxation parameters, *Computer methods in applied mechanics and engineering*, 25(1), 35-48.

- Perrin, G., J. R. Rice, and G. Zheng (1995), Self-healing slip pulse on a frictional surface, *Journal of the Mechanics and Physics of Solids*, 43(9), 1461-1495, doi:10.1016/0022-5096(95)00036-I.
- Pollitz, F. F. (2012), ViscoSim earthquake simulator, *Seismol. Res. Lett.*, 83(6), 979-982, doi:10.1785/0220120050.
- Qiang, S. (1988), An adaptive dynamic relaxation method for nonlinear problems, *Computers & Structures*, 30(4), 855-859.
- Rezaiee-Pajand, M., and H. Estiri (2017), Comparative analysis of three-dimensional frames by dynamic relaxation methods, *Mechanics of Advanced Materials and Structures*, 1-16.
- Rice, J. R. (1993), Spatio-temporal complexity of slip on a fault, *J. Geophys. Res.*, 98(B6), 9885-9907, doi:10.1029/93JB00191.
- Rice, J. R. (1999), Flash heating at asperity contacts and rate-dependent friction, *Eos Trans. AGU*, 80(46), F471.
- Rice, J. R. (2006), Heating and weakening of faults during earthquake slip, *J. Geophys. Res.*, 111(B5), doi:10.1029/2005JB004006.
- Rojas, O., E. M. Dunham, S. M. Day, L. A. Dalguer, and J. E. Castillo (2009), Finite difference modelling of rupture propagation with strong velocity-weakening friction, *Geophys. J. Int.*, 179(3), 1831-1858, doi:10.1111/j.1365-246X.2009.04387.x.
- Rubin, A. M. (2008), Episodic slow slip events and rate-and-state friction, *J. Geophys. Res. Solid Earth*, 113(B11), doi:10.1029/2008JB005642.

- Rubin, A. M., and J. P. Ampuero (2005), Earthquake nucleation on (aging) rate and state faults, *J. Geophys. Res. Solid Earth*, 110(B11).
- Ruina, A. (1983), Slip instability and state variable friction laws, *J. Geophys. Res.*, 88(B12), 10359-10370, doi:10.1029/JB088iB12p10359.
- Ryan, K. J., and D. D. Oglesby (2014), Dynamically modeling fault step overs using various friction laws, *J. Geophys. Res. Solid Earth*, 119(7), 5814-5829, doi:10.1002/2014JB011151.
- Sachs, M. K., et al. (2012), Virtual California earthquake simulator, *Seismol. Res. Lett.*, 83(6), 973-978, doi:10.1785/0220120052.
- Satake, K. (2015), Geological and historical evidence of irregular recurrent earthquakes in Japan, *Phil. Trans. R. Soc. A*, 373(2053), 20140375.
- Savage, J., and W. Prescott (1978), Asthenosphere readjustment and the earthquake cycle, *J. Geophys. Res. Solid Earth*, 83(B7), 3369-3376.
- Savage, J., and J. Svarc (1997), Postseismic deformation associated with the 1992 $M_w=7.3$ Landers earthquake, southern California, *J. Geophys. Res. Solid Earth*, 102(B4), 7565-7577, doi:10.1029/97JB00210.
- Sawai, Y., Y. Namegaya, Y. Okamura, K. Satake, and M. Shishikura (2012), Challenges of anticipating the 2011 Tohoku earthquake and tsunami using coastal geology, *Geophys. Res. Lett.*, 39(21), doi:10.1029/2012GL053692.
- Sawai, Y., Y. Namegaya, T. Tamura, R. Nakashima, and K. Tanigawa (2015), Shorter intervals between great earthquakes near Sendai: Scour ponds and a sand layer attributable to AD 1454 overwash, *Geophys. Res. Lett.*, 42(12), 4795-4800.

- Scholz, C. H. (1998), Earthquakes and friction laws, *Nature*, 391(6662), 37-42.
- Scholz, C. H., and C. Small (1997), The effect of seamount subduction on seismic coupling, *Geology*, 25(6), 487-490, doi:10.1130/0091-7613(1997)025<0487:TEOSSO>2.3.CO;2.
- Shibazaki, B., et al. (2011), 3D modeling of the cycle of a great Tohoku-oki earthquake, considering frictional behavior at low to high slip velocities, *Geophys. Res. Lett.*, 38(21), doi:10.1029/2011GL049308.
- Shimamoto, T., and H. Noda (2014), A friction to flow constitutive law and its application to a 2-D modeling of earthquakes, *J. Geophys. Res. Solid Earth*, 119(11), 8089-8106.
- Simons, M., et al. (2011), The 2011 magnitude 9.0 Tohoku-Oki earthquake: Mosaicking the megathrust from seconds to centuries, *science*, 332(6036), 1421-1425.
- Sugawara, D., F. Imamura, K. Goto, H. Matsumoto, and K. Minoura (2013), The 2011 Tohoku-oki earthquake tsunami: similarities and differences to the 869 Jogan tsunami on the Sendai plain, *Pure Appl. Geophys.*, 170(5), 831-843, doi:10.1007/s00024-012-0460-1.
- Sun, T., K. Wang, T. Fujiwara, S. Kodaira, and J. He (2017), Large fault slip peaking at trench in the 2011 Tohoku-oki earthquake, *Nat. Commun.*, 8, 14044, doi:10.1038/ncomms14044.
- Tullis, T. E., et al. (2012), Generic earthquake simulator, *Seismol. Res. Lett.*, 83(6), 959-963, doi:10.1785/0220120093.

- Ujiie, K., et al. (2013), Low coseismic shear stress on the Tohoku-Oki megathrust determined from laboratory experiments, *Science*, *342*(6163), 1211-1214.
- Usami, K., K. Ikehara, T. Kanamatsu, and C. M. McHugh (2018), Supercycle in great earthquake recurrence along the Japan Trench over the last 4000 years, *Geoscience Letters*, *5*(1), 11, doi:10.1186/s40562-018-0110-2.
- Wang, K., and S. L. Bilek (2011), Do subducting seamounts generate or stop large earthquakes?, *Geology*, *39*(9), 819-822, doi:10.1130/G31856.1.
- Wang, K., and S. L. Bilek (2014), Invited review paper: Fault creep caused by subduction of rough seafloor relief, *Tectonophysics*, *610*, 1-24, doi:10.1016/j.tecto.2013.11.024.
- Ward, S. N. (2012), ALLCAL earthquake simulator, *Seismol. Res. Lett.*, *83*(6), 964-972, doi:10.1785/0220120056.
- Weng, H., and H. Yang (2017), Seismogenic width controls aspect ratios of earthquake ruptures, *Geophys. Res. Lett.*, *44*(6), 2725-2732, doi:10.1002/2016GL072168.
- Yamamoto, Y., K. Obana, S. Kodaira, R. Hino, and M. Shinohara (2014), Structural heterogeneities around the megathrust zone of the 2011 Tohoku earthquake from tomographic inversion of onshore and offshore seismic observations, *J. Geophys. Res. Solid Earth*, *119*(2), 1165-1180.
- Yamanaka, Y., and M. Kikuchi (2004), Asperity map along the subduction zone in northeastern Japan inferred from regional seismic data, *J. Geophys. Res. Solid Earth*, *109*(B7), doi:10.1029/2003JB002683.

- Yang, H., Y. Liu, and J. Lin (2012), Effects of subducted seamounts on megathrust earthquake nucleation and rupture propagation, *Geophys. Res. Lett.*, *39*(24), doi:10.1029/2012GL053892.
- Yang, H., Y. Liu, and J. Lin (2013), Geometrical effects of a subducted seamount on stopping megathrust ruptures, *Geophys. Res. Lett.*, *40*(10), 2011-2016, doi:10.1002/grl.50509.
- Yokota, Y., et al. (2011), Joint inversion of strong motion, teleseismic, geodetic, and tsunami datasets for the rupture process of the 2011 Tohoku earthquake, *Geophys. Res. Lett.*, *38*(7).
- Yu, H., Y. Liu, H. Yang, and J. Ning (2018), Modeling earthquake sequences along the Manila subduction zone: Effects of three-dimensional fault geometry, *Tectonophysics*, doi:10.1016/j.tecto.2018.01.025.
- Zhao, D., A. Hasegawa, and S. Horiuchi (1992), Tomographic imaging of P and S wave velocity structure beneath northeastern Japan, *J. Geophys. Res. Solid Earth*, *97*(B13), 19909-19928, doi:10.1029/92JB00603.
- Zhao, D., Z. Huang, N. Umino, A. Hasegawa, and H. Kanamori (2011), Structural heterogeneity in the megathrust zone and mechanism of the 2011 Tohoku-oki earthquake (Mw 9.0), *Geophys. Res. Lett.*, *38*(17).